Nakajima-King Retrievals for Mixed-Phase Clouds

A Model-Only Approach

Kai-Uwe Eiselt

Master's Thesis

supervised by
Prof. Dr. Stefan A. Bühler
Dr. Ákos Horváth

Meteorological Institute
University of Hamburg
Germany
03.09.2019

Thesis topic:

Nakajima-King Retrievals for Mixed-Phase Clouds

Abstract

In this study the performance of Nakajima-King bi-spectral retrievals in the case of deep-convective ice-over-liquid clouds is investigated. The methodology used is based solely on models: on the one hand the high-resolution numerical weather prediction model ICON providing the cloud field and on the other hand the fast radiative transfer model RTTOV for the calculation of the corresponding synthetic reflectances using the ICON output as input. A Nakajima-King bi-spectral retrieval algorithm is then applied to these reflectances and the resulting retrieval is compared to the "true" cloud field quantities (column integrated liquid, ice, and total water path) from the numerical model output.

Several model input data and model set-up configurations are investigated on a pixel-to-pixel basis as well as on a domain-mean basis. The three input data set-ups are the original numerical weather prediction model output, a more idealised set-up with clouds condensed in one model layer, and an even more idealised set-up with condensed clouds as well as homogenised atmospheric profiles of temperature, pressure, and water vapour. Furthermore, different data set-ups are achieved by considering either both cloud water and cloud ice or only cloud ice. Varied radiative transfer model set-ups are incorporated by changing parameters like the sun zenith angle and the assumed ice effective diameter, as well as by changing the ice cloud scheme in the model calculations. Additionally, influences of random measurement error and sensor bias are simulated by adding, respectively, a noise and a bias to the synthetic reflectances.

In the most idealised case with only cloud ice the retrieval corresponds nearly perfectly to the "truth" proving the conceptual viability of the approach. Considering both cloud water and cloud ice results in more ambivalence. This ambivalence is found to depend on the assumption of ice effective diameter in the ice cloud radiation scheme (Baum scheme) in RTTOV. Small ice diameters cause the retrieval to correspond better to integrated ice water path while for large ice diameters the correspondence to integrated total water path is better. In either case the relative retrieval error stays within $\pm$ 10 %. For medium ice effective diameter the results are less clear with relative errors of up to 30 %. Using the other ice cloud radiation scheme available in RTTOV (Baran scheme) leads to substantially different retrieval results with relative errors of close to 100 %.

A typical sensor bias (4 %) is found to have some impact in deep-convective cases. Its influence is investigated in combination with varied sun zenith angle, which on its own does not have considerable impact. For high sun the bias only introduces little difference ($< 5\%$). For middle sun the influence is stronger (5 to 10 %) and for low sun the influence is substantial (up to and exceeding 20 %). A typical random measurement error (noise, 0.5 %) does seem to have only negligible influence (< 1 %).

It is concluded that Nakajima-King bi-spectral retrieval results in deep-convective ice-over-liquid clouds might be improved by using the retrieved effective particle size to determine if the retrieved quantity more closely resembles integrated ice or total water path. However, better ice cloud radiation parametrisations and further analysis are needed to increase confidence in this result. A further conclusion is that while a typical random measurement error might be neglected, a typical bias should be corrected for since its influence on the retrieval can be substantial.

"I have often thought that the nature of science would be better understood if we called theories 'misconceptions' from the outset, instead of only after we have discovered their successors. Thus we could say that Einstein's Misconception of Gravity was an improvement on Newton's Misconception, which was an improvement on Kepler's. The Neo-Darwinian Misconception of Evolution is an improvement on Darwin's Misconception, and his on Lamarck's. If people thought of it like that, perhaps no one would need to be reminded that science claims neither infallibility nor finality."

David Deutsch, *The Beginning of Infinity* (2011)

Contents

List of Figures

List of Tables

List of Acronyms

ATBD algorithm theoretical basis document

BMBF German Federal Ministry of Education and Research

CDO climate data operator

CFC cloud fraction

CLAAS-2 CLoud property dAtAset using SEVIRI, Edition 2

CLI cloud ice

CLW cloud water

COSMO-DE COnsortium for Small-scale Modelling

DAK Doubling Adding KNMI

DKRZ German Climate Computing Centre

DOM Discrete Ordinates Method

DWD German Weather Service

ECMWF European Centre for Medium-Range Weather Forecasts

EUMETSAT European Organisation for the Exploitation of Meteorological Satellites

GOES Geostationary Observational Environmental Satellite

HD(CP)^2 High Definition Clouds and Precipitation for advancing Climate Prediction

ICON ICOsahedral Non-hydrostatic atmosphere model

IPCC Intergovernmental Panel on Climate Change

ISCCP International Satellite Cloud Climatology Project

IWP column integrated ice water path

KNMI Royal Netherlands Meteorological Institute

LES large eddy simulation

LUT look-up table

LWP column integrated liquid water path

MODIS MOderate Resolution Imaging Spectroradiometer

MPI-M Max Planck Institute for Meteorology

NWP numerical weather prediction

NWP SAF Numerical Weather Prediction Satellite Application Facility

OPAC Optical Properties for Aerosols and Clouds

PATMOS-x Pathfinder Atmosphere Extended

RAA relative azimuth angle

RTE radiative transfer equation

RTM radiative transfer model

RTTOV Radiative Transfer for Television Infrared Observation Satellites Operational Vertical Sounder

RTTOVv12.2 RTTOV Version 12.2

SEVIRI Spinning Enhanced Visible and InfraRed Imager

SeAA sensor azimuth angle

SeZA sensor zenith angle

SuAA sun azimuth angle

SuZA sun zenith angle

TWP column integrated total water path

WP column integrated water path

1 Introduction

Ice and mixed-phase clouds play an important role in Earth's climate system. They influence the global atmospheric hydrological cycle and modulate the radiation budget. Clouds in general, as the Intergovernmental Panel on Climate Change (IPCC) states in their latest assessment report, "continue to contribute the largest uncertainty to estimates and interpretations of the Earth's changing energy budget" (Stocker et al., 2013, chap. 7). It has long since been recognised that this uncertainty is in considerable part due to cloud ice which comprises a major challenge regarding Earth system observation and modelling (Waliser et al., 2009).

High-quality observational data are essential for understanding the influence of cloud ice on the climate system and its implementation in climate models, with accurate modelling in turn being important for projecting the future development of Earth's climate. In a landmark study Waliser et al. (2009) reviewed the available datasets and models for cloud ice and pointed out considerable discrepancies and inconsistencies between different datasets as well as different models. They made some suggestions for how to improve the data to be able to put better constraints on the models and hence improve them, too. Eliasson et al. (2011) built on that with more rigorous comparisons of satellite data and come to similar conclusions. Nearly a decade after Waliser et al. (2009), Duncan and Eriksson (2018) make an update and find that, while some progress has been made and large-scale patterns (temporal and spatial) are consistent between multiple data sets, they still differ substantially. They also point out that the reasons for these differences are likely very similar to the ones given in Waliser et al. (2009). All three studies suggest that the major reasons for the discrepancies in the datasets are the varying microphysical assumptions within the different retrieval methods which lead to different advantages and disadvantages. A further problem is that a significant portion of the cloud ice in the atmosphere is located in mixed-phase cloud systems (see section 5.1 and Figure 12 in Smith, 2014). Precipitation and the ice-over-liquid configuration make retrievals in these clouds much more difficult then in thinner single-phase ice clouds (Huang et al., 2006; Minnis et al., 2007; Horváth and Davies, 2007; Tian et al., 2018). Eliasson et al. (2011) also show that different retrieval methods are sensitive to different parts of such clouds and a comparison is hence not straightforward.

One of the most widely used retrieval methods is the Nakajima and King (1990) retrieval, which employs visible and shortwave infrared satellite channels to derive cloud microphysical properties (for a more detailed description see section 2). They are applied for example within the International Satellite Cloud Climatology Project (ISCCP) (Rossow and Schiffer, 1991, 1999), for MOderate Resolution Imaging Spectroradiometer (MODIS) retrievals (King et al., 1997; Platnick et al., 2017), in the CLoud property dAtAset using SEVIRI, Edition 2 (CLAAS-2) data record (Finkensieper et al., 2016; Benas et al., 2017), or in the Pathfinder Atmosphere Extended (PATMOS-x) dataset (Heidinger et al., 2014). A major problem with this retrieval type is that for mixed-phase clouds it is unclear how to interpret its results (Horváth and Davies, 2007; for a more elaborate summary see section 5.1 in Smith, 2014). Since, unlike for multichannel microwave retrievals, no vertical resolution is possible here, the

retrieved property is either the column integrated ice water path (IWP), the column integrated total water path (TWP), or, although this is mostly deemed unlikely, the column integrated liquid water path (LWP). It has to be noted that precipitating hydrometeors are usually too large to be retrieved at optical and infrared wavelengths, so IWP, TWP, and LWP refer to the integrated cloud water only. For approaches to retrieve precipitation with Nakajima-King type retrievals see Roebeling and Hollman (2009). There has been no consensus in the literature to which of these three properties the Nakajima-King retrieval in mixed-phase clouds best corresponds. This is the main focus of the present study. The aim is to make progress on the interpretation of retrieval results in mixed-phase clouds and to try to point out some problems regarding current assumptions made in the treatment of ice. Despite the large uncertainties of Nakajima-King type retrievals in mixed-phase clouds, they are frequently used, e.g. for model evaluation (see, i.a., Alexandri et al., 2015; Brisson et al., 2016, Keller et al., 2015; Wang et al., 2015), because of their extensive spatial and temporal coverage. Unfortunately there has only been little work on quantification of the errors of Nakajima-King retrievals in mixed-phase clouds and even where this is done, the results are inconsistent (see Horváth and Davies, 2007; Minnis et al., 2007; section 5.1 in Smith, 2014; Tian et al., 2018). More clarity on the interpretation and shortcomings of this widely used retrieval is essential for progress in the understanding of cloud ice.

As Bugliaro et al. (2011) point out, one reason for the difficulty of interpretation is that independent data against which Nakajima-King retrievals can be validated are hard to come by. Possible independent methods are satellite based microwave retrievals, ground based radar retrievals, or in-situ aircraft measurements. Horváth and Davies (2007) find that, while for warm liquid clouds their microwave and Nakajima-King retrievals agree reasonably, for cold mixed-phase clouds the agreement is weak. They note that, while the most common interpretations of Nakajima-King retrievals in mixed-phase clouds are IWP or TWP, in their cases the retrievals correspond best to LWP. Tian et al. (2018) on the other hand suggest the retrieval should rather be interpreted as TWP. They compare Nakajima-King type retrievals from, i.a., the Geostationary Observational Environmental Satellite (GOES) to ground based radar retrievals and also find low correlation and relatively large mean differences. All the above referenced independent methods have several problems, however. For one, as already stated, the different methods are based on different microphysical assumptions and are sensitive to different vertical regions of the clouds (Eliasson et al., 2011). Furthermore, microwave retrievals are usually unavailable for continental clouds and precipitation confounds their results with respect to ice. Ground-based radar systems are constrained in their spatial coverage and in-situ measurements are even more constrained and very sparse. To overcome these problems, Bugliaro et al. (2011) suggest another method. They start from a known cloud field generated by a numerical weather prediction (NWP) model and use a radiative transfer model (RTM) to generate synthetic satellite images. Because of its completely model-based nature this approach also has its own shortcomings, which will become clear in the present study, but a main advantage is that the cloud field (the "truth") is known and cloud liquid water and cloud ice

can be precisely separated and hence compared separately to the retrieval results. This is the approach followed in the present study.

The thesis is structured as follows. Section 2 explains the methodology in more detail. Section 3 gives the model descriptions and lays out the model set-up. Section 4 provides the results and offers some discussion. Finally, section 5 gives a summary, some conclusions, and an outlook.

2 Methodology

This section first details the basic principles of the specific retrieval methodology employed in this study and subsequently explains how this is applied in practice. Finally, a description of the model-only approach followed in the present study is given.

2.1 Nakajima-King Bi-Spectral Retrieval

In the field of remote sensing the term "retrieval" generally refers to the derivation of atmospheric properties (e.g. aerosols, precipitation, clouds) from satellite data. One of the most widely used retrieval methods regarding cloud microphysical properties was introduced by Nakajima and King (1990). The basic principle of this method is that at solar reflectances of clouds, water-absorbing wavelengths are mostly sensitive to cloud effective particle radius (r_e), while non-absorbing wavelengths are mostly sensitive to cloud optical thickness (τ). Nakajima and King (1990) show this by employing asymptotic theory to derive the reflection properties of clouds in the atmosphere. They determine that the reflection properties depend primarily on scaled τ and the similarity parameter s which, in turn, depends primarily on r_e. They further show that s is almost zero for wavelengths $\lessapprox 1$ μm so that the reflection function in this part of the electromagnetic spectrum is primarily determined by τ. For wavelengths of about 1.65 μm or 2.16 μm, on the other hand, s primarily depends on r_e (see Figure 1 in Nakajima and King, 1990), which can be defined as (Hansen and Travis, 1974):

$$r_e = \frac{\int_0^\infty r^3 n(r) dr}{\int_0^\infty r^2 n(r) dr} \tag{1}$$

where $n(r)$ is the particle size distribution and r is the particle radius. While in retrieval algorithms nowadays more wavelengths are employed (i.a. to additionally retrieve cloud top temperature, see e.g. Benas et al., 2017) the basic [τ, r_e] retrieval relies only on two spectral channels, one non-absorbing and one absorbing, as described above, and is hence typically called *Nakajima-King bi-spectral retrieval*.

To be able to perform this kind of retrieval algorithmically, RTMs are used to calculate reflectances for an absorbing and a non-absorbing channel based on given τ and r_e combinations. The reflectances are then stored in a look-up table (LUT). An example for a LUT produced for the present study is depicted in Figure 1, where τ (blue) and r_e (red) iso-lines depending on the 0.6 μm (non-absorbing, x-axis) and 1.6 μm (absorbing, y-axis) reflectances are shown. Reflectances in [0.6, 1.6] μm space as measured by satellites are then transformed within the algorithm into the [τ, r_e] space. For every pixel in the satellite image this yields a [τ, r_e] value pair.

The cloud property of interest and the final product of cloud physical property retrieval algorithms is either the LWP or IWP of the clouds − in plain words, the answer to the question: How much cloud water is there in a given atmospheric column? To get from τ and r_e to LWP or IWP is not straightforward but under the assumption of cloud vertical homogeneity it can

be approximated. The formula most widely used for this purpose as given by Stephens (1978) is:

$$LWP \text{ or } IWP = \frac{4\rho\tau r_e}{3Q_e} \tag{2}$$

where Q_e is the extinction efficiency and ρ is either $\rho_w = 1$ g/cm^3 or $\rho_i = 0.93$ g/cm^3 for liquid and ice water, respectively. Note that ρ_i measurements show large variations but here the above given value is chosen because it is used in the most prominent retrieval datasets (e.g. CLAAS-2, Benas et al., 2017). The units of LWP and IWP are g/m^2. For visible wavelengths $Q_e \approx 2$ (see e.g. Petty, 2006) roughly holds so that we get:

$$LWP \text{ or } IWP = \frac{2}{3}\tau r_e \rho \tag{3}$$

To be able to exploit satellite sensors that only provide visible non-absorbing wavelength channels but no absorbing ones, fixed values for r_e can be assumed so as to be able to retrieve LWP or IWP. This has been done for example within ISCCP (Rossow and Schiffer, 1991, 1999).

2.2 Look-Up Table Generation and Custom Retrieval Algorithm

The basic purpose of the LUTs within the Nakajima-King bi-spectral retrieval is to relate the satellite reflectances in the water absorbing and the non-absorbing channels (here 1.6 and 0.6 μm, respectively) to τ and r_e. The generation of the custom LUTs (as an example see Figure 1) for this study roughly follows the algorithm theoretical basis document (ATBD) for the CPP algorithm (Meirink and Zadelhoff, 2016; CPP was first introduced by Roebeling et al., 2006) from the Royal Netherlands Meteorological Institute (KNMI) although there are some differences. The general procedure is to set up several [τ, r_e] value pairs and use them as input for a RTM to calculate the reflectances for a water absorbing channel and for a non-absorbing channel. The resulting reflectances are then stored in a LUT. The specific sensor that is simulated by the RTM in this study is the Spinning Enhanced Visible and InfraRed Imager (SEVIRI) (Schmetz et al., 2002) with the 0.6 μm channel as the non-absorbing and the 1.6 μm channel the absorbing channel (the exact channel means are 0.635 μm and 1.64 μm, respectively). The RTM used here is Radiative Transfer for Television Infrared Observation Satellites Operational Vertical Sounder (RTTOV) (Saunders et al., 2018; see section 3.2). Note that KNMI use a different RTM, the Doubling Adding KNMI (DAK) model, to calculate the reflectances for the CPP LUTs.

Because of the different scattering properties of cloud liquid droplets and cloud ice crystals, different LUTs for liquid and ice clouds are generated. Figure 1 shows a LUT for ice clouds and a comparison of it to the corresponding LUT for liquid water is depicted in Figure $A.1$ in the appendix. The need for separate LUTs is mostly due to the complex shapes that ice crystals can assume while liquid droplets are much closer to spherical shape, which leads to different scattering phase functions (see e.g. Mayer and Kylling, 2005, their Figure 6; Yang et al., 2013). Ice and liquid cloud particles also grow to different typical sizes, with ice crystals mostly being larger than liquid droplets, at least in their effective size (see e.g. Hess et al., 1998). The size

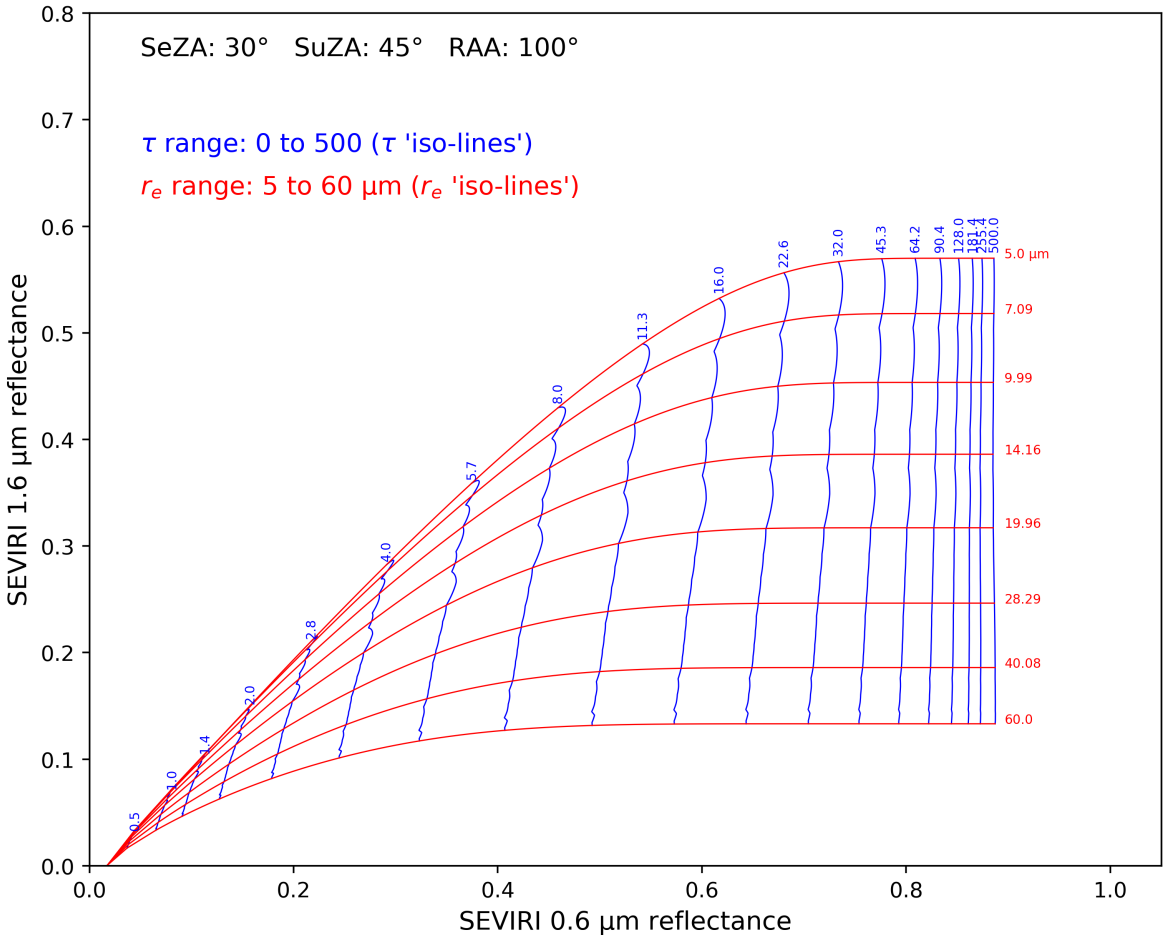

Figure 1: Example of a custom LUT for IWP retrievals. For specifications refer to Table 1 and section 2.2. See Figure *A*.1 in the appendix for a comparison to the corresponding LUT for LWP and Figures *A*.11 and *A*.12 for other sun-view geometries.

interval for liquid particles used here is 3 to 26 μm while for ice particles it is 5 to 60 μm. The latter three values (26, 5, and 60 μm) are the limits enforced in RTTOV, while 3 μm as lower bound for the LWP LUT is chosen because it is the value used in the CPP LUTs. 5 μm as lower bound for the IWP LUT is also the same as for CPP but the upper bounds for cloud ice and cloud liquid water are different from the CPP values (see Meirink and Zadelhoff, 2016, their Table 2). A further difference to the CPP LUTs is the LUT "resolution". While for CPP eight (liquid) and nine (ice) different r_e are used, here we have 500 different r_e. For τ there are 22 different values in the CPP LUTs, while here we use 1000 different τ values. The spacing of the values is equidistant in $\log(r_e)$ and $\log(\tau)$, respectively.

Vertical cloud extension cannot be accounted for in Nakajima-King bi-spectral retrievals and clouds are assumed to be vertically homogeneous (for developments regarding this problem see Minnis et al., 2007, and references therein). In the LUTs the clouds are assumed to be confined to one atmospheric layer. For the custom LUTs this is at ~1800 m altitude for liquid and ~5800 m altitude for ice clouds, which is close to the values used in CPP. Especially for mixed-phase deep-convective clouds this can deviate strongly from reality. However, it is not

practical to include the vertical cloud extension or the cloud height as further dimensions in the LUTs since no robust information regarding either can be directly derived from the Nakajima-King bi-spectral methodology. Within the CPP algorithm cloud height is somewhat accounted for by atmospheric correction (Meirink et al., 2009). There, more satellite channels in the infrared are employed to estimate the cloud top temperature and hence derive their height. This is neglected here (see section 3.3). For a summary of the properties of the custom made LUTs see Table 1.

Table 1: Properties of the custom made LUTs. For more detailed information refer to sections 2.2 and 3.2. See Figures 1 as well as *A*.1, *A*.11, and *A*.12 in the appendix for examples.

parameter	**LWP LUT**	**IWP LUT**
cloud height	∼1800 m	∼5800 m
τ range	0 and 0.5 - 500	0 and 0.5 - 500
τ "resolution"	1000 values equidistant in $\log(\tau)$	
scattering scheme	"Deff"	Baum
r_e range	3 - 26 μm	5 - 60 μm
r_e "resolution"	500 values equidistant in $\log(r_e)$	

The algorithm procedure with the custom generated LUTs works as follows. A [0.6, 1.6] μm reflectance pair is taken from a satellite image. Via nearest-neighbour interpolation the closest reflectance value pair that is stored in the LUT is then found and the corresponding [τ, r_e] value pair is extracted from the LUT. Note that within KNMI's CPP algorithm more sophisticated interpolation is used, which allows much coarser LUTs. Lastly, equation 3 is employed to calculate IWP or LWP from τ and r_e.

2.3 Retrieval From Simulated Satellite Reflectances

As motivated in section 1, a general problem with satellite retrievals is that they are difficult to validate because independent data sets are usually unavailable and it is especially difficult to come up with data that reliably separates LWP and IWP. Since this is essential for the aim of this study, the approach followed here is similar to that of Bugliaro et al. (2011). The basic idea is to use a cloud resolving NWP model to generate a realistic cloud field which is then fully known, including the values of LWP and IWP. The thus generated model atmosphere is used as input for a RTM to generate a synthetic satellite image corresponding to the model atmosphere (for examples see Figures 3 and 4). Consequently, a Nakajima-King retrieval algorithm can be applied to the synthetic satellite image, as described in section 2.2, to retrieve LWP and IWP. Both can finally be compared with the known "true" LWP and IWP as well as their sum (TWP) from the NWP model atmosphere. See Figure 2 for a flow-chart of this procedure. The NWP model used in this study is the ICOsahedral Non-hydrostatic atmosphere model (ICON) (Zängl et al., 2015, see section 3.1).

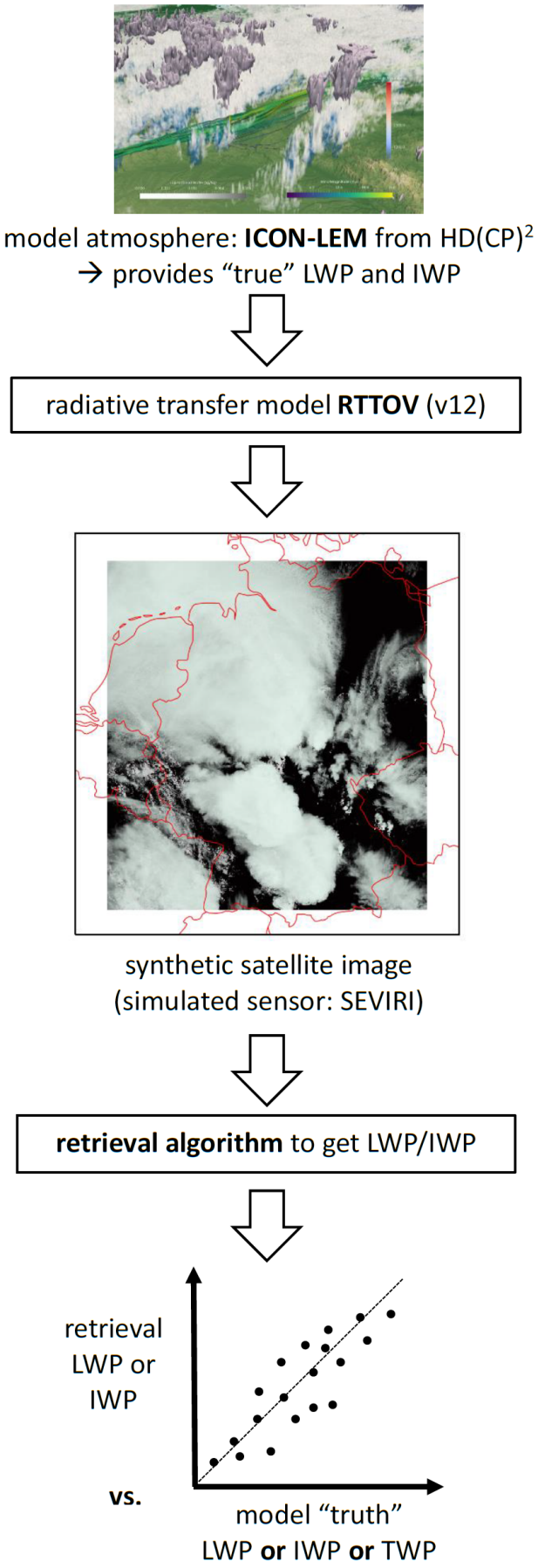

Figure 2: Flow chart of the synthetic retrieval methodology. Refer to section 2 and in particular to section 2.3. Top image taken from the HD(CP)^2 website (`https://hdcp2.zmaw.de/index.php?id=3702`, visited on 09/03/2019).

3 Models and Model Set-Up

This section describes first the NWP model and second the RTM employed in the present study. Subsequently a detailed explanation of the different model set-ups is given.

3.1 ICON

ICON is a non-hydrostatic unified modelling system developed recently in collaboration by the German Weather Service (DWD) and the Max Planck Institute for Meteorology (MPI-M). As a unified system it has the capability of being applicable globally as a NWP model as well as for climate modelling (Zängl et al., 2015). Within the project High Definition Clouds and Precipitation for advancing Climate Prediction (HD(CP)^2) (`http://www.hdcp2.eu`, visited on 09/03/2019) initiated by the German Federal Ministry of Education and Research (BMBF) it has subsequently been expanded to a large eddy simulation (LES) configuration (ICON-LES) that operates at much higher resolutions of $\mathcal{O}(100$ m) on limited domains, where it has been shown to work for classical idealised cases with doubly periodic boundary conditions and flat geometries (Dipankar et al., 2015). Over the further course of HD(CP)^2, ICON-LES has been applied in real-case scenarios with prescribed boundary conditions and terrain following geometry and it was demonstrated that it represents the turbulence spectrum well and that the water vapour profiles as well as small cumulus clouds are realistic (Heinze et al., 2017). The following paragraphs give a short overview of ICON in general and ICON-LES in particular. For a more detailed description of ICON's dynamical core and ICON-LES the reader is referred to Zängl et al. (2015) and Dipankar et al. (2015), respectively.

ICON solves equations for the prognostic variables suggested by Grassmann and Herzog (2008) on an unstructured icosahedral-triangular grid with C-type staggering. The prognostic variables are the horizontal velocity component normal to the triangle edges, the vertical velocity component, density, virtual potential temperature, and the specific masses and number densities of tracers (water vapour, cloud liquid water, etc.; see below). The unstructured icosahedral-triangular C grid was chosen because it provides for a good treatment of the global sphere, which is a problem on latitude-longitude grids because of the poleward convergence of the meridians, as well as a more obvious mesh refinement for grid nesting than on other grids (Zängl et al., 2015). This leads to some compromises, such as, e.g. compared to a hexagonal grid, the loss of exact energy conservation and the need for numerical filtering (Zängl et al., 2015), as well as restrictions on the use of higher accuracy schemes compared to LES models on latitude-longitude grids (Dipankar et al., 2015).

Because of its unified nature there are three physics parametrisation packages available for ICON: the NWP package, the climate modelling package, and the LES package. One of the advantages of having a unified system is that parametrisations, for such processes as convection, applied in the larger-scale and lower-resolution climate modelling and NWP configurations can be investigated within the same model using the LES configuration at much higher resolution of $\mathcal{O}(100$ m), where smaller scale processes, like convection, are resolved. Since, as motivated in

section 1, clouds are one of the main contributors to uncertainties in current climate projections, much attention has been payed to improving convection parametrisations in climate models. This is one of the main goals of HD(CP)^2. Note that modern NWP models like the COnsortium for Small-scale Modelling (COSMO-DE) (DE specifies the operational NWP version of the model, Baldauf et al., 2011) have resolutions in the range of 1 to 4 km (2.8 km in the case of COSMO-DE), which probably allows for deep convection to be simulated directly, while shallow convection still has to be parametrised (see e.g. Baldauf et al., 2011). This range has been called the "gray zone" (Dipankar et al., 2015) since it is unclear how well convection is actually represented. This was a major motivation for achieving resolutions of $\mathcal{O}(100$ m) for ICON-LES.

The LES physics package incorporates the two-moment mixed-phase microphysics bulk scheme developed by Seifert and Beheng (2006). The hydrometeors treated by this scheme are cloud water, cloud ice, rain, snow, graupel, and hail. The warm-rain part is based on Seifert and Beheng (2001) and the hail part, which was originally not treated by the Seifert and Beheng (2006) scheme, has been added subsequently (see Blahak, 2008; Noppel et al., 2010; Heinze et al., 2017). Within the Seifert and Beheng (2006) scheme the mass as well as the number density of all hydrometeors are calculated explicitly and all relevant homogeneous and heterogeneous nucleation processes have been parametrised. Note that cloud ice is assumed to be of hexagonal plate shape after Heymsfield and Kajikawa (1987). The treatment of cloud fraction works via an all-or-nothing scheme so that the value is either 1 or 0 and there is no subgrid scale fractional cloud cover.

3.2 RTTOV

RTTOV is a fast 1-dimensional radiative transfer model that has been developed by the European Centre for Medium-Range Weather Forecasts (ECMWF) during the 1990s (Eyre, 1991). By the end of that decade it was made available for the community (Saunders et al., 1999). Subsequently, it was developed further within the Numerical Weather Prediction Satellite Application Facility (NWP SAF) funded by the European Organisation for the Exploitation of Meteorological Satellites (EUMETSAT). RTTOV has been widely used for satellite retrievals and radiance assimilation (for microwaves as well as increasingly in the infrared, for an overview see Geer et al., 2018) and has received multiple updates. In the present study, RTTOV Version 12.2 (RTTOVv12.2) is used. Saunders et al. (2018) give an overview of RTTOV's history and its development over time, as well as an update on the improvements of version 12 over the original version released in 1999. Extensive documentation regarding usage (Hocking et al., 2018a) and validation (Saunders et al., 2017) is available from the NWP SAF website (`https://www.nwpsaf.eu/site/software/rttov/`, visited on 09/03/2019). To make the use of RTTOV more convenient, a wrapper for the programming languages Python, C, and C++ has been developed, the documentation of which (Hocking et al., 2018b) is also available on the NWP SAF website. The wrapper for Python was employed here. In the following paragraph a summary of the model properties most pertinent to the present study is given.

RTTOV's transmittance calculations are based on regression coefficients computed with line-by-line RTMs. In RTTOVv12.2 these coefficients are available for a multitude of satellite sensors on 54 pressure levels (see Hocking et al., 2018a, their Tables 1 and 4) and the transmittance calculations are performed on these levels. Radiative transfer on the other hand can, since RTTOV version 9, be computed on user input levels. This is made possible via interpolation of, first, the user input to the coefficient levels and, second, after the calculations, RTTOV's output back to the user levels. The input atmospheric profile on these pressure levels has to consist at least of temperature and water vapour. Profiles for several different gasses can also be given, i.a. ozone (O_3) and carbon dioxide (CO_2). If no gas profiles are given RTTOV defaults to reference profiles (Hocking et al., 2018a, p. 40 and Table 1, as well as Saunders et al., 2017 for the gas profiles). The surface in RTTOV has to be specified via skin temperature, 2 m temperature, surface pressure, 10 m u and v wind (only over ocean), surface type (land, ocean, sea ice), and elevation, as well as latitude and longitude. Additionally, surface water vapour can be given. Surface emissivity and reflectance can either be given as user input or calculated by RTTOV. Several emissivity and reflectance atlases are provided. Note that RTTOV neglects thermal emission for channels at wavelengths < 3 μm and considers only solar radiation. The opposite is true for channels > 5 μm, while channels between these wavelengths include both solar and thermal emission contributions. For solar influenced channels the mandatory sun-view geometry input for RTTOV has to consist of sun zenith angle (SuZA), sensor zenith angle (SeZA), sun azimuth angle (SuAA), and sensor azimuth angle (SeAA). The difference between the latter two is referred to as relative azimuth angle (RAA) and is used, in accordance with the CPP LUTs, in the description of the LUT properties (see the LUT plots, e.g. Figure 1).

Using clouds as input for RTTOV works via specifying cloud water (CLW) and/or cloud ice (CLI) as well as cloud fraction (CFC) profiles. For both phases (CLW and CLI), RTTOV provides two parametrisations, respectively. For CLW this is either the Optical Properties for Aerosols and Clouds (OPAC) scheme (Hess et al., 1998) or the "Deff" scheme, which is new in RTTOVv12.2. The OPAC scheme provides optical properties of five cloud types represented by five different particle size distributions, which correspond to different liquid cloud types (see Table 24 in Hocking et al., 2018a). The "Deff" (short for effective diameter) scheme is based on the Mie CLW optical properties available with the libRadtran package (Mayer and Kylling, 2005). It allows the user to specify the effective particle diameter for every layer in every profile in the RTTOV input. For CLI RTTOV provides the Baum scheme and the Baran scheme. Similar to "Deff", the Baum scheme offers (along with some other parametrisations, see Table 23 in Hocking et al., 2018a) the ability to specify the effective diameter of the ice particles, incorporating the properties described in Baum et al. (2011). Henceforth when referring to the particle sizes specified in the "Deff" and Baum scheme in RTTOV runs, *Deff* and *IceDe* (ice effective diameter) are used, respectively. This is done to separate the values chosen in the RTTOV calculations from the retrieved quantity r_e. Note that to be comparable to the values of *Deff* and *IceDe* used in the RTTOV cloud radiation schemes, r_e has to be multiplied by a

factor of two. The Baran scheme, in contrast to the Baum scheme, parametrises the optical properties without the need for prior information on particle shape and effective size in terms of temperature and amount of CLI (Vidot et al., 2015) and is based on a database described by Baran et al. (2014). For a more detailed summary of RTTOV's cloud schemes see Tables 22 to 24 in Hocking et al. (2018a). Apart from predefined cloud properties RTTOV offers the possibility to provide one's own optical properties. These are absorption and scattering coefficients, the azimuthally-averaged single-scattering phase function and the angles over which it is defined, as well as the coefficients of the Legendre decomposition of the phase function.

While for simple single-layer liquid-only clouds a single-scattering approximation (in RTTOV the simple cloud scheme) might suffice for some purposes, for more complex clouds multiple-scattering calculations are necessary. It is important to note that RTTOV is a 1-dimensional RTM incorporating the independent column approximation, which means it cannot account for 3-dimensional effects (e.g. shadowing, side illumination, horizontal photon transport between columns). For visible and infrared radiances the Discrete Ordinates Method (DOM) (Chandrasekar, 1960) was introduced in RTTOV version 12. The implementation in RTTOV (hereafter referred to as RTTOV-DOM) is such that the radiances agree closely with those calculated by the well-established DISORT model (Stamnes et al., 1988) and is described in more detail in Hocking (2016). The RTTOV-DOM is a pseudo-exact algorithm for monochromatic radiation. Since satellite sensors have finite spectral response functions, they cannot be simulated exactly. But this has been shown to only introduce small errors (about 1 to 2 %, Hocking, 2016). The basic idea of DOM is to divide the full solid angle 4π into a finite number of discrete angular intervals. This causes the scattering part of the radiative transfer equation (RTE) to turn from an integral to a sum, so that the RTE becomes a system of linear equations. In RTTOV the discrete angular intervals are called *DOM streams* and the number can be supplied by the user (default is eight). For the predefined optical properties in RTTOV it can range from two to 128 and should be an even number. If the optical properties are provided by the user, there is no limit on the number of DOM streams. Note that while other radiation schemes in RTTOV can account for the curvature of the Earth, RTTOV-DOM requires the assumption of a plane-parallel atmospheric geometry.

As of RTTOVv12.2 Rayleigh scattering is not calculated by the RTTOV-DOM. It is implemented via a single-scattering parametrisation which adds to the extinction leading to an increasing underestimation of top-of-atmosphere reflectances with increasing optical thickness and decreasing wavelength. The surface within RTTOV-DOM is treated as Lambertian (for more details see Hocking et al., 2018a, p. 64).

3.3 Model Set-Up

This section details the model set-ups for the present study, first for ICON-LES and then for RTTOV. The ICON-LES simulations were set up and performed within HD(CP)^2 while the RTTOV simulations were set up and performed by myself. For examples of synthetic SEVIRI images generated with RTTOV using ICON-LES data as input see Figures 3 and 4.

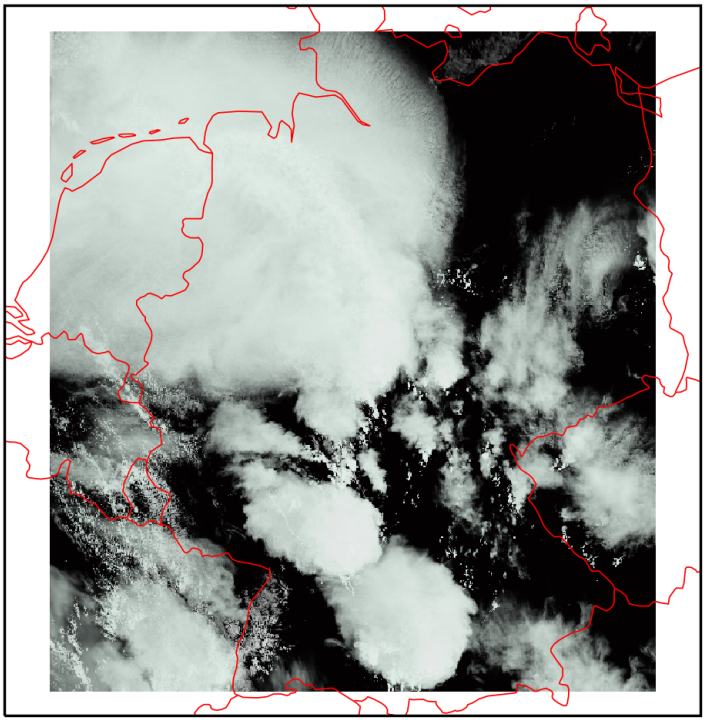

Figure 3: Synthetic SEVIRI image generated with RTTOV from the 2013/06/20 16:00 UTC ICON-LES output. Here, the 0.6 μm reflectance, R_6, is used as red, the 0.8 μm reflectance, R_8, as green, and $0.5(R_6 + R_8)$ as blue. Note the black surface. For details refer to section 3.3.

The ICON-LES configuration for the present study is shown in Figure 5. In this set-up ICON-LES is run on a limited domain over Germany (4.5 °E - 14.5 °E, 47.6 °N - 54.6 °N). As can be seen, there is a local two-step grid refinement with the resolution increasing from a 625 m grid, over 312 m, to 156 m. It has to be noted that because of the icosahedral-triangular grid the resolution here refers to the square root of the mean cell area, which corresponds to about 1.5 times the resolution of a regular grid (Heinze et al., 2017; Dipankar et al., 2015). There are 150 layers in the vertical, with the upper boundary at roughly 21 km (cf. Figure 6). The vertical layer thickness is not uniform, starting from a minimum of 20 m at ground level and increasing to about 380 m at the top. Since the grid is terrain-following, every profile column has its own surface elevation and vertical development. The ICON-LES runs are initialised from an operational COSMO-DE analysis at 00:00 UTC so that turbulence can develop in the morning and the model spin-up is complete during day time. The runs are typically 24 hours (single-day) but there are also some 48 hour runs (double-day). The COSMO-DE data at 2.8 km resolution are interpolated to all three ICON-LES resolutions, so that consistent initialisation is possible. The lateral boundary conditions also come from COSMO-DE via a 20 km nudging zone, shown in Figure 5 as the outer gray frame. The nudging is performed hourly on all prognostic variables. Inside the domain there is a two-step grid refinement via one-way nesting, which means that data is passed only from a coarser to the next finer grid and not vice versa. Again, all prognostic variables are nudged, although here the nudging zones are only

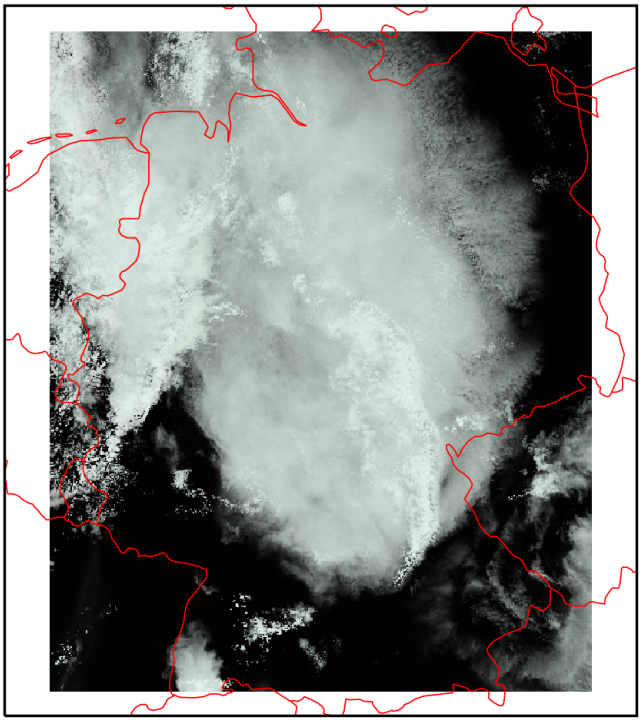

Figure 4: Same as Figure 3 but for 2015/07/05 16:00 UTC.

eight grid elements wide and the nudging is performed at run time (online) for every model time-step. For a more detailed description of the ICON-LES set-up for the limited domain runs over Germany see section 2.2 and Table 1 in Heinze et al. (2017).

To be able to use ICON-LES output as RTTOV input it has to be remapped from the unstructured to a latitude-longitude grid. This is done via nearest-neighbour interpolation using the climate data operator (CDO) (documentation available online: `https://code.mpimet.mpg.de/projects/cdo/wiki/Cdo#Documentation`) software provided by the MPI-M. The resulting latitude-longitude grid is much coarser, with 589 × 637 grid cells for the whole domain, which corresponds to a grid cell size of about 1.2 × 1.2 km. In all RTTOV runs performed in the present study the RTTOV-DOM (see section 3.2) is used to calculate the multiple-scattering in clouds. Via sensitivity tests it has been established that the best compromise between accuracy and computing time is to set the number of DOM streams to eight (for an example see Figure *A*.2 in the appendix). Latitudes and longitudes are a required input in RTTOV. Note that this means the profiles each have their own coordinates which influences the reflectance. For the Germany domain (cf. Figure 5) the respective values for the remapped grid are used in the present study. It has been found that, due to the limited grid size, the effect on the reflectances for the area is negligible.

Since the interest here is centred on the radiation scattering in clouds, the surface influence is minimised. Accordingly, in all RTTOV simulations conducted for the present study the surface type is set to land, the surface emissivity to 1, and the surface reflectivity to 0. The simulation of aerosols in RTTOV has also been turned off. For trace gasses, such as O_3 and CO_2 as well as other gasses, the RTTOV reference profiles are used (see section 3.2). Regarding the

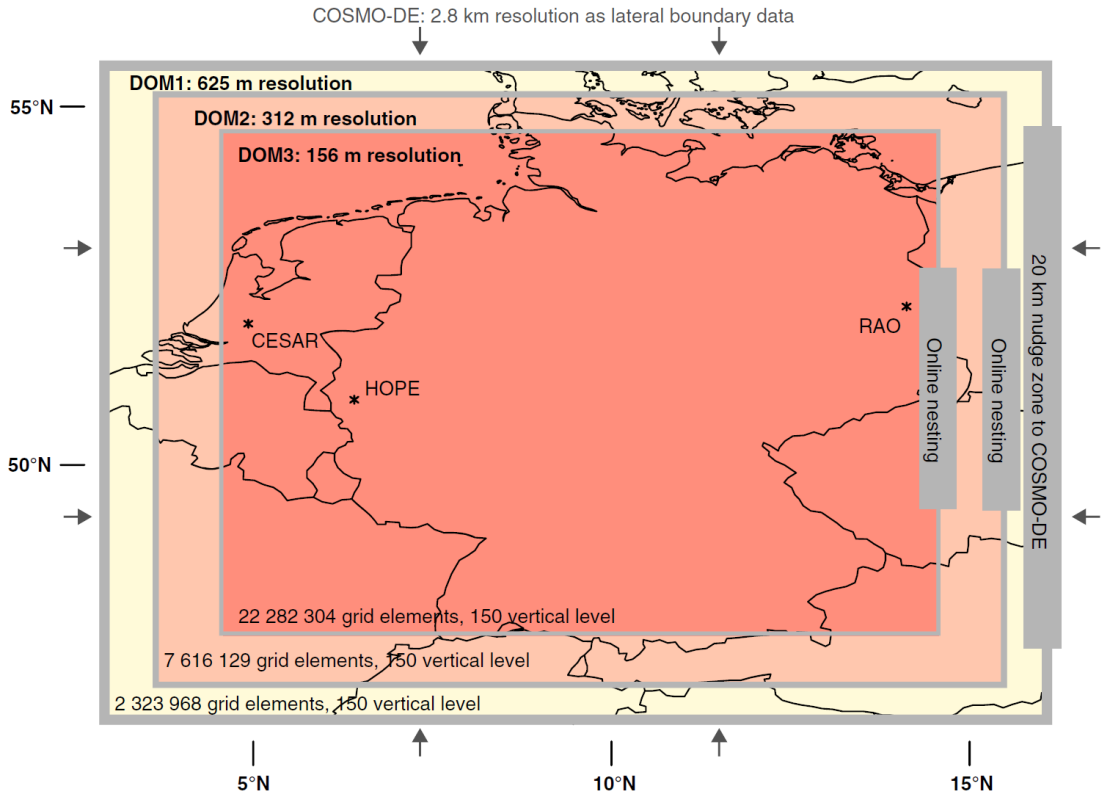

Figure 5: The ICON-LES limited domain over Germany with its two nests and lateral boundary conditions from COSMO-DE. See text form more details. The stars mark observation sites that were used to validate the model runs. The figure is taken from Heinze et al. (2017).

other atmospheric profile variables (temperature, water vapour, CLW, and CLI) three different configurations with different degrees of idealisation are arranged for different model runs to reduce and/or isolate error sources. **(C1)** The first and least idealised configuration consists in the original remapped ICON-LES output. The only idealisation here is that, as in all RTTOV runs (cf. the above text), the type of the surface has been set to land and its emissivity and reflectivity to 1 and 0, respectively. The original cloud heights and their vertical extent are, in contrast to (C2) and (C3), retained. Since in the present study cases with extensive deep convection have been selected specifically, the clouds can span multiple tens of layers. For an example of a vertical cross-section through the clouds in this configuration see Figure 6. **(C2)** In a further, more idealised configuration, the clouds (CLW and CLI) are condensed in one layer (each) while the rest of the atmospheric profile remains the unchanged remapped output of the ICON-LES simulation. See Figure 7 for an example of a vertical cross-section in this configuration. Notably, it follows that, as in (C1), the topography is not homogeneous (gray line in Figure 7) and hence the vertical development of the columns is different for every profile regarding pressure levels and height. Due to the dynamic pressure profiles the clouds are condensed to a specific geometric height. This complicates the procedure of condensing the clouds in one layer since the vertical layer index for the same height is different for every atmospheric profile column in the domain. Configuration (C2) is expected to show the influence

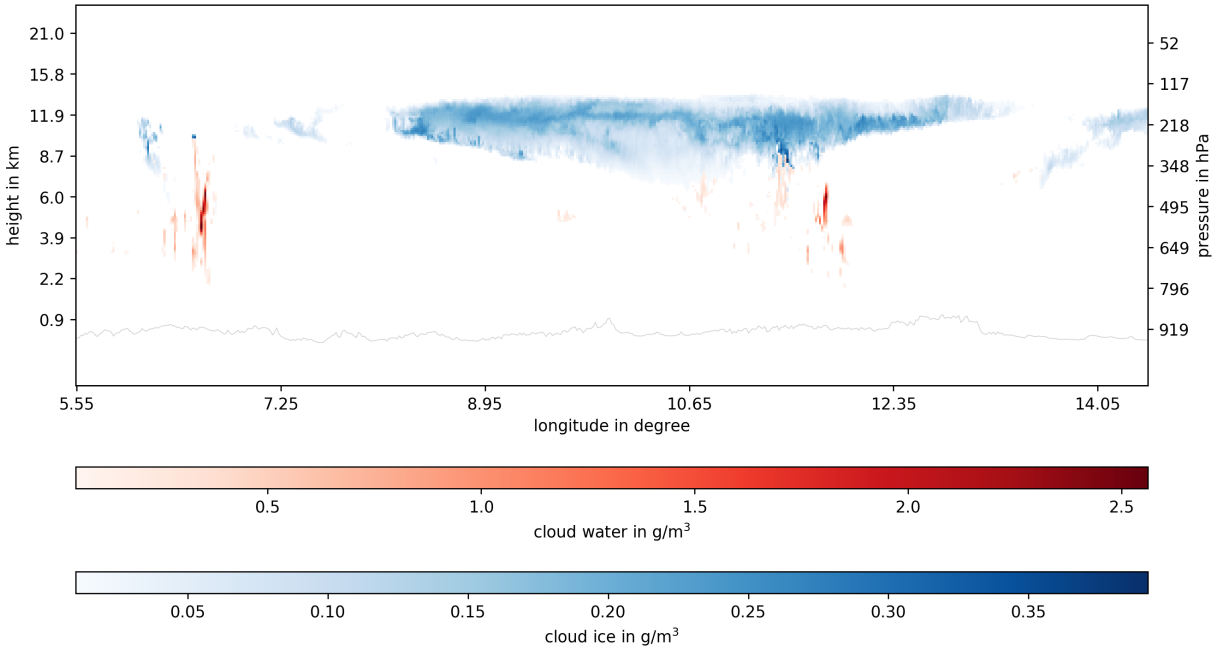

Figure 6: Vertical cross-section of cloud water (red) and cloud ice (blue) of the 2015/07/05 16:00 UTC ICON-LES run over Germany corresponding to configuration (C1). The latitude is ca. 50.4 °N. Note that the y-axis spacing is not equidistant. The heights and pressure values are only intended for orientation because due to the configuration they only hold, in this case, for the central longitude. The gray line gives and indication of the topography and also only roughly corresponds to the heights and pressure values. Refer to section 3.3 for details.

of varying atmospheric profiles on Nakajima-King bi-spectral retrievals. Note though, that due to the limited area approach in the present study the range of atmospheric profiles is also limited and while the results might be applicable for the mid-latitudes, they might not be for other climatic regions. **(C3)** The strongest idealisation consists on the one hand, as for (C2), in condensing CLW and CLI in one layer each and on the other hand in homogenising the temperature and water vapour profiles on the same pressure levels for the whole model domain (note that this means the trace gas profiles are also homogenised). Figure 8 gives an example of a vertical cross-section in this configuration. The profile for the idealisation was selected from the already existing profiles in one of the ICON-LES output files based on the criterion that it is close to the mid-latitude summer profile in Anderson et al. (1986). This is the same profile used for the LUT generation, and the heights to which CLW and CLI are condensed are also the same (at roughly 1.8 km for CLW, and 5.8 km for CLI, see section 2.2). Note that the Anderson et al. (1986) mid-latitude summer profile is used in KNMI's CPP algorithm (Roebeling et al., 2006). Having the same atmospheric profile over the whole domain means that the surface elevation (topography) and grid vertical development, i.e. pressure levels and height, are also the same, so that, in contrast to (C2), for the whole domain one vertical layer index for condensing CLW and CLI, respectively, can be used (cf. Figure 8). Since this is essentially the set-up of the LUT generation, it is used as a sanity-check for the retrieval method. Because here distinct LUTs for

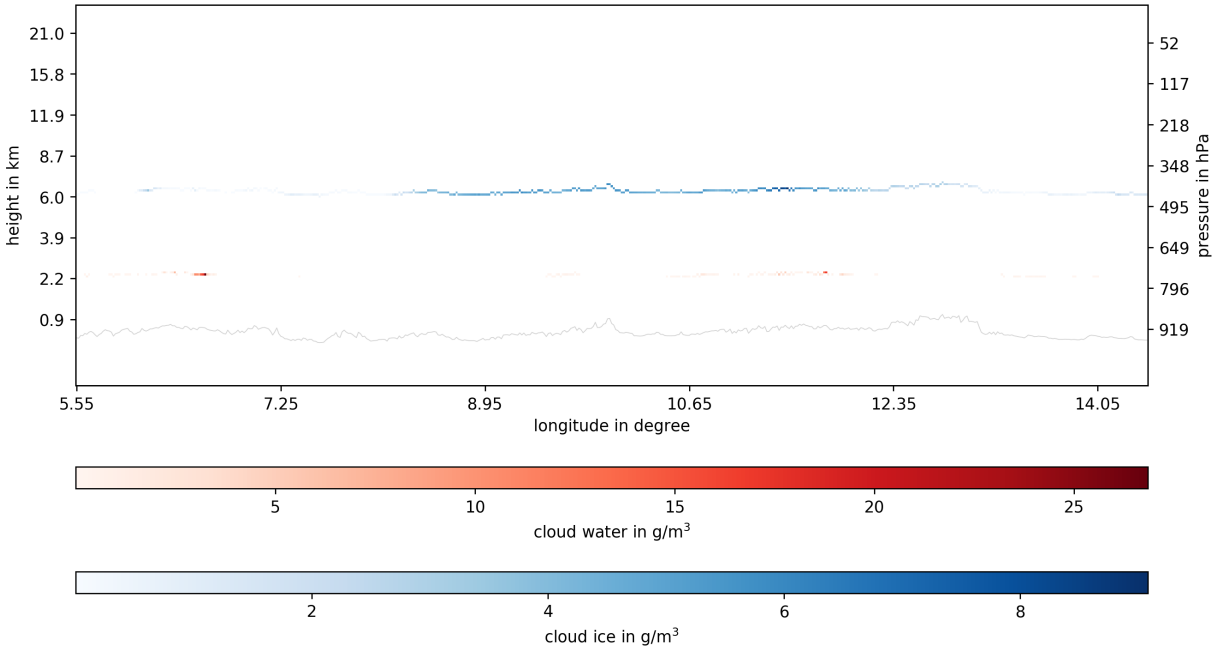

Figure 7: Same as Figure 6 but corresponding to configuration (C2).

LWP and IWP are employed, in order to actually perform such a sanity-check, CLI and CLW, respectively, have to be removed from the atmospheric profile given to RTTOV. As expected, for values of LWP and IWP that fall inside the range of the LUTs, this results in a near-perfect retrieval (see section 4.1.1 and Figure 9) which increases confidence in the method. The reason for this kind of idealisation is that by having all clouds at the same height, Rayleigh scattering should be the same in all profiles, and by having the same trace gas profiles everywhere the absorption of radiation by these gasses should also be the same.

In order to isolate the influence of CLW under CLI, several RTTOV runs employing configuration (C3) but with CLW removed are conducted. Comparing these to the runs with both CLI and CLW is expected to show the influence of CLW under CLI.

Since CLI is of special interest in the present study, the influence of the CLI parametrisation in RTTOV is investigated. Hence, different values of *IceDe* in the Baum scheme are tested but for all other RTTOV runs (testing different influences, e.g. bias or varied SuZA) the Baum scheme is used with an *IceDe* of 60 μm, which is the same value as in ISCCP (Rossow and Schiffer, 1999). As described in more detail in section 3.2, RTTOVv12.2 offers another ice cloud scheme, namely the Baran scheme. To compare both schemes, further simulations employing the Baran scheme are performed. Note that due to its methodology (see section 3.2) it makes no sense to use the Baran scheme with the condensed clouds of configurations (C2) and (C3), since the CLI values are unrealistic (cf. Figures 7 and 8). Hence, results for the Baran scheme are available only for configuration (C1).

As a technical note, it should be mentioned that having multiple cloud layers strongly increases computation time which becomes especially salient for deep-convective clouds spanning multiple layers (see Figure 6). The RTTOV simulations were carried out on the supercomputer *Mistral* at the German Climate Computing Centre (DKRZ) and running the complete 589 $\times$

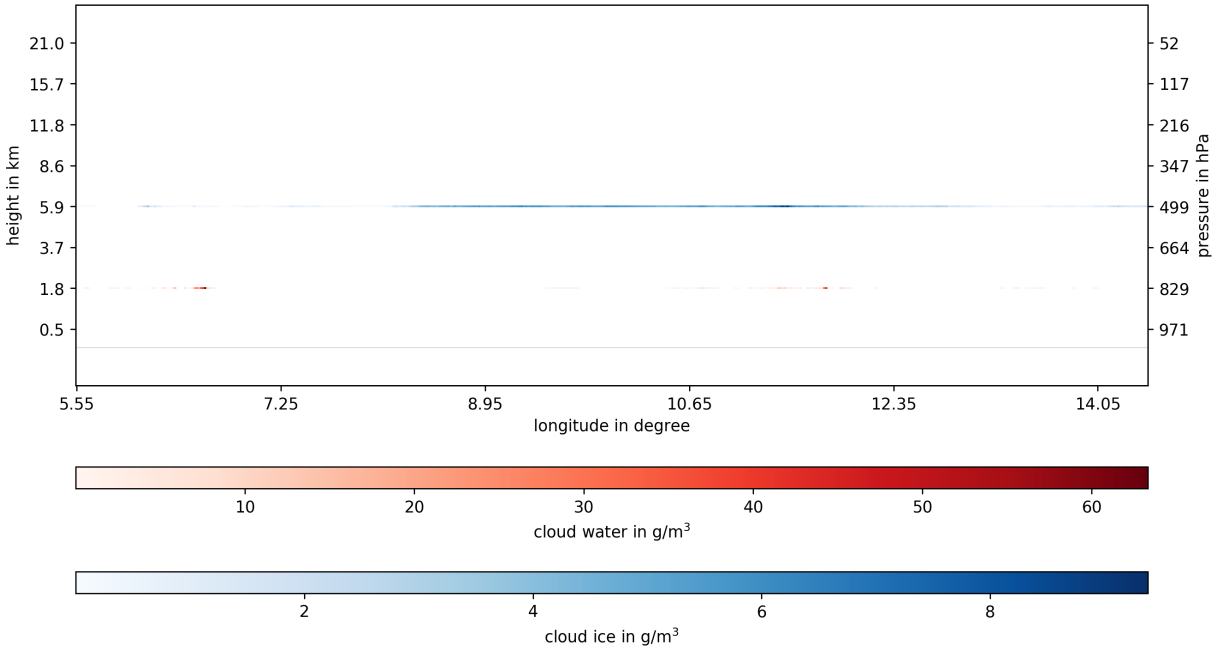

Figure 8: Same as Figure 6 but corresponding to configuration (C3). Note the flat topography and the slightly deviant y-axes compared to Figures 6 and 7.

637 grid cell domain in configuration (C2) or (C3) takes about 45 minutes while in configuration (C1) a patch of only 50 × 50 grid cells alone can reach computation durations of multiple hours. Although the application of the independent column approximation allows each column of the domain to be run separately and thus parallel in RTTOV, there still are restrictions on the amount of simulations in configuration (C1). For this reason several complete domain runs are conducted for configurations (C2) and (C3), while for configuration (C1) there are only a few runs.

In all RTTOV runs the "Deff" scheme is used for CLW. The *Deff* is set to 20 μm, which is the value chosen in ISCCP (Rossow and Schiffer, 1991, 1999). It is expected that, due to the easier treatment of scattering by CLW, the CLW scheme has little influence on the results.

Regarding sun-view geometry in RTTOV the standard set-up chosen here is: SeZA = 30°, SuZA = 45°, SeAA = 10°, and SuAA = 110° (and hence RAA = 100°). Since SEVIRI is a geostationary satellite, it makes sense to keep the SeZA constant over a relatively small simulation domain. To examine the influence of varying sun position, further RTTOV runs are carried out with SuZA of 10° as well as 70° to represent high and low sun, respectively. Note though, that RTTOV is a 1-dimensional RTM that cannot represent 3-dimensional effects such as shadowing and lateral photon transport, thus the applicability of the results here might be limited.

RTTOV simulates a perfect sensor so that there is no random measurement error (noise) and no instrument bias, which is unrealistic. To be able to investigate the effects of noise and reflectance biases on the retrievals, we take the reflectances produced from configuration (C3) RTTOV runs and, for noise, add values drawn from a normal distribution with a mean value of zero and a standard deviation of 0.5 %, and for bias add or subtract 4 % (Govaerts and Clerici,

2004). Note that for all other tests described above neither noise nor bias are added.

4 Results and Discussion

The results are split into two parts. In the first part the retrieval results are discussed on a pixel-to-pixel basis for single time-steps. In the second part domain-means of the retrieval results are investigated for multiple time-steps. A note on nomenclature: To be more general the retrieved quantity is referred to in the following as retrieved column integrated water path (WP) even though all retrievals conducted in the present study use the IWP LUT.

4.1 Single Case Pixel-to-Pixel Comparison

In this section the retrieval results and their comparison to the model "truth" are discussed for single time-step cases on a pixel-to-pixel basis with regards to the influence of ice-over-liquid configuration, idealisation ((C1), (C2), (C3)), different ice cloud schemes, and different assumptions about *IceDe* in the Baum ice scheme.

4.1.1 Retrieval Algorithm Specifications and Sanity-Check

As mentioned in section 3.3 for configuration (C3) there is a sanity-check set-up where the configuration is the same as for the LUT generation and either CLW or CLI is removed (referred to as only-CLI and only-CLW, respectively, in the following). This results in the near-perfect retrieval for values within the limits of the LUTs, as can be seen in Figure 9 which depicts the comparison of retrieved WP to "true" IWP via a 2d-histogram for the only-CLI case. The retrieved WP values agree almost exactly with the model "truth" values, except where they fall outside the LUT, which happens at 1860 g/m^2 (the value is arrived at from equation 3 for ice, assuming $r_e = 30$ μm and $\tau = 100$; see below). Note that for a cell to be accepted in the retrieval several criteria have to be fulfilled. Firstly, the clouds have to be optically thick, which means here that retrieved $\tau \geq 8$ has to hold, since, according to Roebeling et al. (2006), for the channel configuration used in the present study (0.6 μm and 1.6 μm), retrievals for clouds with $\tau < 8$ are unreliable. Secondly, there has to be an amount of IWP > 10 g/m^2 in the grid cell, which resembles the ice phase mask. Since in operational retrievals this is usually done by using an infrared window channel like SEVIRI's 10.8 μm channel (see e.g. Roebeling et al., 2006) which is not employed here, the IWP threshold is applied based on the model "truth" values and not on the retrieved values. Thirdly, as is common practice in operational retrievals (see e.g. Benas et al., 2017), the retrieved τ values are truncated at 100 and all grid cells with $\tau > 100$ are set to $\tau = 100$. These three criteria are applied to all the retrievals described in the present study. Where no information is given regarding sun-view geometry and ice cloud radiation scheme, the standard set-up described in section 3.3 (SeZA = 30°, SuZA = 45°, SeAA = 10°, and SuAA = 110°; *Deff* = 20 μm and *IceDe* = 60 μm) is employed.

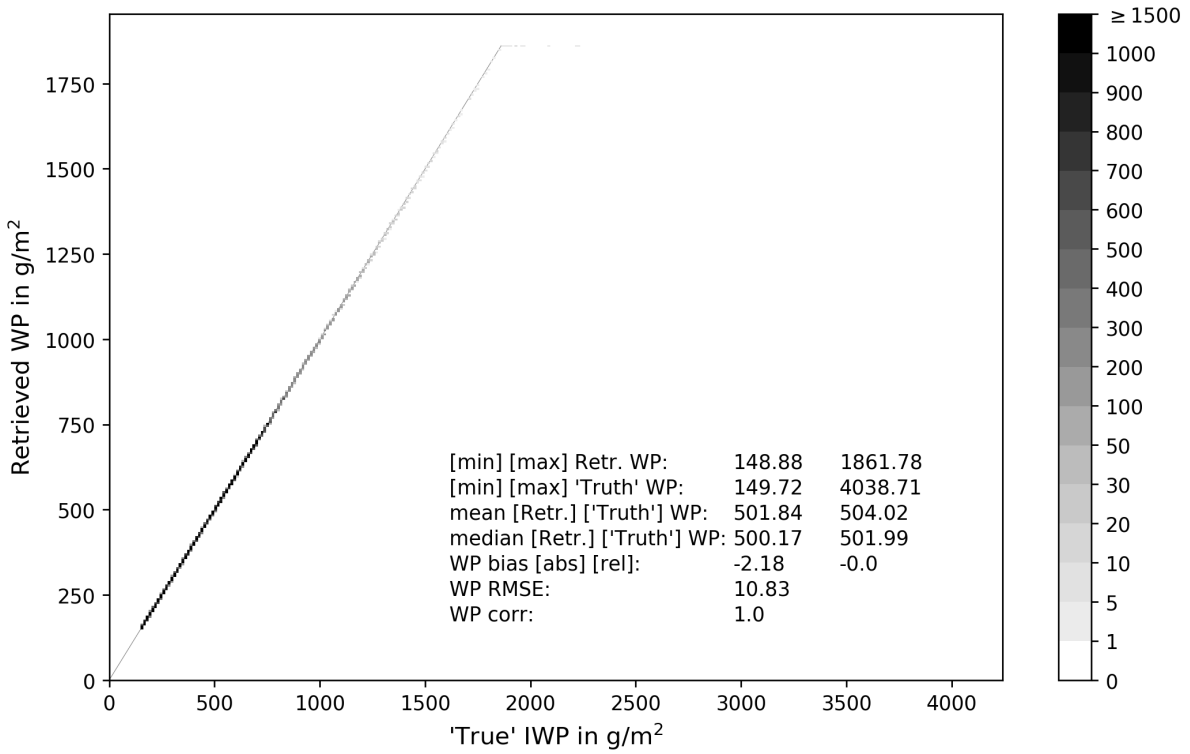

Figure 9: 2d-histogram showing the pixel-to-pixel comparison of the retrieved WP to the model "truth" IWP for 2015/07/05 16:00 UTC. The configuration corresponds to (C3) with only-CLI. This resembles the sanity-check case with the near-perfect retrieval result (for details refer to section 4.1.1).

4.1.2 Ice-Over-Liquid Configuration

Keeping both CLW and CLI (in the following referred to as CLW+CLI) in the (C3) configuration resembles an idealised deep-convective mixed-phase cloud (cf. Figure 8). This influences the retrieval result to quite some extent as becomes clear from Figure 10. The points in the plot are much more spread out than in Figure 9 and there are also many more values at the maximum (1860 g/m^2), which indicates that a lot of retrieved values fall beyond the truncation threshold of $\tau = 100$. Note that, except for very few values at the maximum, all retrieved values are either on the 1:1 line or above the 1:1 line, so that the line constitutes a lower bound on the values. The reason for this is that the cases where the values fall above the 1:1 line correspond to cells where there is in the atmosphere underneath the CLI at least some CLW which scatters back radiation that went through the overlying CLI and hence increases the retrieved τ which translates to a positively biased retrieval.

As described in section 2.3, the methodology applied in the current study allows to accurately discern between "true" LWP, IWP, and TWP. In Figure 11 the retrieved WP is again compared to the model "truth", but now to TWP. Similar to Figure 10, the values are more spread than in Figure 9, although now the values seem to fall mostly below the 1:1 line. So, conversely to the IWP-IWP comparison described above, the line constitutes kind of an upper bound on the values. The reason for this likely is that although, as seen in Figure 10, the re-

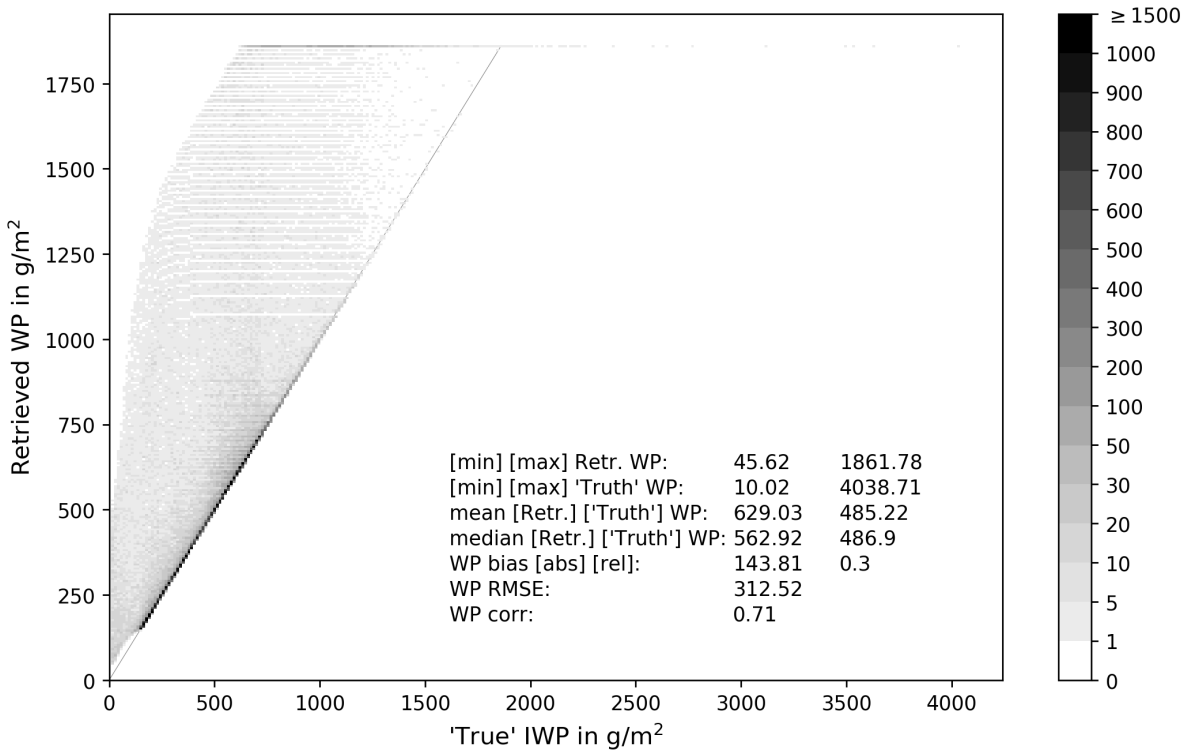

Figure 10: 2d-histogram showing the pixel-to-pixel comparison of the retrieved WP to the model "truth" IWP for 2015/07/05 16:00 UTC. The configuration corresponds to (C3) with CLW+CLI. For the only-CLI configuration cf. Figure 9.

trieval yields higher values compared to "true" IWP for columns with CLW+CLI, the CLW is still masked partly by CLI. Depending on the amount of CLI in the atmospheric column, some fraction of the radiation is already scattered back so that the radiation that can possibly be scattered by the underlying CLW is reduced and leads, in many cases, to an underestimation of τ which translates to a negatively biased retrieval. Looking more closely at the retrieval reveals that in some cases "true" TWP is actually overestimated by the retrieval. The reason for this is that there is only one retrieved r_e per atmospheric column and this value is assumed to be valid for the whole vertical extent of the cloud in the column. This means that when the retrieval algorithm calculates the WP from retrieved τ and r_e for ice-over-liquid clouds (according to equation 3) it assumes that the effective particle size of the liquid cloud is the same as for the overlying ice cloud. In the present configuration with $Deff = 20$ μm and $IceDe = 60$ μm retrieved CLI r_e would be 30 μm while the retrieved CLW r_e would be 10 μm. Since the 1.6 μm reflectances are mostly influenced by the overlying ice, the retrieved r_e is mostly close to 30 μm. Hence, the retrieved WP is calculated using an r_e that is a factor three too large for part of the actual cloud, which, assuming a fairly accurately retrieved τ, leads to overestimation of even the "true" TWP.

The described effect of CLW under CLI is visible quite distinctly in the image plots in Figure 12 (upper left panel), where the influence of the CLW on the retrieval is obvious. The visual impression is that the retrieval much better corresponds to the "true" TWP than to the

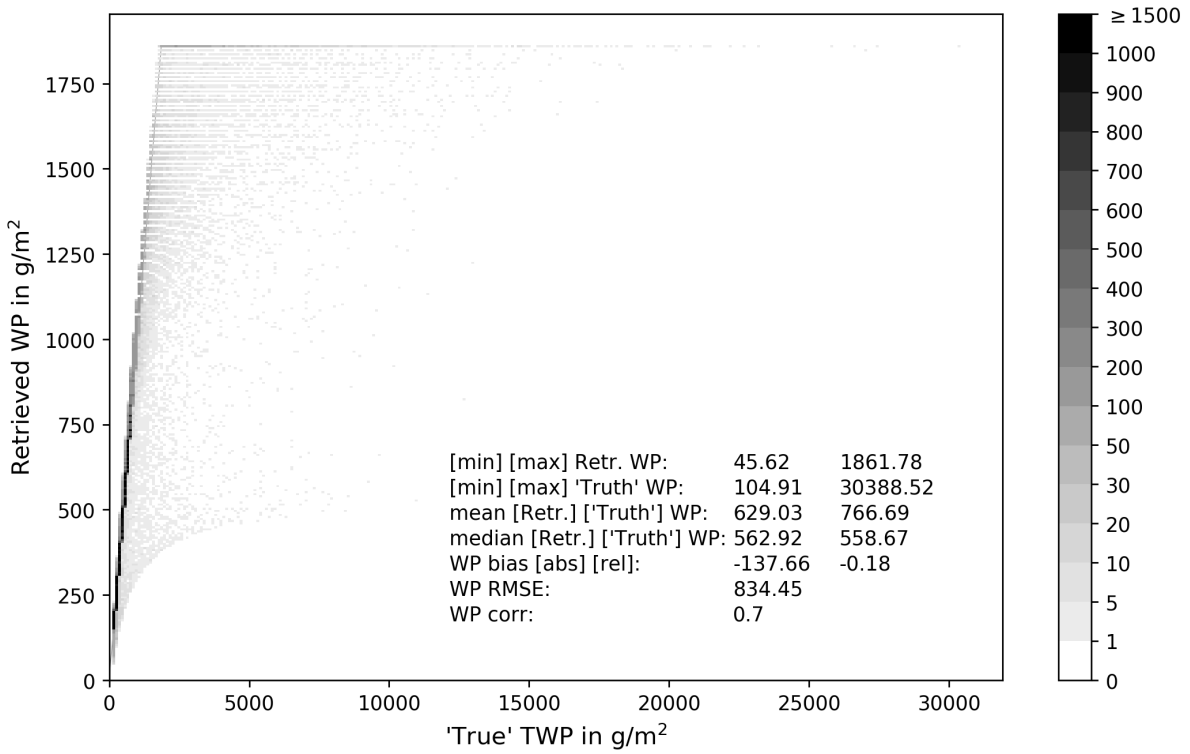

Figure 11: 2d-histogram showing the pixel-to-pixel comparison of the retrieved WP to the model "truth" TWP for 2015/07/05 16:00 UTC. The configuration corresponds to (C3) with CLW+CLI. For the comparison to "true" IWP cf. Figure 10.

"true" IWP. Note though, that Figure 12 just shows that the patterns correspond well, but the absolute values do not necessarily (see Figure 11). As shown in the statistics presented in Figures 10 and 11, the correlations of retrieval to "truth" are very similar for both IWP-IWP and IWP-TWP comparisons, with 0.71 and 0.70, respectively. This is likely due to the fact that, as is clear from the 2d-histograms, most of the values for both comparisons fall close to the 1:1 line. Note that these are mostly lower values.

Another way to analyse the retrieval in more detail is to make a LUT plot similar to Figure 1 and overlay it with a scatter-plot of the reflectances of the synthetic satellite image. This is done in Figure 13. There, the reflectances for the (C3) case on the one hand without CLW (only-CLI, black) and on the other hand with CLW (CLW+CLI, gray) are scattered onto the lines resembling the IWP LUT. For the only-CLI case, which is the sanity-check case, all reflectances, except at the high end where the truncation of $\tau = 100$ is reached, fall on a single line which corresponds to the $r_e = 30$ μm iso-line and is the same value chosen for the RTTOV calculation (Baum scheme), confirming the basic functionality of the retrieval. For the CLW+CLI case the situation seems quite different with much more variance and some reflectance pairs corresponding to iso-lines of $r_e < 10$ μm. The reason for this is that, even though an IWP mask (IWP > 10 g/m^2, see section 4.1.1) is applied in all cases, the reflectances of atmospheric columns where only thinner ice clouds are evident over liquid clouds are still strongly influenced by the liquid clouds. Hence, the reflectance pairs are shifted to correspond

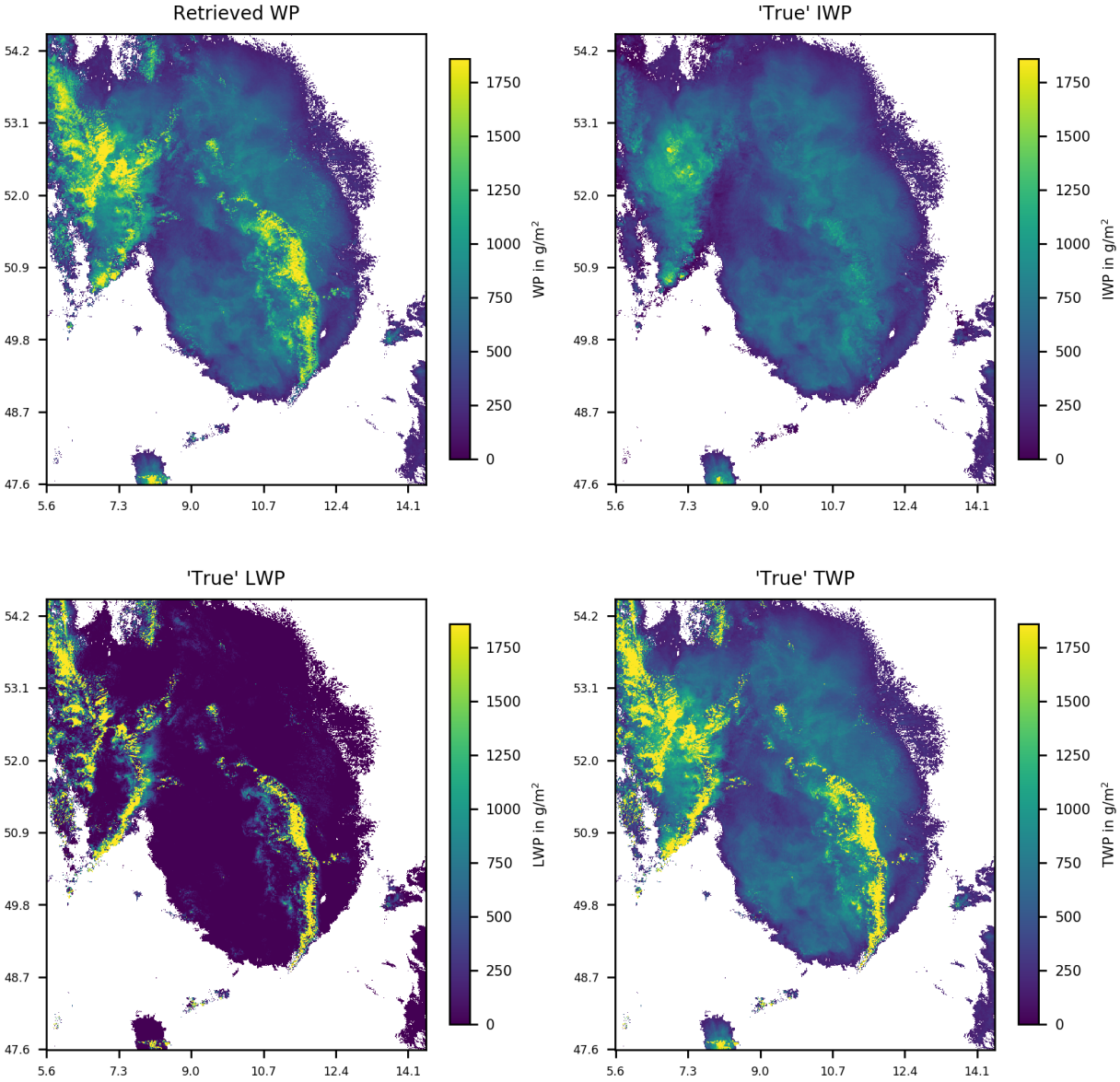

Figure 12: Image plots of retrieved WP (upper left), "true" IWP (upper right), "true" LWP (lower left), "true" TWP (lower right) for 2015/07/05 16:00 UTC. The configuration corresponds to (C3) with CLW+CLI used for the retrieval. Cf. Figure *A*.6 in the appendix.

to smaller r_e values in the LUT, sometimes even to the actual value used in the RTTOV calculation ($Deff = 20$ μm). However, the latter instances are most likely coincidental since, as explained in section 2.2, CLW and CLI need different LUTs and it cannot be expected that a reflectance pair corresponding to $Deff = 20$ μm would correspond to $IceDe = 20$ μm. Also, as the red line in the histogram in Figure 14 shows, the number of retrieved $r_e \neq 30$ μm is actually very small compared to the number of $r_e = 30$ μm.

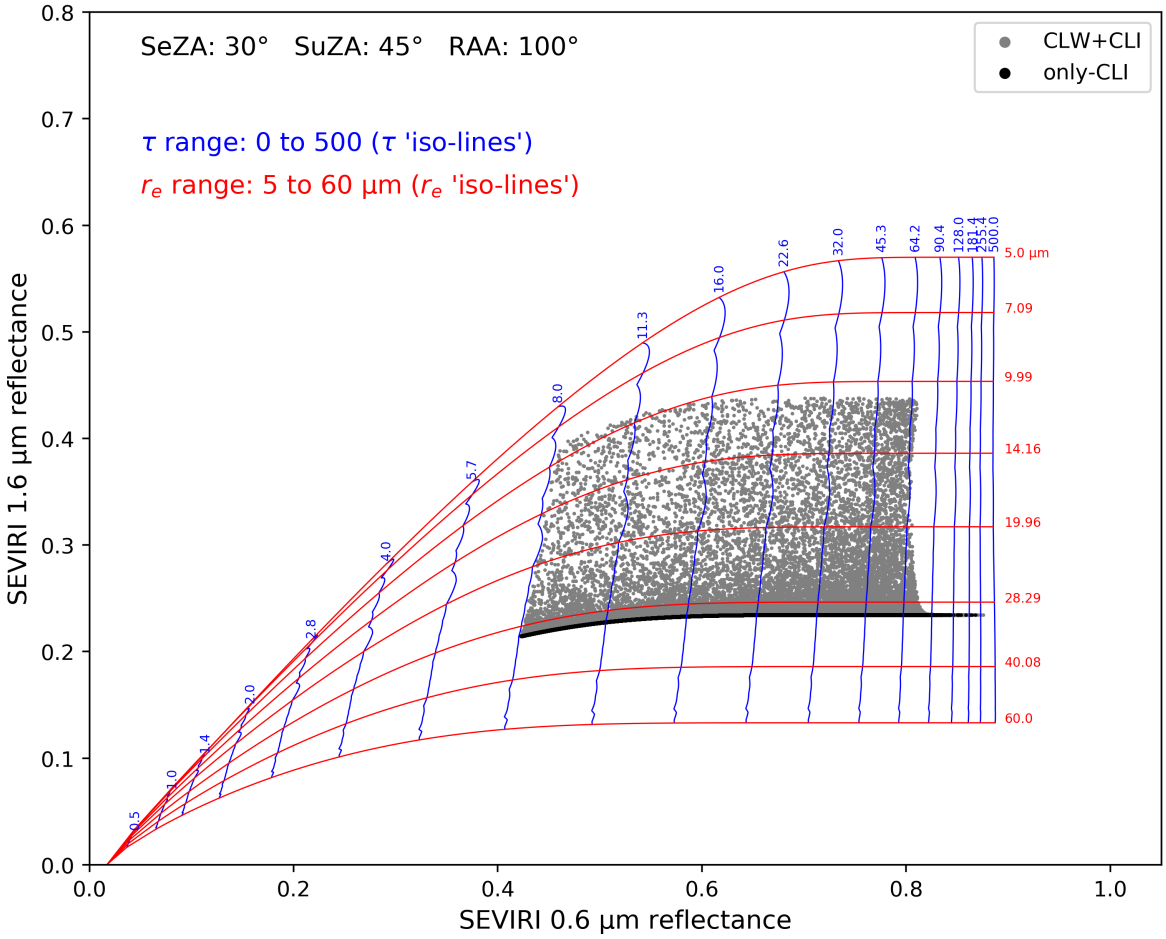

Figure 13: IWP LUT overlayed over reflectances of synthetic satellite images for 2015/07/05 16:00 UTC. Both correspond to configuration (C3) and on the one hand CLW+CLI (gray dots; cf. the red line in Figure 14 as well as Figures 10 and 11) and on the other hand only-CLI (black dots; cf. Figure 9).

4.1.3 Varied Atmospheric Profiles

Performing retrievals for configuration (C2) atmospheric input data should indicate the influence of different atmospheric profiles, especially different trace gasses. The influence on the retrieval is not very large, as can be seen in Figure 15 and from the statistics presented therein. Note that CLW was removed from the RTTOV calculation (only-CLI configuration) to isolate the effect of varying the atmospheric profile. The influence of the retrieval from CLW+CLI RTTOV input is larger, as will become clear in section 4.2.4. There is a slight negative bias

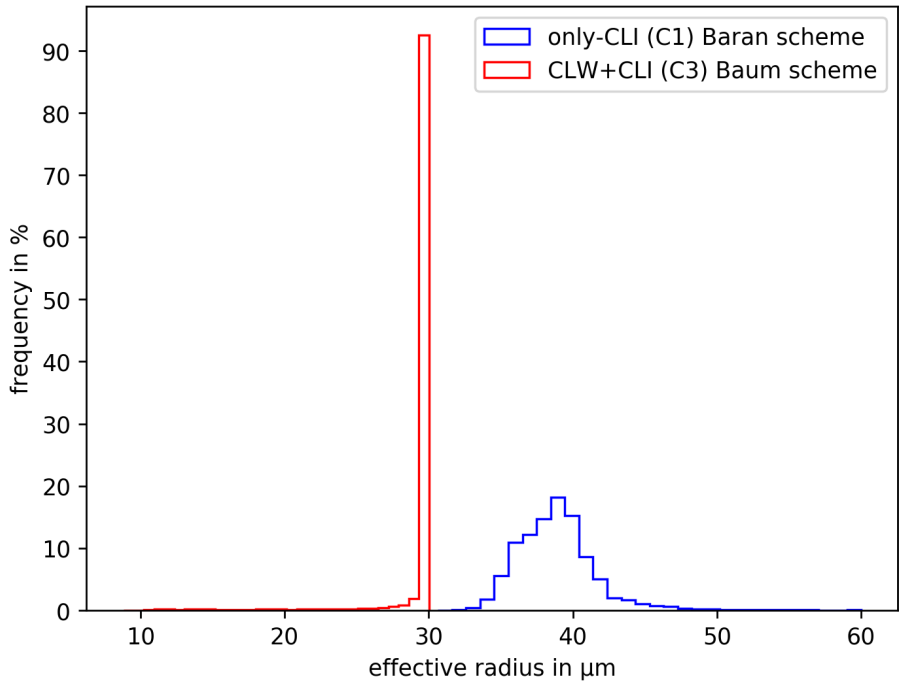

Figure 14: Histogram of retrieved r_e for CLW+CLI Baum scheme calculations from configuration (C3) data (red; cf. the gray dots in Figure 13 as well as Figures 10 and 11) and only-CLI Baran scheme calculations from configuration (C1) data (blue; cf. Figure 17 as well as Figure *A*.5 in the appendix) at 2015/07/05 16:00 UTC.

(−0.08) in the IWP retrieval which stems mostly from an underestimation of IWP at higher values. For lower values the retrieval coincides very closely with the "truth". 2d-histograms of retrieved τ exhibit the same pattern and the retrieved r_e are very close to 30 μm in almost all cases (both not shown). This means that the divergence from the near-perfect retrieval (Figure 9) is mostly caused by greater variance in the retrieval of τ, which mainly depends on the 0.6 μm channel reflectance. The divergence gets larger for larger reflectances, which results from the exponential dependence of τ on the 0.6 μm reflectance (cf. the LUT in Figure 1 and, additionally, Figure *A*.3 in the appendix). In fact, at high reflectance quite small changes in reflectance can cause quite large changes in retrieved τ. Given the here applied methodology of "condensing" the clouds in one layer per atmospheric column − they are condensed such that they all are situated at as similar as possible *geometric* height − their actual height in the atmospheric column with regards to pressure, water vapour and so on varies. Further RTTOV calculations have shown that cloud height has substantial impact on the retrieval (see Figure *A*.4 in the appendix). The reason for this is twofold. On the one hand it is the absorption of radiation by trace gasses (for the considered wavelengths these are mainly O_3 and water vapour) and on the other hand it is the Rayleigh scattering, that has a non-negligible impact on solar channels. Both depend on the amount of atmosphere above the clouds and indeed, RTTOV calculations with the atmosphere above the clouds removed yield much larger reflectances, especially in the 0.6 μm channel (not shown). Also, calculations with strongly reduced O_3

and water vapour result in higher reflectances but they do not correspond perfectly to the reflectances with removed above-cloud atmosphere, which confirms the influence of Rayleigh scattering. Furthermore, in the case with removed above-cloud atmosphere retrieved values at the lower end are actually smaller than in the standard case, which, again, confirms the Rayleigh scattering influence. This is because at lower reflectance Rayleigh scattering increases the reflectances, while at higher reflectance it reduces the reflectances.

However, RTTOV does not provide the functionality to completely turn off O_3, water vapour, or Rayleigh scattering, because the calculations are based on coefficients that are available only at certain value ranges (see section 3.2). Of course, removing the atmosphere above the clouds removes all three but they cannot be removed individually. Hence, it is not possible to precisely isolate the influence of these effects. Combined with the non-linear relationships of τ and r_e with the reflectances, which, importantly, restricts the meaningfulness of average values, this makes finding out exactly what is responsible for the negative bias in retrievals from configuration (C2) RTTOV input data compared to (C3) input data difficult.

Summing up this discussion regarding cloud height, it can be said that varying the atmospheric profile essentially means setting the cloud to slightly different heights which, in most cases does not influence the retrieval strongly, but becomes more relevant at higher reflectance. This becomes increasingly important in deep-convective ice-over-liquid clouds, which is further discussed in section 4.2.4.

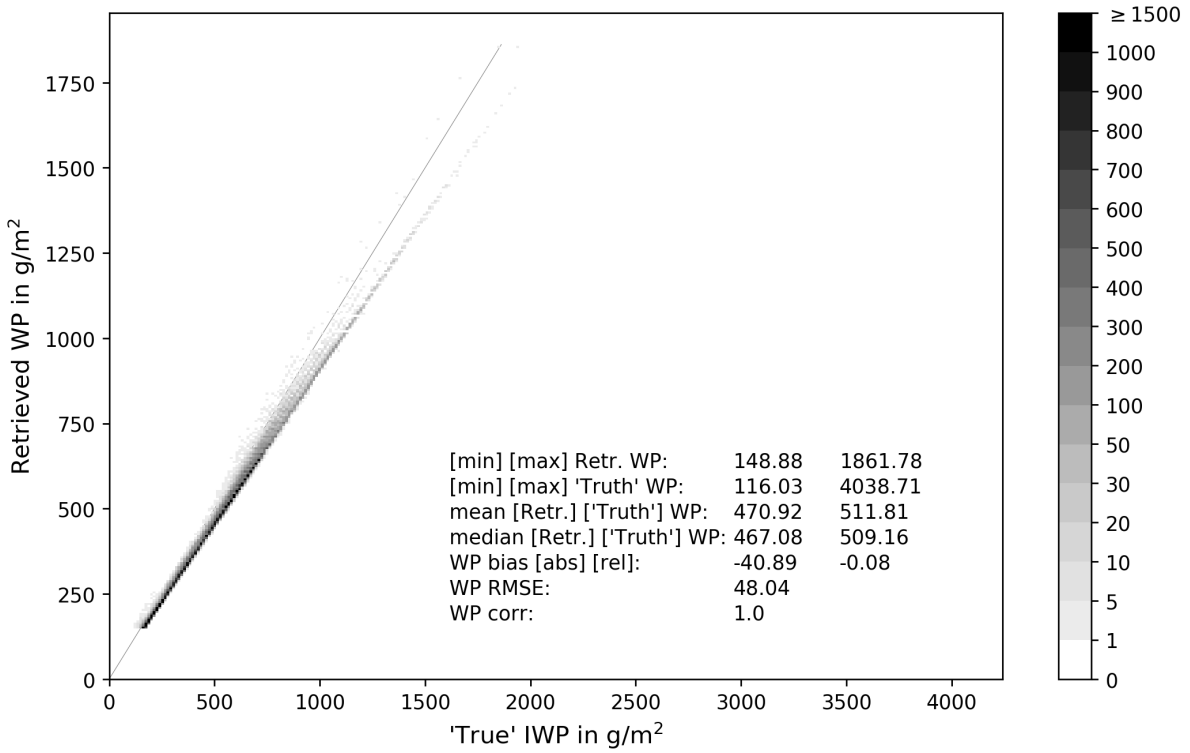

Figure 15: 2d-histogram showing the pixel-to-pixel comparison of the retrieved WP to the model "truth" IWP for 2015/07/05 16:00 UTC. The configuration corresponds to (C2) with only-CLI. For the (C3) results cf. Figure 9.

4.1.4 Full Clouds and Baran Scheme

The retrieval result compared to the "true" IWP for configuration (C1) only-CLI RTTOV input (cf. Figure 6) for a single time-step is shown in Figure 16. It is evident that, similar to the (C2) result described above, for smaller values the retrieval compares fairly well with the "truth" but for higher values it increasingly diverges from the 1:1 line. In this case though, the departure from the 1:1 line is not linear with increasing value but seems to be more exponential. Also, there are many more values at the retrieval maximum. The results for retrieved τ exhibit the same behaviour and the retrieved r_e varies only slightly by about 1 μm around 30 μm (not shown). It is clear from Figure 6 that the height of most of the CLI in configuration (C1) goes far beyond the height of 5.8 km assumed in the IWP LUT, often exceeding 12 km. As discussed regarding the (C2) configuration in the above text, this leads to less atmosphere above the clouds and thus less absorption by trace gasses as well as less Rayleigh scattering. Accordingly, the reflectances at 0.6 μm are higher (the 1.6 μm relectances are almost not affected), translating to increasingly higher retrieved τ and, finally, higher retrieved WP values. The generally higher reflectances due to higher clouds combined with the exponential relationship of τ and 0.6 μm (see Figure *A*.3 in the appendix) are likely responsible for the increasing deviation of the retrieved values from the 1:1 line in Figure 16.

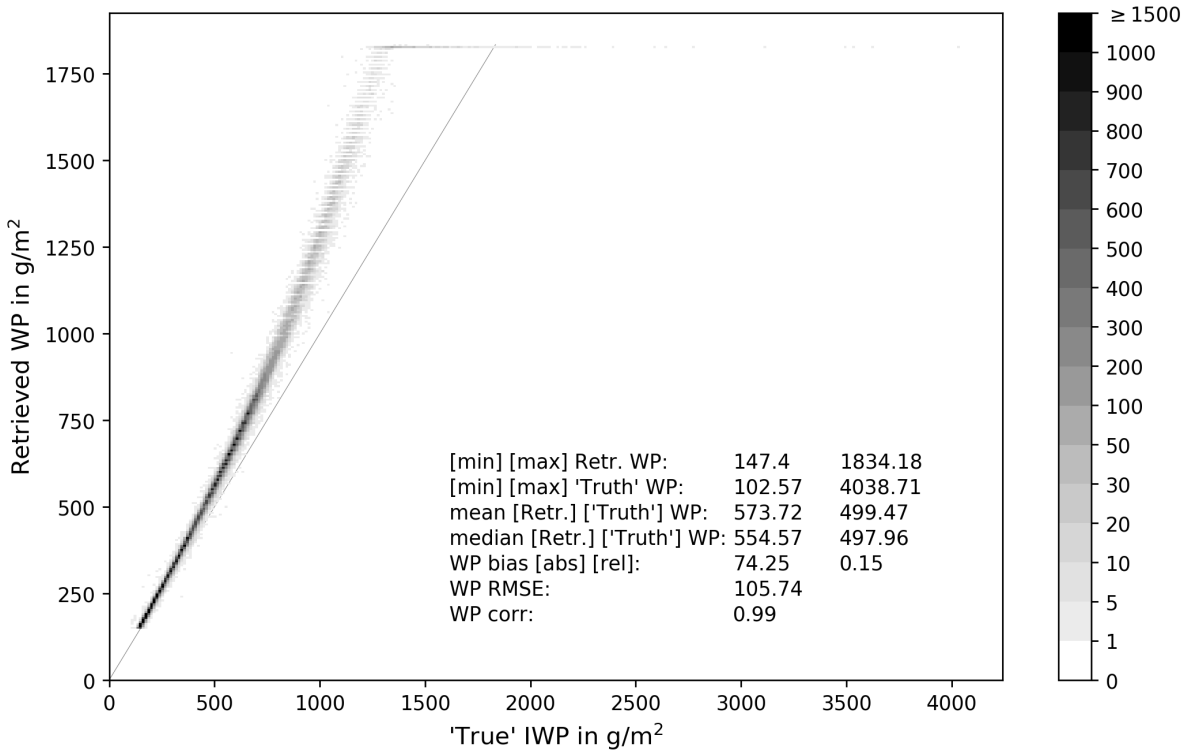

Figure 16: 2d-histogram showing the pixel-to-pixel comparison of the retrieved WP to the model "truth" IWP for 2015/07/05 16:00 UTC. The configuration corresponds to (C1) with only-CLI. For (C2) and (C3) results cf. Figures 15 and 9, respectively.

While for all previously discussed cases at least the smaller retrieved values show good

agreement with the "truth", using the Baran scheme to calculate the scattering by CLI in RTTOV leads to more variation, even at lower values, as well as a general positive offset (see Figure 17). It is also evident that the retrieved WP reaches much higher values (up to > 3000 g/m^2) than in the other cases and exhibits a more cloud-like clustering of values at the high end in the 2d-histogram, whereas in the previous cases this looks more like a hard cut-off. Examining the corresponding 2d-histogram for retrieved τ shows that this actually looks more similar to the previous cases with less spread and hard a cut-off at the high end while the general offset is still evident (not shown). The divergence from the 1:1 line is larger than for the (C1) Baum scheme case but the slope of the τ values is smaller than that of the retrieved WP values. Note though that the applicability of this τ comparison (retrieved τ v. "true" τ) is limited for the Baran scheme since "true" τ is just derived from "true" IWP (in the only-CLI case) via rearranging equation 3 and isolating τ. Hence, the vertical homogeneity assumption goes into the calculation of "true" τ as well as the assumption of one specific r_e. This is plausible for the Baum scheme since there radiative transfer calculations are based on a given effective particle size but the Baran scheme does not work with particle sizes (see section 3.2) which makes the methodology less plausible.

Examining where the reflectances fall in the LUT (see Figure $A.4$ in the appendix) as well as a histogram of retrieved r_e (blue line in Figure 14), it turns out that there is a much larger spread in the retrieved r_e values which distribute almost Gaussian-like around a value slightly below 40 μm with a longer tail on the right hand side reaching values of $r_e > 50$ μm. This spread in retrieved r_e causes the spread in the retrieved WP values compared to the previous cases and the generally higher r_e values cause the increased slope of WP compared to τ.

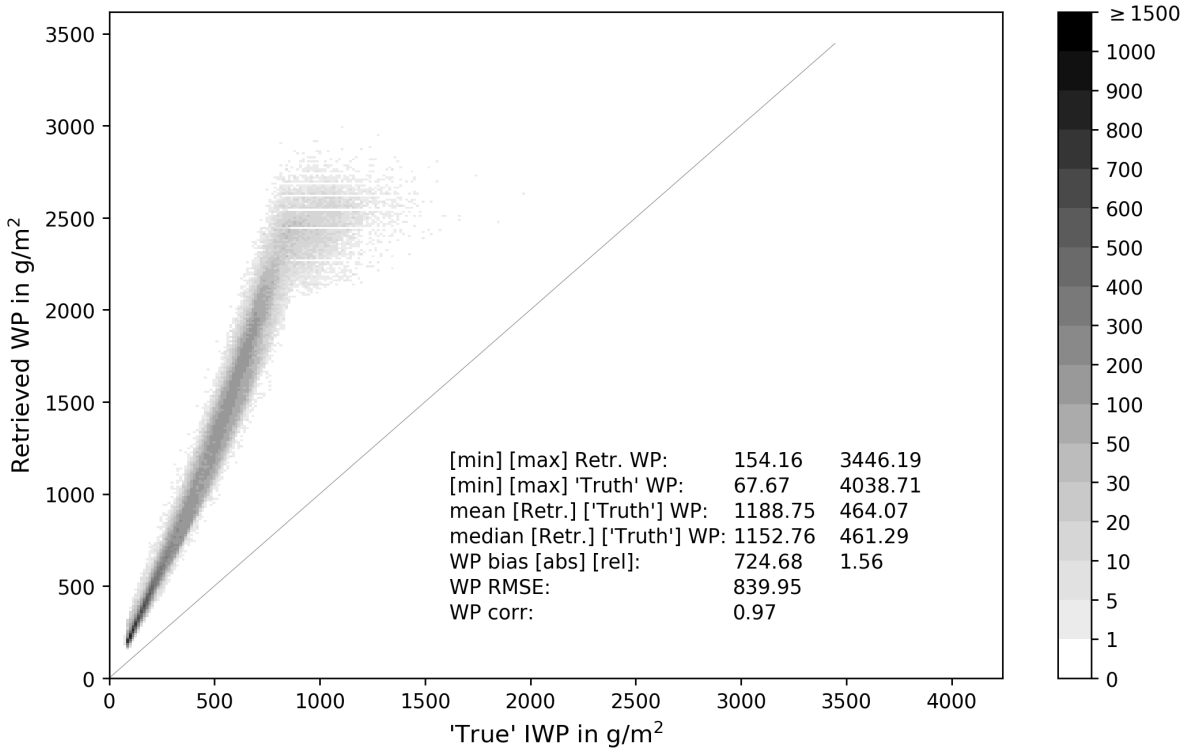

Figure 17: Same as Figure 16 but with Baran ice cloud scheme.

4.1.5 Varied Ice Effective Diameter

Investigating the Baum scheme more deeply reveals some interesting properties that should be pointed out. Because of the way LWP and IWP depend on τ and r_e the choice of *IceDe* in the Baum scheme in RTTOV has considerable effects on the resulting reflectances and, by extension of this as well as because of how r_e factors in the retrieval (see equation 3), on the retrieved LWP and IWP. Figure 18 illustrates how changing the *IceDe* from 20 μm to 60 μm and then to 100 μm (in the following referred to as *IceDe20*, *IceDe60*, and *IceDe100*, respectively) affects retrieved WP (left) and τ (right). All three cases correspond to configuration (C3) with CLW+CLI and the "Deff" scheme assuming *Deff* = 20 μm applied for CLW (like in all other CLW+CLI cases discussed in the present study). Increasing the *IceDe* while keeping IWP constant will decrease τ and hence the 0.6 μm reflectance. This explains the decrease of cloud covered area in accordance with the increase in assumed *IceDe* in the Baum scheme. The reason is that, as in all other retrievals presented in this study, a minimum retrieved τ threshold of 8 is applied (see section 4.1.1). Cells with retrieved $\tau < 8$ are rejected by the retrieval algorithm and not classified as cloud, which is most often true at the edges of the cloud. A further effect of assuming different *IceDes*, and hence different τ, is clearly evident from the central areas of the cloud in the top row in Figure 18. There are many more cells with retrieved $\tau = 100$ in the top right panel with *IceDe20* than in the other two cases. Furthermore, there is a larger amount of high values in the middle right panel (*IceDe60*) than in the lower right panel (*IceDe100*). Conversely though, as is evident from the left hand side of Figure 18, the retrievals of IWP for *IceDe20* (maximum IWP $\approx$ 620 g/m^2) only reach much lower values than for *IceDe60* (maximum IWP $\approx$ 1860 g/m^2) and both reach lower values than for *IceDe100* (maximum IWP $\approx$ 3020 g/m^2). From Figure 18 and Figure 12 it is clear that assuming larger *IceDes* in ice-over-liquid clouds leads to the shape of the underlying CLW being much better visible than when smaller *IceDes* are assumed. In the synthetic satellite image in Figure 4 the thin band of liquid cloud is actually also visible underneath the ice cloud since there *IceDe60* is assumed. In contrast, for the synthetic satellite image in Figure 3 no liquid clouds (which are in evidence, see Figure *A*.6 in the appendix) seem to be visible underneath the ice cloud. The Baran scheme is used for this image. Note that the reflectances in both images are calculated from configuration (C1) RTTOV input. As described above, the Baran scheme tends to overestimate τ due to CLI which explains why the ice clouds obscure the underlying liquid clouds in Figure 3.

This translates to the fact that the larger the *IceDe*, the worse the correspondence between retrieved WP and "true" IWP. Conversely though, assuming a larger *IceDe* leads to a better correspondence of the retrieved WP to the "true" TWP. The statistics presented in Table 2 bear this out. For *IceDe20* it seems clear that the retrieved WP corresponds much more closely to the "true" IWP than TWP. For *IceDe100* it is the other way round, even though the correspondence of retrieved WP to "true" TWP is less good than that of retrieved WP to "true" IWP in the *IceDe20* case. Note that the root mean square error (RMSE) for "true" IWP is always smaller than for "true" TWP. This is because of some few very high values of "true" TWP (up to 30000 g/m^2, also see Figure 11). The relative bias in both cases is still

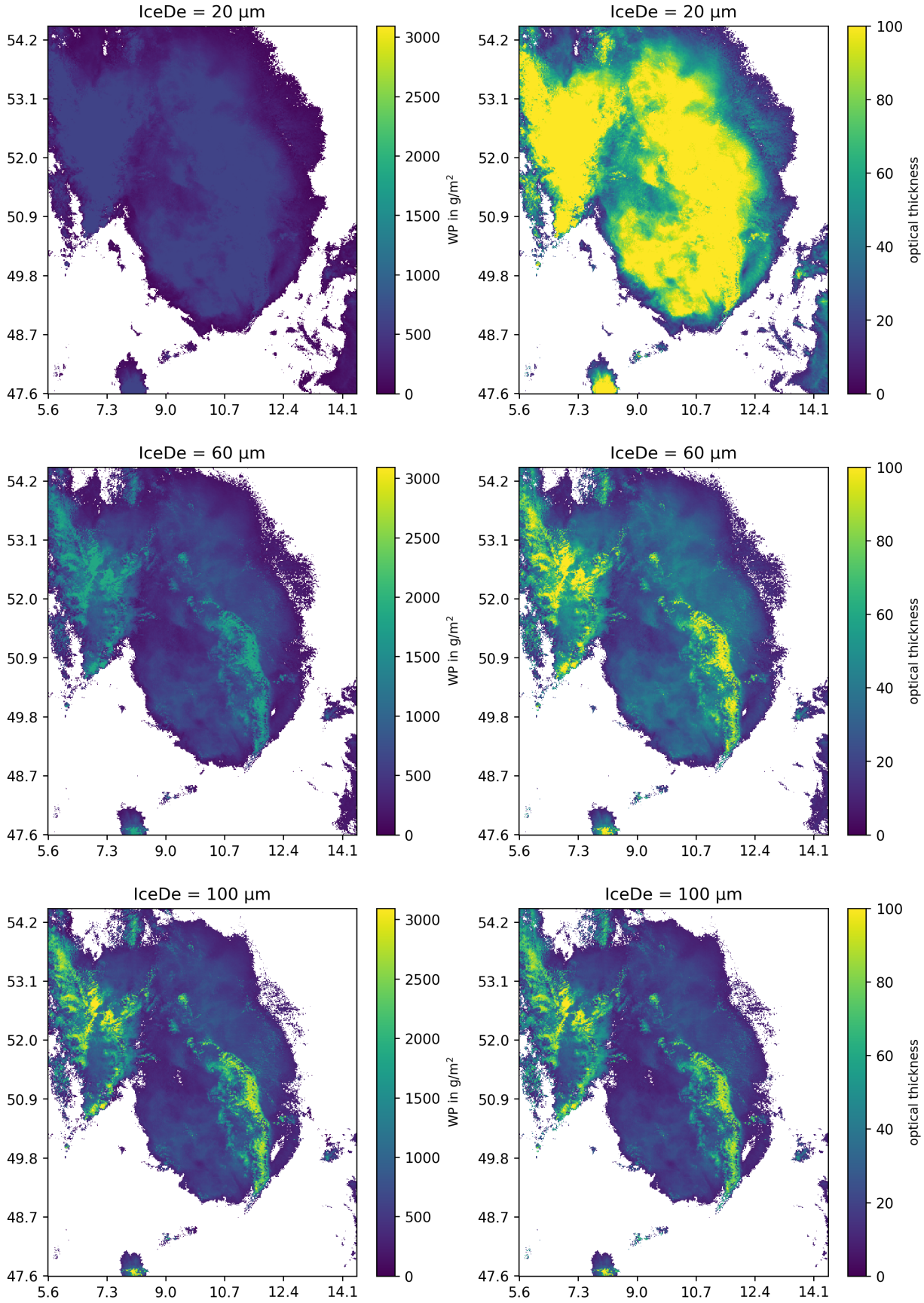

Figure 18: Comparison of the effect of assuming different ice effective diameters on retrieved WP (left) and retrieved τ (right). All panels correspond to configuration (C3) data with CLW+CLI. See Table 2 for statistics.

Table 2: Statistics of the retrieval compared to "true" IWP and TWP assuming three different ice effective diameters. All values correspond to configuration (C3) data with CLW+CLI. Cf. Figure 18.

statistic/IceDe	20 μm	60 μm	100 μm
relative bias IWP	-0.05	0.3	0.53
RMSE IWP	128.57 g/m^2	312.52 g/m^2	577.26 g/m^2
correlation IWP	0.89	0.71	0.52
relative bias TWP	-0.39	-0.18	-0.05
RMSE TWP	973.74 g/m^2	834.45 g/m^2	773.14 g/m^2
correlation TWP	0.42	0.70	0.74

at the same level (-0.05). For *IceDe60* the situation is less clear. The correlation is almost the same for both "true" IWP and TWP (0.71 and 0.70, respectively) and while the RMSE is much higher for "true" TWP (834.45 g/m^2 v. 312.52 g/m^2), the relative bias (neglecting the sign) is almost only halve that of "true" IWP (-0.18 v. 0.3). In this case no clear distinction can be made.

4.2 Domain-Mean Comparison

In this section the domain-means of the retrieval results and their comparison to the model "truth" with regards to the influence of ice-over-liquid configuration, different assumptions about the *IceDe* in the Baum scheme, sensor noise and bias, varied SuZA, and using different ice schemes are discussed.

The domain-mean corresponds to the all-sky mean of the model domain and is calculated by first filling all the cells that were rejected by the retrieval algorithm (see section 4.1.1 for the criteria) and hence classified as clear-sky with the value zero and then taking the mean value over all the cells in the domain. As before, the day chosen is 2015/07/05 and the investigated time period is 10:00 UTC to 18:45 UTC. Note that, to reduce the complexity, the sun-view geometry, unrealistically, is kept constant over the whole period except for the cases where the influence of SuZA is investigated.

4.2.1 Ice-Over-Liquid Configuration and Bias

Figure 19 shows the development of a few different retrieval configurations (continuous lines) compared to the "true" values of LWP, IWP, and TWP (dashed lines). The retrievals correspond to RTTOV input data in configuration (C3). The ice scheme used for the RTTOV calculations is Baum with *IceDe60*.

It is clear that while in the morning there is only little CLI and almost no CLW, over the course of the day a large ice-over-liquid cloud system forms with peak domain-mean values exceeding 400 g/m^2 (the in-cloud means exceed 750 g/m^2). The mean values of LWP are much lower than that of IWP which results from the much smaller area covered by CLW than by CLI

(cf. Figure 12). LWP peaks at about 16 UTC while IWP peaks at about 17 UTC, causing the TWP to plateau in the hour between. The "true" IWP line in Figure 19 is almost not visible because it is obscured by two other lines: The only-CLI retrieval (black) and the only-CLI retrieval from negatively biased reflectances (red). This is done such because it illustrates on the one hand the accuracy of the near-perfect retrieval and shows on the other hand that a -4 % negative bias in the reflectances (assuming the only-CLI configuration) does not affect the retrieval much. The probable reason for this is that, as previously discussed, smaller reflectances in the 0.6 μm channel lead to smaller retrieved τ, while smaller reflectances in the 1.6 μm channel lead to larger retrieved r_e. In the configuration presented here, both effects seem to cancel each other out and hence lead to a unbiased retrieval. For the positive bias the situation is different. The retrieval from positively biased reflectances, while for the first hour (10 to 11 UTC) very close to the "truth", later diverges and reaches peak divergence when the IWP domain-means themselves peak at around 17 UTC. The reason for this probably lies in the exponential dependence of retrieved τ on the reflectances. At high 0.6 μm reflectance a small positive change in reflectance translates to a much larger positive change in retrieved τ. In contrast to the situation with negatively biased reflectances, this is not compensated by the reduction in retrieved r_e due to the increased 1.6 μm reflectance, because the relationship in the reflectance interval in question is much less extreme than that for retrieved τ and 0.6 μm reflectance (see Figure $A.3$ in the appendix).

The green continuous line in Figure 19 represents the all-sky domain-means of the retrievals from CLW+CLI RTTOV input. It is obvious that due to the CLW underneath CLI this retrieval deviates more strongly from the "true" IWP than even the retrieval from positively biased reflectances. The absolute (continuous with "$\times$"-markers) and relative (dashed with filled circle markers) differences between CLW+CLI retrieval and "true" IWP (blue) and "true" TWP (black) are depicted in Figure 20. "True" IWP is always overestimated while "true" TWP is always underestimated. The absolute differences to both "true" IWP and TWP are quite small in the morning (ca. 5 and -5 g/m^2, respectively) but steadily rise and reach ca. 80 g/m^2 (-80 g/m^2) at their peaks in the afternoon. With regards to "true" IWP the difference plateaus there at first and only slowly declines to about 70 g/m^2 at the end of the time-series. Conversely, for TWP the peak difference of -80 g/m^2 remains but for a very short time and the difference quickly decreases to only about -20 g/m^2 at the end of the time-series. The relative errors exhibit less variation over the whole period. For "true" IWP the error is always positive and starts at about 15 % followed by a rapid increase to 30 % with a slower decline to slightly over 20 % afterwards and finally some meandering between 25 % and 30 %. The "true" TWP error is always negative and starts at (omitting the sign) below 10 % with an increase till noon of (at peak) 20 % followed by meandering between 15 % and 20 % and finished by a decline in the afternoon to roughly 5 % at the end. Overall, the retrieval corresponds better to the "true" TWP with mean absolute and relative differences of -32.53 g/m^2 and -14.26 %, respectively, compared to 44.38 g/m^2 and 25.68 % with regards to "true" IWP.

Summarising, in the present case having CLW present under CLI influences the retrieval

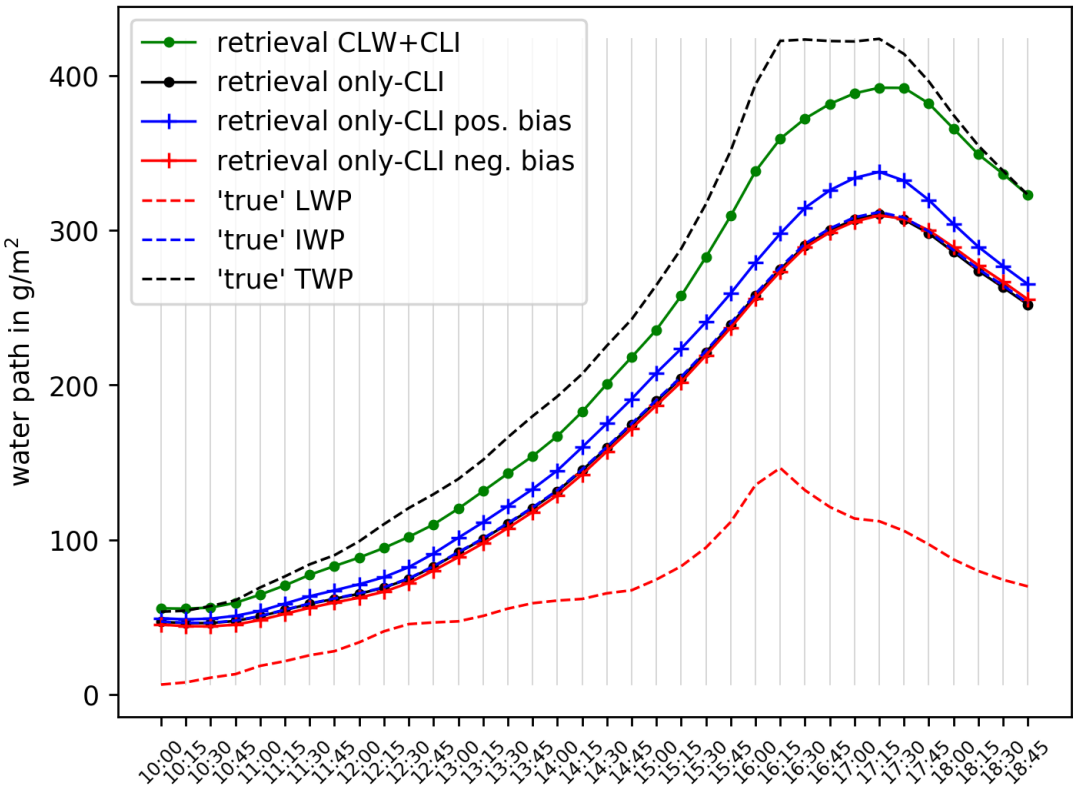

Figure 19: All-sky domain-mean time-series. The dashed lines correspond to the "true" LWP (red), IWP (blue), and TWP (black). The continuous lines with markers correspond to the retrievals: only-CLI retrieval assuming perfect sensor (black with filled circle markers), only-CLI retrieval from negatively biased reflectances (red with "+"-markers), only-CLI retrieval from positively biased reflectances (blue with "+"-markers), CLW+CLI retrieval assuming perfect sensor (green with filled circle markers). All retrieval correspond to configuration (C3) data.

more strongly than a positive or negative bias in the only-CLI reflectances and the CLW+CLI retrieval corresponds slightly better to TWP than IWP, even though the differences to TWP are still considerable.

4.2.2 Varied Ice Effective Diameter

As discussed for a single case in section 4.1.5 and shown in Figure 18, the retrieval results considerably depend on the choice of *IceDe* when using the Baum scheme in RTTOV. This holds true for the complete time-series, as discussed in this section. Figure 21 compares the retrieval from the reflectances calculated for *IceDe20* (red), *IceDe60* (black), and *IceDe100* (blue) to "true" IWP (dashed) and TWP (dotted). Note that the domain-mean values of "true" IWP and TWP vary depending on the choice of *IceDe*. This is because of the minimum retrieved τ threshold applied to the retrieval, as explained previously in section 4.1.5. Importantly, this also affects the lines in Figure 19 and, to be more exact, there would have to be four lines for each "true" LWP, IWP, and TWP in that figure. But because these deviate only slightly from

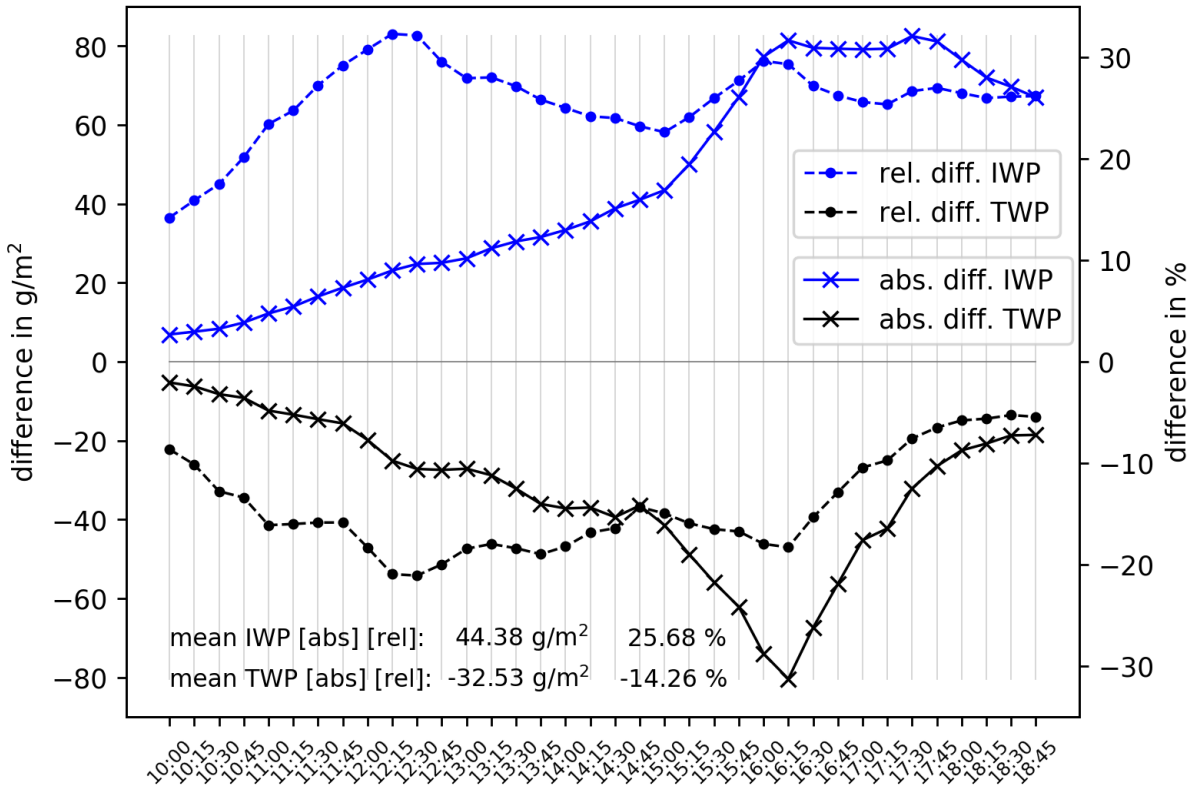

Figure 20: Absolute (continuous with "×"-markers) and relative (dashed with filled circle markers) differences between "true" IWP and retrieval (blue) as well as "true" TWP and retrieval (black). The differences correspond to the green line and the dashed blue and black lines, respectively, in Figure 19.

the present lines, and for the sake of simplicity of depiction, they are not shown in the figure. For the calculations of the differences shown in Figure 20 the actual corresponding values of "true" IWP and TWP are used. The justification for not having the same "truth" data in every case is that this would show the impact of the cloud detection which is not the main aim of the study. Furthermore, for the different cases considered here, the impact does not seem to be large, and where the impact seems non-negligible it is made clear (e.g. in Figure 21).

Table 3: Mean values of the absolute and relative differences of retrieval to "true" IWP and TWP assuming three different ice effective diameters corresponding to Figures 21 and 22.

diff. type/IceDe	20 μm	60 μm	100 μm
IWP [abs.]	-9.39 g/m^2	44.38 g/m^2	74.84 g/m^2
TWP [abs.]	-86.63 g/m^2	-32.53 g/m^2	-1.89 g/m^2
IWP [rel.]	-4.55 %	25.68 %	48.78 %
TWP [rel.]	-32.78 %	-14.26 %	-3.23 %

In section 4.1.5 it is concluded that the *IceDe20* retrieval result corresponds closely to the "true" IWP, while the *IceDe100* result resembles the "true" TWP quite well. For *IceDe60* the

distinction is less clear. These conclusions are equally valid for the complete time-series, as discussed here. The differences between "true" IWP and TWP to the retrieval results for the different *IceDes* are shown in the top and bottom panels of Figure 22, respectively. Their mean values are presented in Table 3. The choice of *IceDe20* leads to an underestimation (always > -10 %) of IWP for almost the complete time-series adding up to a -4.55 % time-series mean difference while the other two *IceDes* lead to constant overestimation culminating in about a quarter (*IceDe60*) and one half (*IceDe100*) overestimation. Notably, the absolute as well as the relative time-series difference lines of *IceDe60* and *IceDe100* have a very similar shape while this is not true for the *IceDe20* line. This indicates that for the two larger *IceDes* the CLW has some influence while at *IceDe20* CLW is basically not "seen" by the satellite sensor. Regarding TWP, *IceDe100* causes underestimation of between -10 % and -5 % until the afternoon, when the time-series shifts to overestimation of slightly lower than 10 %. This leads to a very low overall mean difference of -3.23 %. Both smaller *IceDes* cause constant larger underestimations reaching minimum values of -20 % (*IceDe60*) and -40 % (*IceDe20*), retaining values close to these from noon until afternoon and causing time-series mean differences of -14.26 % and -32.78 %, respectively. Considering their general shape, the difference curves with regards to TWP look quite similar, although the dip at 16:15 UTC is very strongly pronounced for *IceDe20* and almost non-existent for *IceDe100*. Notably, the dip coincides with the maximum of LWP for the time-series (cf. Figure 19). Similar to the above discussion, this indicates that CLW is not "seen" by the satellite sensor and hence cannot be retrieved, which leads to an underestimation of LWP and, consequently, to an underestimation of TWP. Again, as in section 4.1.5, it is not clear what the *IceDe60* retrieval corresponds to best, but considering the overall mean values (-14.26 % v. 25.68 %), it might be advisable to consider the retrieval as TWP with a roughly -15 % underestimation.

In conclusion it can be said that the results from varied *IceDe* in the domain-mean are similar to the results discussed in section 4.1.5. Both more "extreme" cases (*IceDe20* and *IceDe100*) correspond distinctly better to one of the "true" quantities (IWP and TWP, respectively), while for the "middle", more commonly used (see section 3.3), case (*IceDe60*) it is less clear.

One feature that stands out from the *IceDe100* retrieval domain-means and differences plots (Figures 21 and 22, respectively) is that in the afternoon the retrieval overestimates even the "true" TWP. The reason for this is already explained in section 4.1.5 regarding *IceDe60*, as being a result of the assumption of one effective particle size for the complete vertical cloud extent. For *IceDe100* the effect is even more pronounced than in the *IceDe60* case, because the retrieved *IceDe* is even larger than the actual effective diameter of the underlying liquid clouds (100 μm v. 20 μm). Consequently, the *IceDe100* domain-mean retrievals overestimate "true" TWP sometimes, while for *IceDe60* the domain-means are always lower than "true" TWP. As described in section 4.1.5, there is some overestimation for single atmospheric columns in the *IceDe60* case, but it never suffices for an overestimation in the domain-mean.

A further question arising in the present case is why the overestimation of "true" TWP for

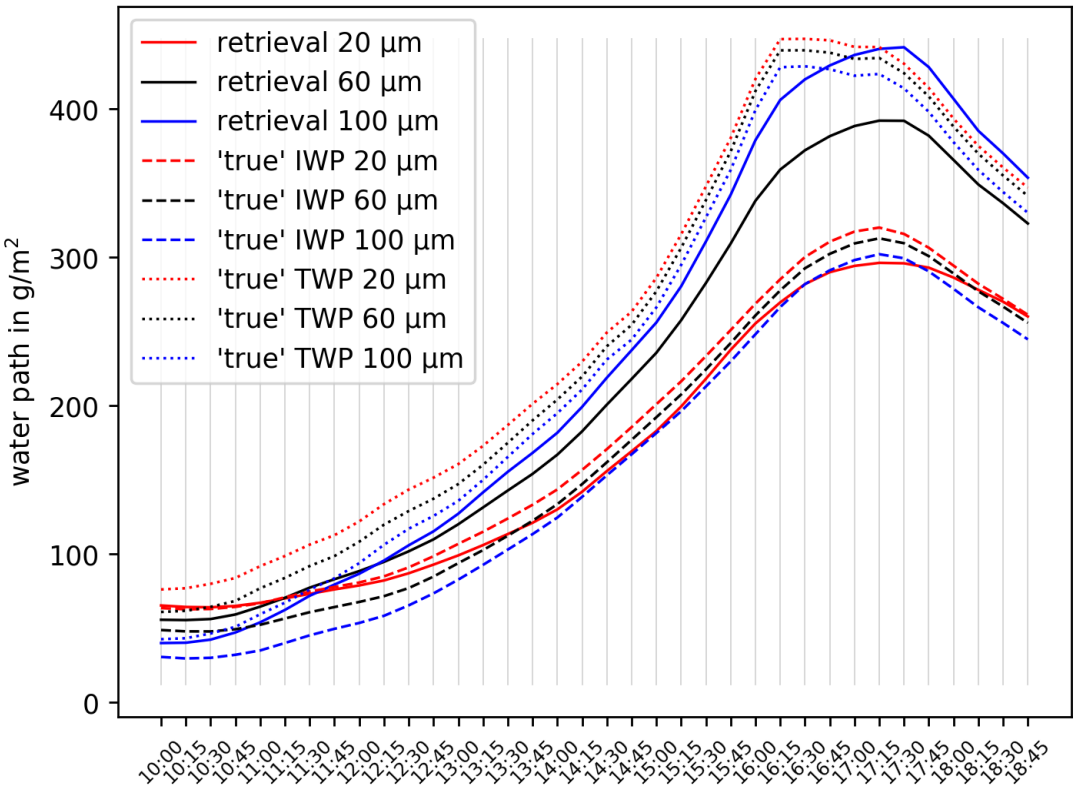

Figure 21: All-sky domain-mean time-series of retrieval (continuous) and "true" IWP (dashed) and TWP (dotted) for *IceDes* 20 μm (red), 60 μm (black), and 100 μm (blue). All values correspond to configuration (C3) data with CLW+CLI. Cf. Figure 22 for the time-series differences and Table 3 for statistics.

IceDe100 is only evident in the late afternoon and not earlier. This seems to be a feature of the masking of CLW by CLI and the incapability of the retrieval to account for the CLW under CLI sufficiently. Comparing retrieved τ with "true" total τ and τ due to CLI alone (short IW-τ) it is evident that, while total τ is always underestimated and IW-τ always overestimated, retrieved τ correlates much better with IW-τ than with total τ (see Figure *A*.7 in the appendix for the *IceDe100* case). For *IceDe100* "true" total τ is strongly influenced by τ due to CLW alone (short LW-τ), since assuming *IceDe* = 100 μm as well as the relationship in equation 3 yields relatively small values of τ compared to the ones yielded by assuming *Deff* = 20 μm. In the late afternoon LWP and LW-τ decline quite strongly after peaking at 16:15 UTC, but, because of the explained dependence on "true" IW-τ, retrieved τ declines only very slightly. Additionally, at the time when "true" LWP is declining, domain-mean retrieved r_e reaches its peak. The reason is probably that while the fraction of cells with LWP > 0 stays the same (e.g. 49.27 % at 16:15 UTC v. 49.85 % at 17:30 UTC), the amount of LWP in these cells decreases (54.3 % of TWP at 16:15 UTC v. 45.7 % of TWP at 17:30 UTC), reducing the influence of CLW on the reflectances so that they tend to be influenced more strongly by CLI. Hence, the retrieved r_e in these cells increasingly approaches *IceDe*/2 which is larger than *Deff*/2, translating into higher retrieved WP. The combined effect of retrieved τ dependence on "true" CLI and increasing retrieved r_e due to the declining influence of "true" CLW as well as the

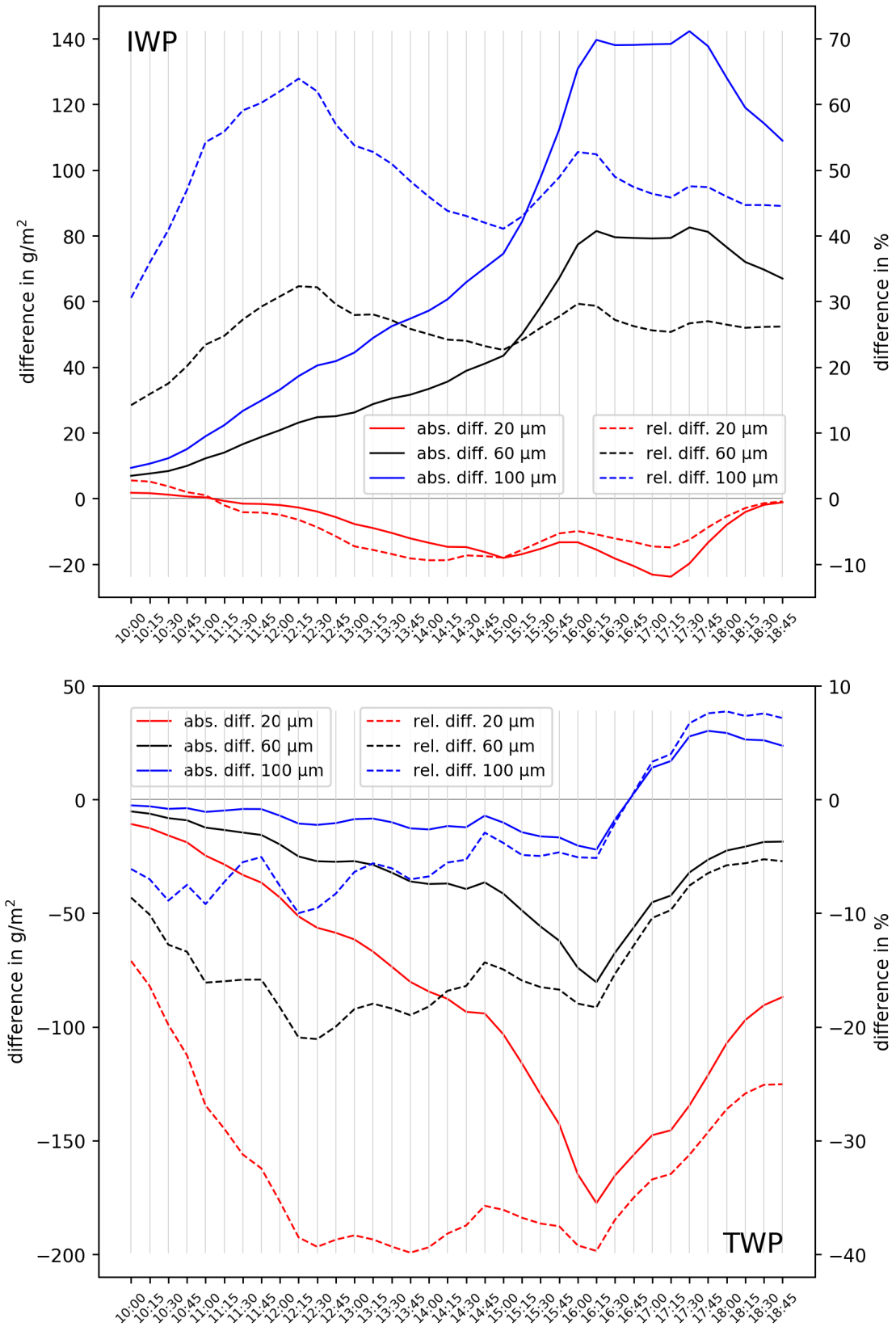

Figure 22: Absolute (continuous) and relative (dashed) differences of all-sky domain-mean time-series of retrieval and "true" IWP (top) and TWP (bottom) for *IceDes* 20 μm (red), 60 μm (black), and 100 μm (blue) corresponding to the Figure 21. See Table 3 for statistics.

high importance of "true" LWP for "true" TWP leads to the overestimation of "true" TWP by the *IceDe100* retrieval in the late afternoon of the domain-mean time-series.

Concluding the preceding discussion, it seems to be suggestible to recognise that in cases where the retrieval corresponds to the "true" TWP, which, here, are necessarily cases with higher *IceDe*, it depends substantially on the underlying CLW if the retrieval over- or underestimates "true" TWP. Without prior knowledge of CLW it might not be possible to overcome this uncertainty in the retrieval.

4.2.3 Varied Sun Zenith Angle, Bias, and Noise

Figure 19 depicts, i.a., the only-CLI retrieval from positively and negatively biased reflectances, which exhibits small overestimation for the former while the latter has almost no impact. As is evident in Figure 23, for the CLW+CLI retrieval (blue and red lines with filled circle markers) the impact of a bias is larger. The corresponding time-series differences are shown in Figures $A.8$, $A.9$, and $A.10$ in the appendix. Note that the differences in these figures as well as the ones referred to here and in Table 4 are not the differences to the "true" values but to the retrieval without bias or noise. The positive bias in the reflectances leads to a constant positive bias in the retrieval with maximum absolute differences of up to over 30 g/m^2 and an almost constant relative difference averaging at 7.0 %. Conversely, and notably different from the only-CLI retrieval, the negatively biased reflectances lead to a negatively biased retrieval with absolute differences reaching almost -20 g/m^2 and mostly constant relative differences with an average of -5.38 %. The overall time-series averages of the differences of biased to unbiased retrievals are presented in Table 4 for the usual sun-view geometry (middle sun) as well as for high and low sun. Varying the SuZA changes the influence of a bias in the reflectances considerably, as is clear from Table 4 and Figure 23. At high sun the differences introduced by the bias in the reflectances are much smaller than for middle sun, with time-series mean relative differences of only 0.65 % and 1.23 % for positively and negatively biased reflectances, respectively. For low sun on the other hand, the deviation from middle sun is much larger, with time-series mean differences of 21.12 % (positive bias) and -17.3 % (negative bias). These effects are explained by the different dependence of retrieved τ and r_e on the reflectances for different SuZAs which stems from the scattering phase function of liquid and ice particles varying with the scattering angle. This is demonstrated in Figure 6 in Mayer and Kylling (2005), where low sun roughly corresponds to 0.21 on the x-axis (the cosine of the scattering angle), middle sun to 0.55, and high sun to 0.84 (for constant SeZA = 30° and RAA = 100°). The figure shows that the phase function, and hence the reflectance, over this interval of scattering angles increases with the cosine of the scattering angle, explaining why high sun yields generally higher reflectances than middle sun, which yields higher reflectances than low sun. Comparing the LUTs for high and low sun with the middle sun LUT (see Figures $A.11$ and $A.12$ in the appendix) clearly elucidates the consequences of this, especially via the changed τ dependence on the 0.6 μm reflectance. For high sun the reflectances corresponding to the same τ value are considerably higher than for middle sun, while the low sun the reflectances are much lower. This means that the same

bias in the reflectances causes a much larger bias in the low sun retrieval than in the middle sun retrieval, and there a larger bias than in the high sun retrieval, which is what is evident in Figure 23. Accordingly, for high sun the decrease (increase) in τ brought on by the negative (positive) bias seems to be compensated by the increase (decrease) in r_e, which is not true for middle and low sun because there the reflectances mostly lie in an area of the LUT where the dependence of retrieved τ on the 0.6 μm reflectance is strongly exponential (cf. also Figure $A.3$ in the appendix).

The influence of noise is only minimal (see Table 4), even for low sun where it is larger than for the other two SuZAs but still causes only an error of about 1 %.

In conclusion regarding bias, noise, and varied SuZA, it can be said that in deep-convective ice-over-liquid cloud cases a typical instrument bias can lead to considerable deviation of the retrieval results, especially for a low sun geometry. Hence, a bias in the reflectances should not be neglected and best be corrected for before applying a Nakajima-King type retrieval. Conversely, a typical random measurement error (noise) does not seem to have considerable influence on the retrieval results, even at low sun.

Table 4: Time-series mean values of the absolute and relative differences of the retrieval from unbiased reflectances to the retrievals from reflectances with noise as well as positively and negatively biased reflectances for high (10°), middle (45°), and low (70°) sun. The values correspond Figure 23 as well as Figures $A.8$, $A.9$, and $A.10$ in the appendix.

diff. type/SuZA	10°	45°	70°
noise [abs.]	0.09 g/m^2	0.09 g/m^2	0.28 g/m^2
pos. bias [abs.]	2.12 g/m^2	16.08 g/m^2	46.68 g/m^2
neg. bias [abs.]	3.56 g/m^2	−10.35 g/m^2	−34.9 g/m^2
noise [rel.]	0.02 %	0.02 %	0.09 %
pos. bias [rel.]	0.65 %	7.0 %	21.12 %
neg. bias [rel.]	1.23 %	−5.38 %	−17.3 %

4.2.4 Varied Atmospheric Profiles

Investigating the domain-means of retrievals from configuration (C2) RTTOV input data suggests that the influence of varied atmospheric profile does have more considerable impact than might have been clear from the discussion in section 4.1.3. There the conclusion is that the influence of the (C2) configuration is more salient at higher reflectances, which, accordingly, makes them more interesting in ice-over-liquid cases, which are the focus here.

The (C2) retrieval results are smaller than the ones from (C3) input data with a relative time-series mean difference of −14.92 % and, as Figure 24 shows, they actually correspond better to "true" IWP than TWP, while (C3) retrieval results correspond better to "true" TWP (see Figure 20 and the corresponding discussion). In the time-series mean the retrieval

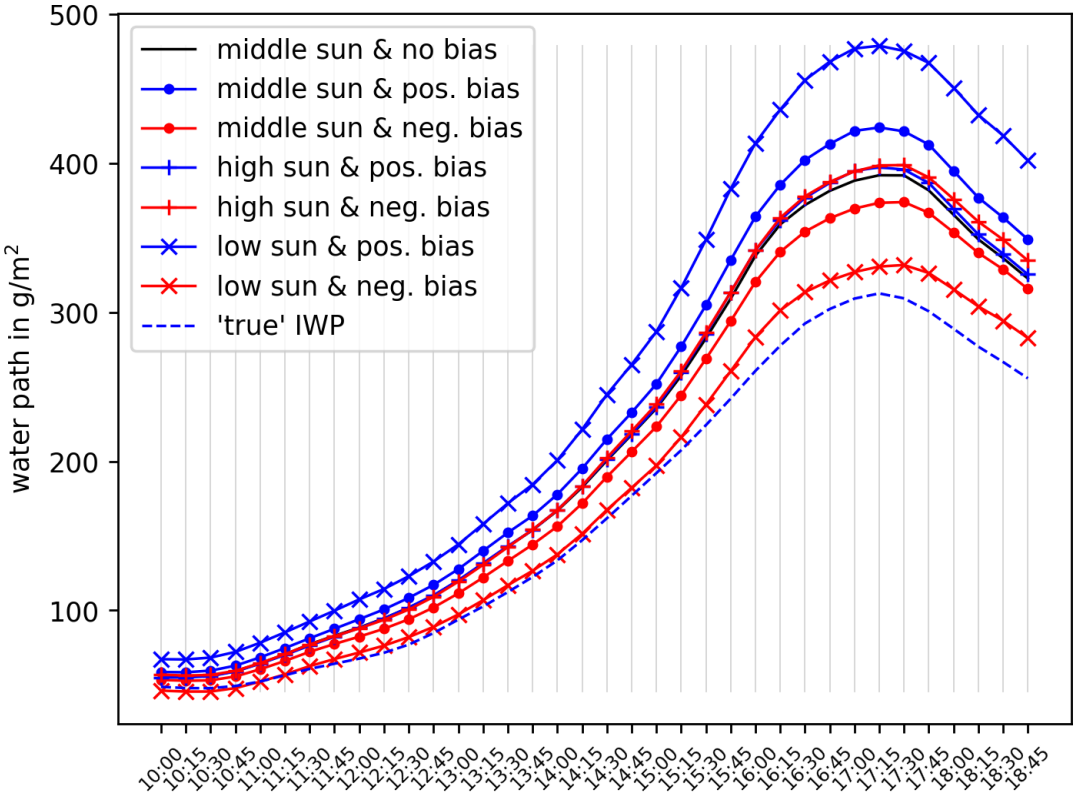

Figure 23: All-sky domain-mean time-series of middle sun unbiased retrieval (black line without markers), middle sun positively and negatively biased retrievals (blue and red line, respectively, with filled circle markers), high sun positively and negatively biased retrievals (blue and red line, respectively, with "×"-markers), and low sun positively and negatively biased retrievals (blue and red line, respectively, with "+"-markers). For orientation the "true" IWP is included (blue dashed line). All values correspond to configuration (C3) data with CLW+CLI. See Table 4 for statistics and Figures *A*.8, *A*.9, and *A*.10 in the appendix for the corresponding differences.

results for (C2) data only deviate by 6.96 % from "true" IWP, while the deviation is −27.06 % for "true" TWP.

In section 4.1.3 it is pointed out that finding out what exactly the reasons for the lower retrieval results from configuration (C2) data are is difficult. Some indications can be given here. More detailed investigation reveals that in all cases in the domain-mean the clouds in the (C2) data are slightly geometrically lower than in the (C3) data. Albeit, this is qualified by the fact that, again in the domain-mean, the clouds are situated at a lower pressure level, putting them actually higher in the atmosphere. Also, in the domain-mean, the air above the clouds is more humid in the (C3) data than in the (C2) data. However, as has been pointed out in section 4.1.3, the exponential relationship of τ to 0.6 μm reflectance limits the meaningfulness of examining mean values. E.g. looking at the average specific humidity in columns where CLI is at its 99th percentile or higher the air in the (C2) data is actually more humid than in the (C3) data (where it is the same in all columns). Maybe the largest part of the explanation for

the lower retrieval values for the (C2) configuration comes from the fact that the above-cloud O_3 concentration is slightly higher (about 1 to 2 %) than in the (C3) configuration. This holds true for the domain-mean as well as the mean in columns where CLI is at its 99th percentile or higher. Having higher O_3 values would increase the degree to which the radiation is absorbed (especially in the 0.6 μm channel), as is pointed out in section 4.1.3, which would translate to lower retrieved τ and finally lower retrieved WP.

Summing up the discussion about the influence of the varied atmospheric profile it can be concluded that it depends on the amount of CLW and CLI if the influence is important or not. For generally higher reflectance, which is a typical feature of deep-convective ice-over-liquid clouds, the impact of varied atmospheric profile, if it is not corrected for, can be quite severe. The reason is on the one hand the dependence of the reflectance on the O_3 and water vapour profiles and on the other hand the exponential relationship between 0.6 μm reflectance and retrieved τ. The 1.6 μm reflectances and retrieved r_e do not seem to have a noticeable impact.

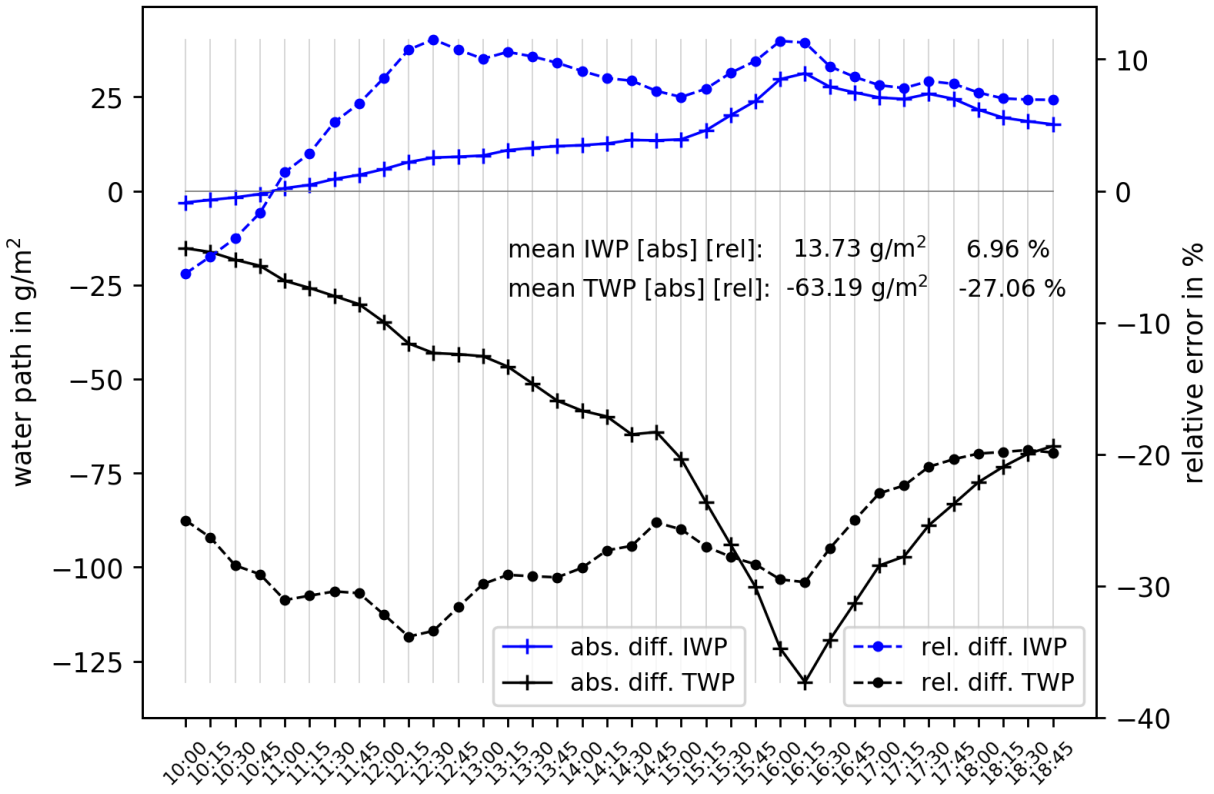

Figure 24: Time-series of all-sky domain-mean absolute (continuous with "+"-markers) and relative (dashed with filled circle markers) differences of CLW+CLI retrievals from configuration (C2) RTTOV input data to "true" IWP (blue) and TWP (black). For the (C3) case cf. Figure 20.

4.2.5 Full Clouds and Baran Scheme

In section 4.1.4 the Baran ice scheme is analysed for a single time-step on a pixel-to-pixel basis and it is found that the retrieval from Baran scheme reflectances, calculated from only-CLI

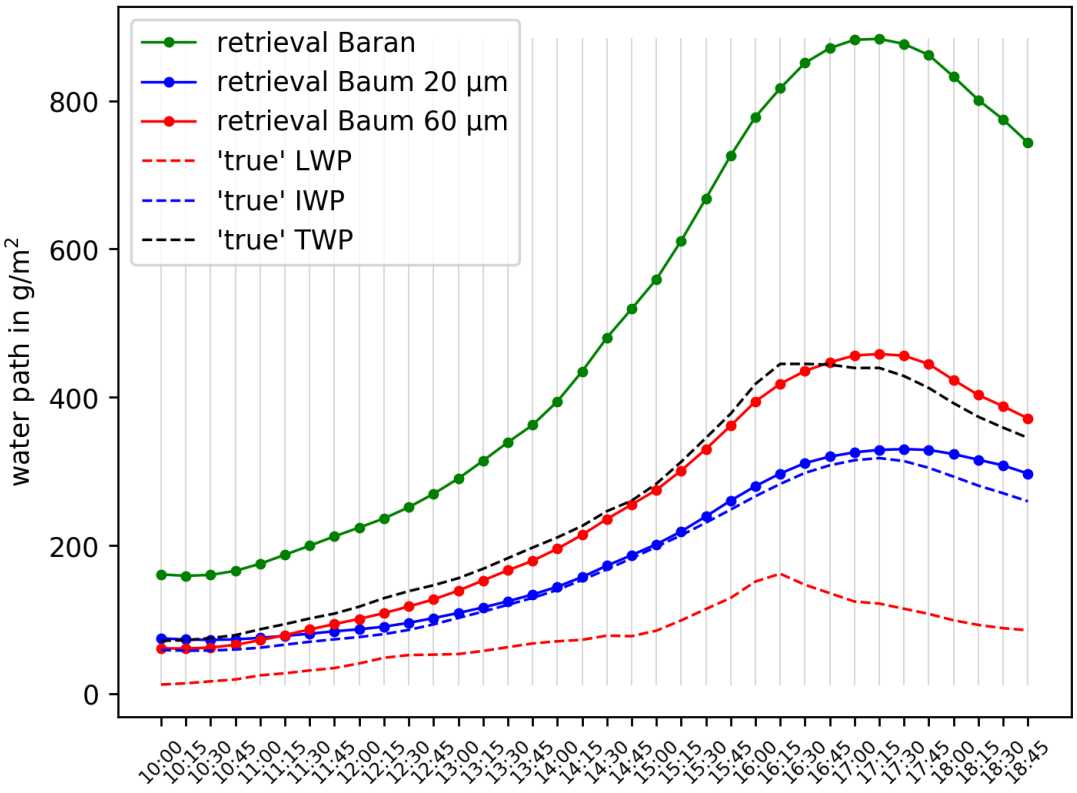

Figure 25: All-sky domain-mean time-series of CLW+CLI retrievals from Baran ice scheme reflectances (green line) as well as Baum scheme at *IceDe* = 20 μm (blue) and *IceDe* = 60 μm (red) reflectances. "True" TWP (black), IWP (blue), and LWP (red) are also shown for comparison.

RTTOV input, considerably overestimates the "true" IWP (see Figure 17). It is clearly evident from Figure 25 that this is true also for the retrievals based on the Baran scheme reflectances from CLW+CLI RTTOV input, with regards to both "true" IWP and TWP. Again note, that because of how the Baran scheme derives the cloud's optical properties (see section 3.2), it makes no sense to use it in configuration (C2) or (C3). Hence, the reflectances are calculated from a configuration (C1) RTTOV input. For comparison, RTTOV simulations from the same configuration (C1) input using the Baum scheme with *IceDe20* and *IceDe60* are conducted and the retrievals from the resulting reflectances are depicted in Figure 25, also. Similar to what has been established previously, the *IceDe20* retrieval corresponds quite closely to the "true" IWP, while the *IceDe60* retrieval resembles the "true" TWP much better, with relative time-series mean differences of 6.94 % and −1.7 %, respectively. The retrieval from the Baran scheme reflectances overestimates the "true" TWP by almost 100 % (97.97 %). The retrievals from the (C1) configuration data and Baum scheme reflectances exhibit not much larger relative differences from the "true" values than the retrievals from (C3) configuration data (cf. Table 3), which indicates that the influence of the cloud height on the retrieval described in section 4.1.4 is not very strong on the domain-mean scale. This is because the truncation at retrieved τ = 100 "absorbs" the large retrieved τ values and thus keeps the retrieved WP much lower than in a not truncated retrieval. Retrievals from the (C1) configuration RTTOV input *without*

truncation yield much larger values of WP. While the not truncated *IceDe60* retrieval still stays quite close to "true" TWP, now overestimating it in the mean by 10.88 %, the not truncated *IceDe20* retrieval now exceeds, in the time-series mean, IWP by 92.18 % and TWP by 29.14 %. Note that the impact of not truncating the retrieved τ at 100 on retrievals from the configuration (C3) RTTOV input is comparatively small. Treating the *IceDe60* retrieval as TWP amounts to a -13.74 % time-series mean underestimation of the "truth" (compared to -14.26 % for the not truncated retrieval; see Table 3) and treating the *IceDe20* retrieval as IWP amounts to a 6.95 % time-series mean overestimation of the "truth" (compared to -4.55 % for the not truncated retrieval; see Table 3). This goes to show that the truncation does not have a large effect in the (C3) configuration (although it is much larger in the *IceDe20* case than in the *IceDe60* case) but it does have a substantial effect in the (C1) configuration, which indicates that cloud (top) height has considerable impact on the reflectances and hence the retrieval (cf. also Figure *A*.4 in the appendix).

From the preceding discussion it is clear that the choice of cloud ice scheme in RTTOV has non-negligible influence on the retrieval quality. The Baum scheme is chosen in the present study because it works with the applied idealisations, which is not true for the Baran scheme. For the same RTTOV input data configuration both schemes yield very different results, even when the Baum scheme is used with multiple different *IceDes*. Furthermore, the influence of the $\tau \leq 100$ truncation is substantial, especially for *IceDe20*. Albeit, in the cases investigated here it seems to actually improve the retrieval quality and cancels out the overestimation due to larger cloud height in the (C1) configuration.

5 Summary and Conclusions

The aim of this study was to investigate Nakajima-King bi-spectral retrievals and their performance in deep-convective ice-over-liquid clouds. To do this a model-only approach is followed, exploiting the capabilities of recently developed high-resolution convection resolving NWP models simulating the cloud field and using RTMs to generate synthetic reflectances. These can subsequently be used to perform the retrieval and the retrieval results can be compared to the "truth" from the NWP model cloud field.

It is found that, while considering only CLI in the most idealised case resembling the sanity-check configuration yields a near-perfect retrieval (compared to "true" IWP), using the same configuration but with both CLW and CLI retained, the retrieval corresponds similarly, albeit weaker, to both "true" IWP as well as "true" TWP. However, a further finding is, that it is important which *IceDe* is assumed in the radiative transfer calculations. Assuming smaller *IceDe* (e.g. 20 μm) leads to better correspondence with "true" IWP while assuming larger *IceDe* (e.g. 100 μm) results in better correspondence with "true" TWP. There is a caveat to this, however, which is the influence of the retrieval truncation at $\tau = 100$. Not truncating the retrieval in the case of small *IceDe* causes much larger retrieved values leading to large overestimations of both "true" IWP and "true" TWP. These overestimations are thus cancelled out by the truncation. Conversely, the truncation has only a weak effect in cases with larger assumed *IceDe*.

The influence of random measurement error (noise) and sensor bias depends on the intensity of the reflectance as well as on the SuZA. For lower reflectances in a middle sun configuration only a positive bias has some impact. For higher reflectances (which are more typical in deep-convective clouds) both positive and negative bias have non-negligible influence on the retrieval result but noise does not seem important. In a high sun configuration neither noise nor positive nor negative bias have large influence but for low sun both positive and negative bias change the retrieval results substantially (more than in all the aforementioned cases). Still, noise does not seem to have an impact, even in the low sun case.

Using different configurations of input data for the RTM also changes the retrieval results. As stated above, the retrievals from the most idealised input data (C3) are near-perfect. In the less idealised configuration (condensed clouds but varied atmospheric profile, (C2)) the retrievals underestimate the "true" values. The degree of the underestimation again depends on the intensity of the refectances. Generally higher reflectances lead to greater underestimation, while generally lower reflectances result in less underestimation. Retrievals from the original NWP output configuration (C1) exhibit slight overestimation of the "truth". Here, again, the influence of the $\tau \leq 100$ truncation is substantial and prevents larger overestimation, especially in the case of smaller assumed *IceDe*.

Finally, changing the ice cloud scheme in the RTTOV calculations from Baum to Baran leads to strong differences in the retrieval results. The retrieved r_e varies much more strongly than in the previous cases and the retrieved WP values overestimate the "truth" more severely

than in previous cases.

Several (tentative) conclusions might be drawn from these results.

First, the results generally reinforce the findings of previous studies (see section 1) that Nakajima-King bi-spectral retrievals for deep-convective ice-over-liquid clouds are ambiguous. While for single-phase clouds, provided τ is not extremely small or large, the retrieval is very precise, errors can get substantial in mixed-phase clouds.

A second conclusion, connected to the first, is that the quality as well as the quantity of the errors in the retrieval results compared to the (model) "truth" depend strongly on the assumptions made in the RTM simulations. Assuming different values of *IceDe* in the Baum ice scheme changes if the retrieval corresponds better to "true" IWP or TWP. Using a different radiation scheme for the CLI (Baran instead of Baum) leads to much higher retrieved WP, not corresponding well to either of the "true" quantities. However, the applicability of the Baran scheme is limited for the approach followed here, since the LUTs are generated using the Baum scheme. Furthermore, there is complex interplay between the assumptions in the radiation schemes and the $\tau \leq 100$ truncation in the retrieval algorithm, with the latter introducing a negative bias compared to what would actually follow from the reflectances. Hence, it is questionable if the strong correspondence of results from the *IceDe20* configuration with "true" IWP is physical or simply a lucky coincidence. The correspondence might change, if the τ threshold for the truncation is changed in the retrieval algorithm, which is sometimes done (e.g. for MODIS retrievals from 100 to 150, see King et al., 1997, and Platnick et al., 2017), and hence change the retrieved values and the way they should best be interpreted. The retrievals from reflectances from larger assumed *IceDe* do not seem to be as strongly affected by the truncation, however.

This leads to a third conclusion, namely that the current knowledge about CLI and it's radiative properties puts limits on the applicability of the model-only approach followed in the present study. This is similar to the conclusions of several previous studies mentioned in section 1 (Waliser et al., 2009; Eliasson et al., 2011; Duncan and Eriksson, 2018). More clarity regarding the applicability of different radiation schemes is needed to achieve more rigorous results from the model-only methodology. The large differences between the Baran and Baum scheme radiative transfer calculations elucidate that assuming a different ice model in the LUT than that actually existing in the cloud can lead to large errors in the retrieval.

Putting aside these caveats, a fourth, tentative, conclusion would be that the retrieved r_e could be used to decide if the retrieval should be considered to correspond to "true" IWP or TWP. For larger retrieved r_e (around 50 μm) the retrieved WP can be considered as TWP and for smaller retrieved r_e (around 10 μm) it can be considered as IWP. For both the relative error is between $\pm$ 10 % in all considered cases. Notably, the sign of the error is not unambiguous. In the case of a medium r_e (like 30 μm) the errors are larger (20 to 30 %). Although this has not been tested explicitly, there seems to be a continuum with retrievals first corresponding better to IWP (small ice particle sizes), then there is more ambiguity (medium ice particle sizes),

and finally there is a shift to better correspondence to TWP (large ice particle sizes). Finding an exact value of ice particle size where this transition (from IWP to TWP) is feasible might not be possible if the relationship really is continuous. Moreover, it seems difficult to draw general quantitative conclusions from this because, as discussed in section 4.2.2, it depends on the specific ice-over-liquid configuration if the quantity in question (IWP or TWP) is over- or underestimated.

As a fifth conclusion it can be said that regarding random measurement error (noise), bias, and sun-view geometry their isolated effects, though not negligible (especially in the case of positive bias and generally larger reflectances), are limited, but their combined effect (especially regarding low sun and bias) are substantial. If the bias is similar to that found for SEVIRI by Govaerts and Clerici (2004) it should hence be corrected for to prevent considerable over- or underestimations in the retrieval. Noise at the level found in the same study on the other hand does not seem to be as important and might be neglected.

Ideas for further research could be to compare the RTTOV calculations in the here considered cases with calculations from other stand-alone RTMs to investigate the applicability of the different cloud schemes. Using RTTOV with the output data from NWP models is very convenient because only little preprocessing of the output data is necessary but the problem is that different effects like the absorption due to different trace gasses or Rayleigh scattering cannot be turned off in RTTOV and hence their impact cannot be precisely isolated. This might be achieved by applying different RTMs to the same general methodology.

For further studies using RTTOV or similar 1-dimensional RTMs the accuracy of their calculation could be increased by e.g. transforming the RTM input data to correspond to the tilted independent pixel approximation which would more closely resemble the path of solar radiation through the atmosphere (Frame et al., 2009). There are also methods to approximate 3-dimensional cloud effects such as cloud top inclination which might increase the accuracy of the 1-dimensional radiative transfer calculations (Scheck et al., 2018).

Another idea would be to make further tests of the dependence of the retrieval correspondence to "true" IWP and TWP on the particle size. In the present study only three different *IceDes* over a period of only one day are considered but in further research more different *IceDes* and more simulated cloud fields could be investigated. A tentative empirical relationship might be established regarding on the one hand when it is feasible to consider the retrieved WP as IWP and when as TWP and on the other hand giving an assessment of the over- or underestimation based on the retrieved r_e. Note that empirical relationships have been proposed before based on observational data for similar retrievals (Smith, 2014, section 5.2; Tian et al., 2018). There, however, the influence of retrieved r_e on whether the retrieval should be interpreted as IWP or TWP is not considered. Some caveats to a possible empirical relationship have been discussed above. One further caveat to be investigated in this regard would be the effectiveness of atmospheric correction within the retrieval algorithm. As stated above, the retrievals depend substantially on the the idealisation of the input data ((C1), (C2), (C3)), emphasising

the influence of atmospheric profile (water vapour, O_3, etc.) and cloud height. If these cannot be corrected for, it would not make sense to use the above hypothesised empirical relationship since the errors due to varying atmospheric profile and cloud height would not be compensated.

Finally, real Nakajima-King retrieval data could be investigated and compared to data from other retrieval methods to investigate if an empirical relationship depending on the retrieved effective particle size is viable.

References

Alexandri, G., A. K. Georgoulias, P. Zanis, E. Katragkou, A. Tsikerdekis, K. Kourtidis, and C. Meleti (2015). "On the ability of RegCM4 regional climate model to simulate surface solar radiation patterns over Europe: An assessment using satellite-based observations." In: *Atmospheric Chemistry and Physics* 15, pp. 13195–13216. DOI: 10.5194/acp-15-13195-2015.

Anderson, G. P., S. A. Clough, F. X. Kneizys, J. H. Cheywynd, and E. P. Shettle (May 1986). *AFGL atmospheric constituent profiles (0 – 120 km).* Environmental Research Papers 954. Air Force Geophysics Laboratory.

Baldauf, M., A. Seifert, J. Förstner, D. Majewski, M. Raschendorfer, and T. Reinhardt (2011). "Operational convective-scale numerical weather prediction with the COSMO model: Description and sensitivities." In: *Monthly Weather Review* 139, pp. 3887–3905. DOI: 10.1175/MWR-D-10-05013.1.

Baran, A. J., R. Cotton, K. Furtado, S. Havemann, L.-C. Labonnote, F. Marenco, A. Smith, and J.-C. Thelen (2014). "A self-consistent scattering model for cirrus. II: The high and low frequencies." In: *Quarterly Journal of the Royal Meteorological Society* 140, pp. 1039–1057. DOI: 10.1002/qj.2193.

Baum, B. A., P. Yang, A. J. Heymsfield, C. Schmitt, Y. Xie, A. Bansemer, Y. X. Hu, and Z. Zhang (2011). "Improvements to shortwave bulk scattering and absorption models for the remote sensing of ice clouds." In: *Journal of Applied Meteorology and Climatology* 50, pp. 1037–1056. DOI: 10.1175/2010JAMC2608.1.

Benas, N., S. Finkensieper, M. Stengel, G.-J. van Zadelhoff, T. Hanschmann, R. Hollmann, and J. F. Meirink (2017). "The MSG-SEVIRI-based cloud property data record CLAAS-2." In: *Earth System Science Data* 9, pp. 415–434. DOI: 10.5194/essd-9-415-2017.

Blahak, U. (2008). "Towards a better representation of high density ice particles in a state-of-the-art two-moment bulk microphysical scheme." In: *Proceedings of the 15th International Conference Clouds and Precipitation.* Cancun, Mexico.

Brisson, E., K. Van Weverberg, M. Demuzere, A. Devis, S. Saeed, M. Stengel, and N. P. M. van Lipzig (2016). "How well can a convection-permitting climate model reproduce decadal statistics of precipitation, temperature and cloud characteristics?" In: *Climate Dynamics* 47, pp. 3043–3061. DOI: 10.1007/S00382-016-3012-Z.

Bugliaro, L., T. Zinner, C. Keil, B. Mayer, R. Hollmann, M. Reuter, and W. Thomas (2011). "Validation of cloud property retrievals with simulated satellite radiances: A case study for SEVIRI." In: *Atmospheric Chemistry and Physics* 11, pp. 5603–5624. DOI: 10.5194/acp-11-5603-2011.

Chandrasekar, S. (1960). *Radiative Transfer.* New York: Dover.

Dipankar, A., B. Stevens, R. Heinze, C. Moseley, G. Zängl, M. Giorgetta, and S. Brdar (2015). "Large eddy simulation using the general circulation model ICON." In: *Journal of Advances in Modeling Earth Systems* 7, pp. 963–986. DOI: 10.1002/2015MS000431.

Duncan, D. I. and P. Eriksson (2018). "An update on global atmospheric ice estimates from satellite observations and reanalyses." In: *Atmospheric Chemistry and Physics* 18, pp. 11205–11219. DOI: 10.5194/acp-18-11205-2018.

Eliasson, S., S. A. Buehler, M. Milz, P. Eriksson, and V. O. John (2011). "Assessing observed and modelled spatial distributions of ice water path using satellite data." In: *Atmospheric Chemistry and Physics* 11, pp. 375–391. DOI: 10.5194/acp-11-375-2011.

Eyre, J. R. (Mar. 1991). *A fast radiative transfer model for satellite sounding systems.* Technical Memorandum 176. ECMWF.

Finkensieper, S., J. F. Meirink, G.-J. van Zadelhoff, T. Hanschmann, N. Benas, M. Stengel, P. Fuchs, R. Hollmann, and M. Werscheck (2016). *CLAAS-2: CM SAF CLoud property dAtAset using SEVIRI – Edition 2.* EUMETSAT CM SAF. DOI: 10.5676/EUM_SAF_CM/CLAAS/V002.

Frame, J. W., J. L. Petters, P. M. Markowski, and J. Y. Harrington (2009). "An application of the tilted independent pixel approximation to cumulonimbus environments." In: *Atmospheric Research* 91, pp. 127–136. DOI: 10.1016/j.atmosres.2008.05.005.

Geer, A. J., K. Lonitz, P. Weston, M. Kazumori, K. Okamoto, Y. Zhu, E. H. Liu, A. Collard, W. Bell, S. Migliorini, P. Chambon, N. Fourriè, M.-J. Kim, C. Köpken-Watts, and C. Schraff (2018). "All-sky satellite data assimilation at operational weather forecasting centres." In: *Quarterly Journal of the Royal Meteorological Society* 144, pp. 1191–1217. DOI: 10.1002/qj.3202.

Govaerts, Y. and M. Clerici (Jan. 2004). *MSG-1/SEVIRI Solar Channels Calibration.* Commissioning Activity Report. EUMETSAT.

Grassmann, A. and H.-J. Herzog (2008). "Towards a consistent numerical compressible nonhydrostatic model using generalized Hamiltonian tools." In: *Quarterly Journal of the Royal Meteorological Society* 134, pp. 1597–1613. DOI: 10.1002/qj.297.

Hansen, J. E. and L. D. Travis (1974). "Light scattering in planetary atmospheres." In: *Space Science Reviews* 16, pp. 527–610. DOI: 10.1007/BF00168069.

Heidinger, A. K., M. J. Foster, A. Walther, and X. Zhao (2014). "The Pathfinder Atmospheres-Extended AVHRR Climate Data Set." In: *Bulletin of the American Meteorological Society* 95, pp. 909–922. DOI: 10.1175/BAMS-D-12-00246.1.

Heinze, R., A. Dipankar, C. C. Henken, C. Moseley, O. Sourdeval, S. Trömel, X. Xie, P. Adamidis, F. Ament, H. Baars, C. Barthlott, A. Behrendt, U. Blahak, S. Bley, S. Brdar, M. Brueck, S. Crewell, H. Deneke, P. Di Girolamo, R. Evaristo, J. Fischer, C. Frank, P. Friederichs, T. Göcke, K. Gorges, L. Hande, M. Hanke, A. Hansen, H.-C. Hege, C. Hoose, T. Jahns, N. Kalthoff, D. Klocke, S. Kneifel, P. Knippertz, A. Kuhn, T. van Laar, A. Macke, V. Maurer, B. Mayer, C. I. Meyer, S. K. Muppa, R. A. J. Neggers, E. Orlandi, F. Pantillon, B. Pospichal, N. Röber, L. Scheck, A. Seifert, P. Seifert, F. Senf, P. Siligam, C. Simmer, S. Steinke, B. Stevens, K. Wapler, M. Weniger, V. Wulfmeyer, G. Zängl, D. Zhang, and J. Quaase (2017). "Large-eddy simulations over Germany using ICON: A comprehensive evaluation." In: *Quarterly Journal of the Royal Meteorological Society* 143, pp. 69–100. DOI: 10.1002/qj.2947.

Hess, M., P. Koepke, and I. Schult (1998). "Optical Properties of Aerosols and Clouds: The Software Package OPAC." In: *Bulletin of the American Meteorological Society* 79, pp. 831–844. DOI: 10.1175/1520-0477(1998)079<0831:OPOAAC>2.0.CO;2.

Heymsfield, A. J. and M. Kajikawa (1987). "An improved approach to calculating terminal velocities of plate-like crystals and graupel." In: *Journal of the Atmospheric Sciences* 44, pp. 1088–1099. DOI: 10.1175/1520-0469(1987)044<1088:AIATCT>2.0.CO;2.

Hocking, J. (Dec. 2016). *A visible/infrared multiple-scattering model for RTTOV.* Technical Report. EUMETSAT NWP SAF. URL: http://nwpsaf.eu/publications/tech_reports/nwpsaf-mo-tr-031.pdf (visited on 07/02/2018).

Hocking, J., P. Rayer, D. Rundle, R. W. Saunders, M. Matricardi, A. Geer, P. Brunel, and J. Vidot (Apr. 2018a). *RTTOV v12 Users Guide.* Version 1.2. EUMETSAT NWP SAF. URL: https://www.nwpsaf.eu/site/download/documentation/rtm/docs_rttov12/users_guide_rttov12_v1.2.pdf (visited on 07/02/2018).

Hocking, J., P. Roquet, and P. Brunel (Mar. 2018b). *Python/C/C++ wrapper for RTTOV v12.* Version 1.2. EUMETSAT NWP SAF. URL: https://www.nwpsaf.eu/site/download/documentation/rtm/docs_rttov12/rttov-wrapper.pdf (visited on 07/02/2018).

Horváth, Á. and R. Davies (2007). "Comparison of microwave and optical cloud water path estimates from TMI, MODIS, and MISR." In: *Journal of Geophysical Research: Atmospheres* 112.DO1202. DOI: 10.1029/2006JD007101.

Huang, J., P. Minnis, B. Lin, Y. Yi, T. F. Fan, S. Sun-Mack, and J. K. Ayers (2006). "Determination of ice water path in ice-over-water cloud systems using combined MODIS and AMSR-E measurements." In: *Geophysical Research Letters* 33.L21801. DOI: 10.1029/2006GL027038.

Keller, M., O. Fuhrer, J. Schmidli, M. Stengel, R. Stöckli, and C. Schär (2015). "Evaluation of convecion-resolving model using satellite data: The diurnal cycle of summer convection over the Alps." In: *Meteorologische Zeitschrift* 25, pp. 165–179. DOI: 10.1127/metz/2015/0715.

King, M. D., S.-C. Tsay, S. E. Platnick, M. Wang, and K.-N. Liou (Dec. 1997). *Cloud retrieval algorithms for MODIS: Optical thickness, effective particle radius, and thermodynamic phase.* Algorithm Theoretical Basis Document ATBD-MOD-05. NASA Goddard Space Flight Center. URL: https://modis.gsfc.nasa.gov/data/atbd/atbd_mod05.pdf (visited on 09/03/2019).

Mayer, B. and A. Kylling (2005). "Technical note: The libRadtran software package for radiative transfer calculations - description and examples of use." In: *Atmospheric Chemistry and Physics* 5, pp. 1855–1877. DOI: 10.5194/acp-5-1855-2005.

Meirink, J. F., R. A. Roebeling, and P. Stammes (Feb. 2009). *Atmospheric correction for the KNMI Cloud Physical Properties retrieval algorithm.* Technical Report 304. KNMI. URL: https://cdn.knmi.nl/system/data_center_publications/files/000/068/281/original/tr304_atmospheric_correction_meirink.totaal_copy1.pdf?1495621108 (visited on 07/30/2019).

Meirink, J. F. and G.-J. van Zadelhoff (June 2016). *SEVIRI Cloud Physical Products, CLAAS Edition 2.* Algorithm Theoretical Basis Document. EUMETSAT CM SAF. DOI: 10.5676/EUM_SAF_CM/CLAAS/V002.

Minnis, P., J. Huang, B. Lin, Y. Yi, R. F. I. Arduin, T.-F. Fan, J. K. Ayers, and G. G. Mace (2007). "Ice cloud properties in ice-over-water cloud systems using Tropical Rainfall Measuring Mission (TRMM) visible and infrared scanner and TRMM Microwave Imager data." In: *Geophysical Research Letters* 112.D06206. DOI: 10.1029/2006JD007626.

Nakajima, T. and M. D. King (1990). "Determination of the Optical Thickness and Effective Particle Radius of Clouds from Reflected Solar Radiation Measurements. Part I: Theory." In: *Journal of the Atmospheric Sciences* 47, pp. 1878–1893. DOI: 10.1175/1520-0469(1990)047<1878:DOTOTA>2.0.CO;2.

Noppel, H., U. Blahak, A. Seifert, and K. D. Beheng (2010). "Simulations of a hailstorm and the impact of CCN using an advanced two-moment cloud microphysical scheme." In: *Atmospheric Research* 96, pp. 286–301. DOI: 10.1016/j.atmosres.2009.09.008.

Petty, G. W. (2006). *A First Course in Atmospheric Radiation.* Madison, Wisconsin: Sundog Publishing.

Platnick, S., K. G. Meyer, M. D. King, G. Wind, N. Amarasinghe, B. Marchant, G. T. Arnold, Z. Zhang, P. A. Hubanks, R. E. Holz, P. Yang, W. L. Ridgway, and B. Riedi (2017). "The MODIS cloud optical and microphysical products: Collection 6 updates and examples from Terra and Aqua". In: *IEEE Transactions on Geoscience and Remote Sensing* 55. DOI: 10.1109/TGRS.2016.2610522.

Roebeling, R. A., A. J. Feijt, and P. Stammes (2006). "Cloud property retrievals for climate monitoring: Implications of differences between Spinning Enhanced Visible and Infrared Imager (SEVIRI) on METEOSAT-8 and Advanced Very High Resolution Radiometer (AVHRR) on NOAA-17." In: *Journal of Geophysical Research* 111.D20210. DOI: 10.1029/2005JD006990.

Roebeling, R. A. and I. Hollman (2009). "SEVIRI rainfall retrieval and validation using weather radar observations." In: *Journal of Geophysical Research* 114.D21202. DOI: 10.1029/2009JD012102.

Rossow, W. B. and R. A. Schiffer (1991). "ISCCP cloud data products." In: *Bulletin of the American Meteorological Society* 71, pp. 2–20. DOI: 10.1175/1520-0477(1991)072<0002:ICDP>2.0.CO;2.

— (1999). "Advances in understanding clouds from ISCCP." In: *Bulletin of the American Meteorological Society* 80, pp. 2261–2288. DOI: 10.1175/1520-0477(1999)080<2261:AIUCFI>2.0.CO;2.

Saunders, R. W., J. Hocking, D. Rundle, P. Rayer, S. Havemann, M. Matricardi, A. Geer, C. Lupu, P. Brunel, and J. Vidot (Feb. 2017). *RTTOV v12 science and validation report.* Validation Report. EUMETSAT NWP SAF. URL: https://www.nwpsaf.eu/site/download/documentation/rtm/docs_rttov12/rttov12_svr.pdf (visited on 07/02/2018).

Saunders, R. W., J. Hocking, E. Turner, P. Rayer, D. Rundle, P. Brunel, J. Vidot, P. Roquet, M. Matricardi, A. Geer, N. Bormann, and C. Lupu (2018). "An update on the RTTOV fast radiative transfer model (currently at version 12)." In: *Geoscientific Model Development* 11, pp. 2717–2737. DOI: 10.5194/gmd-11-2717-2018.

Saunders, R. W., M. Matricardi, and P. Brunel (1999). "An improved fast radiative transfer model for assimilation of satellite radiance observations." In: *Quarterly Journal of the Royal Meteorological Society* 125, pp. 1407–1425. DOI: 10.1002/qj.49712555615.

Scheck, L., M. Weissmann, and B. Mayer (2018). "Efficient methods to account for cloud-top inclination and cloud overlap in synthetic visible satellite images." In: *Journal of Atmospheric and Oceanic Technology* 35, pp. 665–685. DOI: 10.1175/JTECH-D-17-0057.1.

Schmetz, J., P. Pili, S. Tjemkes, D. Just, J. Kerkmann, S. Rota, and A. Ratier (2002). "An introduction to Meteosat Second Generation (MSG)." In: *Bulletin of the American Meteorological Society* 83, pp. 977–992. DOI: 10.1175/1520-0477(2002)083<0977:AITMSG>2.3.CO;2.

Seifert, A. and K. D. Beheng (2001). "A double-moment parameterization for simulating autoconversion, accretion and selfcollection." In: *Atmospheric Research* 59-60, pp. 265–281. DOI: 10.1016/S0169-8095(01)00126-0.

— (2006). "A two-moment cloud microphysics parameterization for mixed-phase clouds. Part I: Model description." In: *Meteorology and Atmospheric Physics* 92, pp. 45–66. DOI: 10.1007/s00703-005-0112-4.

Smith, W. L. Jr. (July 2014). "4-D cloud properties from passive satellite data and applications to resolve the flight icing threat to aircraft." PhD Dissertation. University of Wisconsin-Madison.

Stamnes, K., S.-C. Tsay, W. Wiscombe, and K. Jayaweera (1988). "Numerically stable algorithm for discrete ordinate-method radiative transfer in multiple-scattering and emitting layered media." In: *Applied Optics* 27, pp. 2502–2509. DOI: 10.1364/AO.27.002502.

Stephens, G. L. (1978). "Radiation profiles in extended water clouds. II: Parameterization schemes." In: *Journal of the Atmospheric Sciences* 35, pp. 2123–2132. DOI: 10.1175/1520-0469(1978)035<2123:RPIEWC>2.0.CO;2.

Stocker, T. F., D. Qin, G.-K. Plattner, M. Tignor, S. K. Allen, J. Boschung, A. Nauels, Y. Xia, V. Bex, and P. Midgley, eds. (2013). *Climate Change 2013: The physical science basis. Contribution of Working Group I to the Fifth Assessment Report of the Intergovernmental Panel on Climate Change.* Cambridge, United Kingdom and New York, NY, USA: Cambridge University Press.

Tian, J., X. Dong, B. Xi, P. Minnis, W. L. Smith Jr., S. Sun-Mack, and J. Wang (2018). "Comparisons of ice water path in deep convective systems among ground-based, GOES, and CERES-MODIS retrievals." In: *Journal of Geophysical Research: Atmospheres* 123, pp. 1708–1723. DOI: 10.1002/2017JD027498.

Vidot, J., A. J. Baran, and P. Brunel (2015). "A new ice cloud parameterization for infrared radiative transfer simulation of cloudy radiances: Evaluation and optimization with IIR

observations and ice cloud profile retrieval products". In: *Journal of Geophysical Research: Atmospheres* 120, pp. 6937–6951. DOI: 10.1002/2015JD023462.

Waliser, D. E., J.-L. F. Li, C. P. Woods, R. T. Austin, J. Bacmeister, J. Chern, A. Del Genio, J. H. Jiang, Z. Kuang, H. Meng, P. Minnis, S. Platnick, W. B. Rossow, G. L. Stephens, S. Sun-Mack, W.-K. Tao, A. M. Tompkins, D. G. Vane, C. Walker, and D. Wu (2009). "Cloud ice: A climate model challenge with signs and expectations of progress." In: *Journal of Geophysical Research: Atmospheres* 114.D00A21. DOI: 10.1029/2008JD010015.

Wang, K., K. Yahya, Y. Zhang, C. Hogrefe, G. Pouliot, C. Knote, A. Hodzic, R. San Jose, J. L. Perez, P. Jimènez-Guerrero, R. Baro, P. Makar, and R. Bennartz (2015). "A multi-model assessment for the 2006 and 2010 simulations under the Air Quality Model Evaluation International Initiative (AQMEII) Phase 2 over North America: Part II. Evaluation of column variable predictions using satellite data." In: *Atmospheric Environment* 115, pp. 587–603. DOI: 10.1016/j.atmosenv.2014.07.044.

Yang, P., L. Bei, B. A. Baum, K.-N. Liou, G. W. Kattawar, M. I. Mishchenko, and B. Cole (2013). "Spectrally consistent scattering, absorption, and polarization properties of atmospheric ice crystals at wavelengths from 0.2 to 100 μm." In: *Journal of the Atmospheric Sciences* 70, pp. 330–347. DOI: 10.1175/JAS-D-12-039.1.

Zängl, G., D. Reinert, P. Ripodas, and M. Baldauf (2015). "The ICON (ICOsahedral Non-hydrostatic) modelling framework of DWD and MPI-M: Description of the non-hydrostatic dynamical core." In: *Quarterly Journal of the Royal Meteorological Society* 141, pp. 563–579. DOI: 10.1002/qj.2378.

Appendix

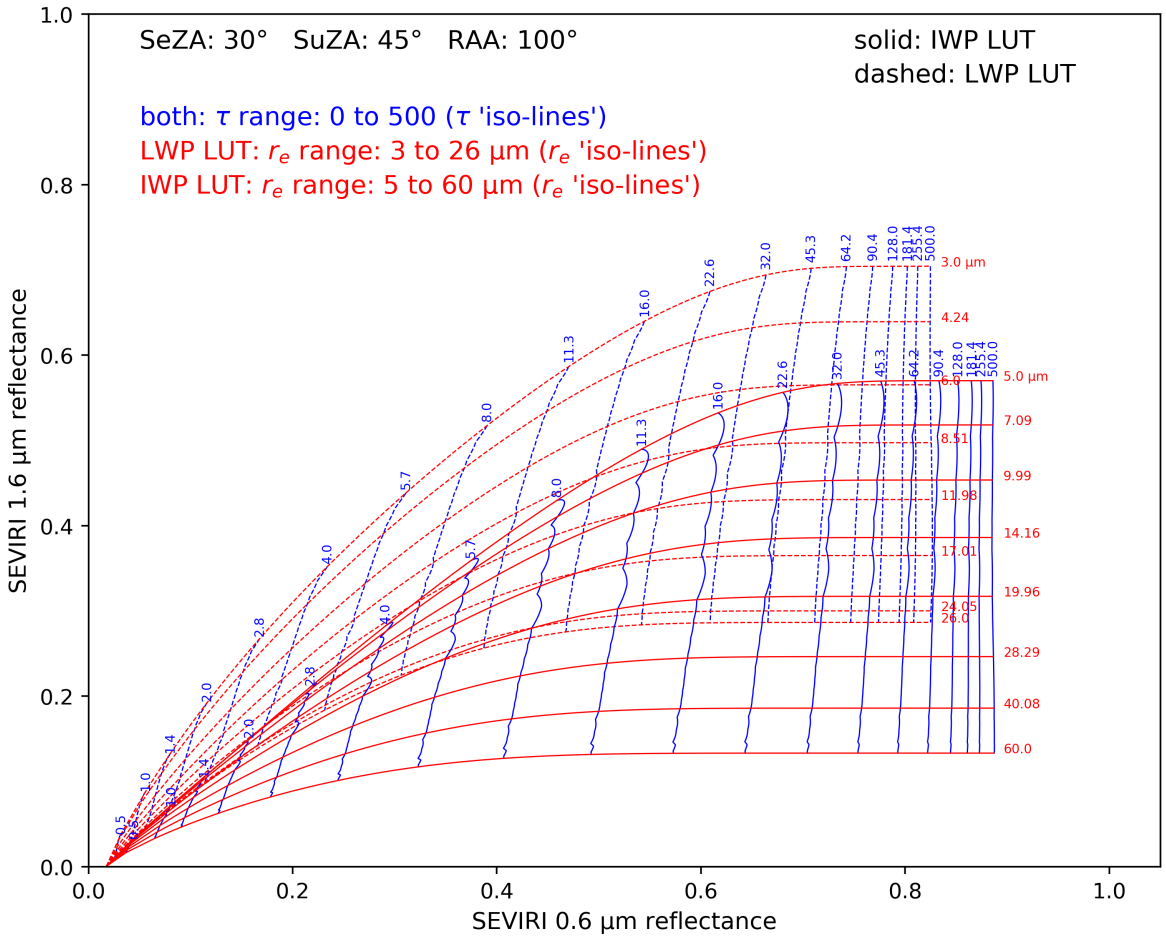

Figure A.1: Comparison of the corresponding LUTs for liquid (dashed) and ice (continuous). Refer to section 2.2 and Table 1 for details.

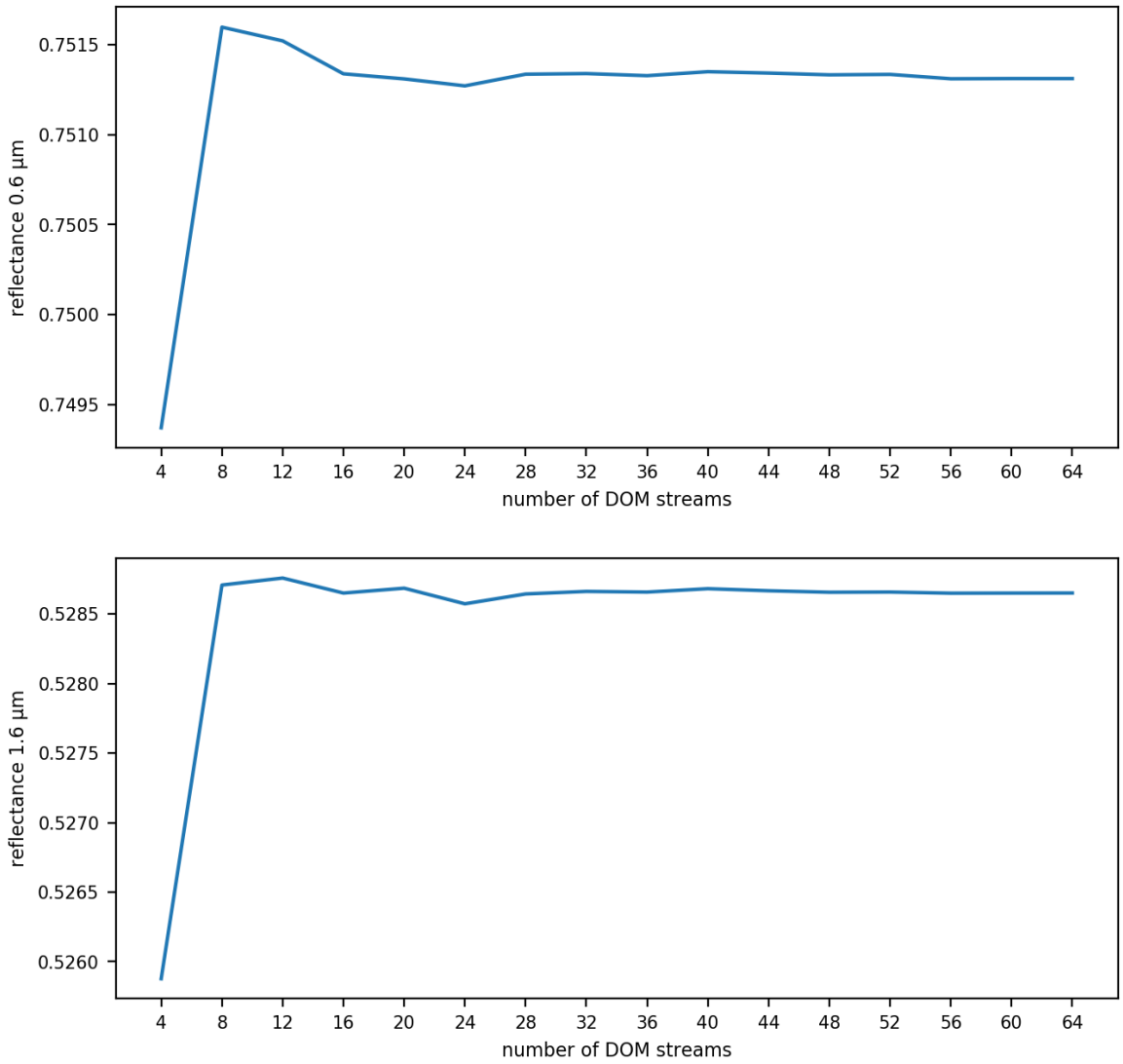

Figure A.2: Typical example of the dependence of the SEVIRI 0.6 μm (top) and 1.6 μm (bottom) reflectance on the number of DOM streams. See section 3.3.

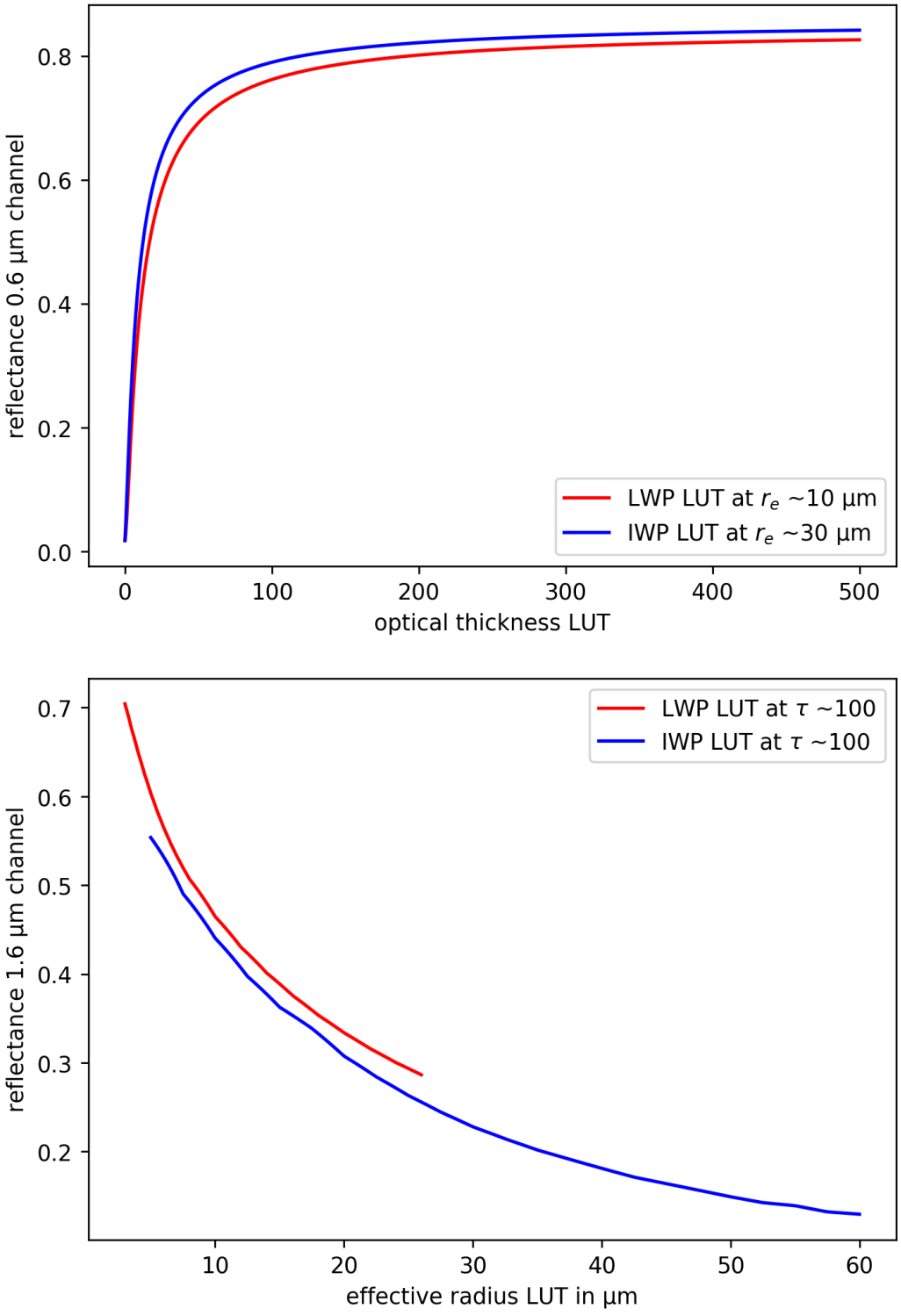

Figure A.3: Relationship of τ and 0.6 μm reflectance (top) as well r_e and 1.6 μm reflectance (bottom). Cf. the corresponding LUTs in Figure $A.1$.

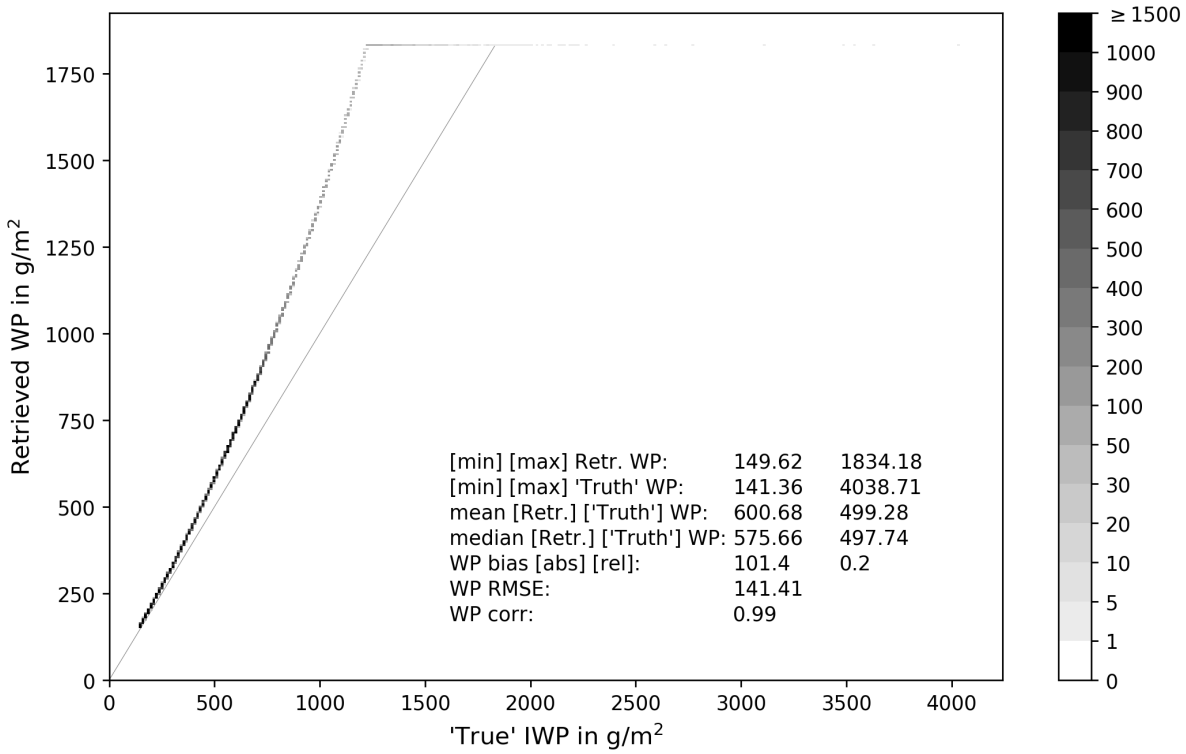

Figure A.4: 2d-histogram of only-CLI configuration (C3) retrieval v. "true" IWP. This is the same configuration as in Figure 9 but with CLI at roughly 12 km geometric height.

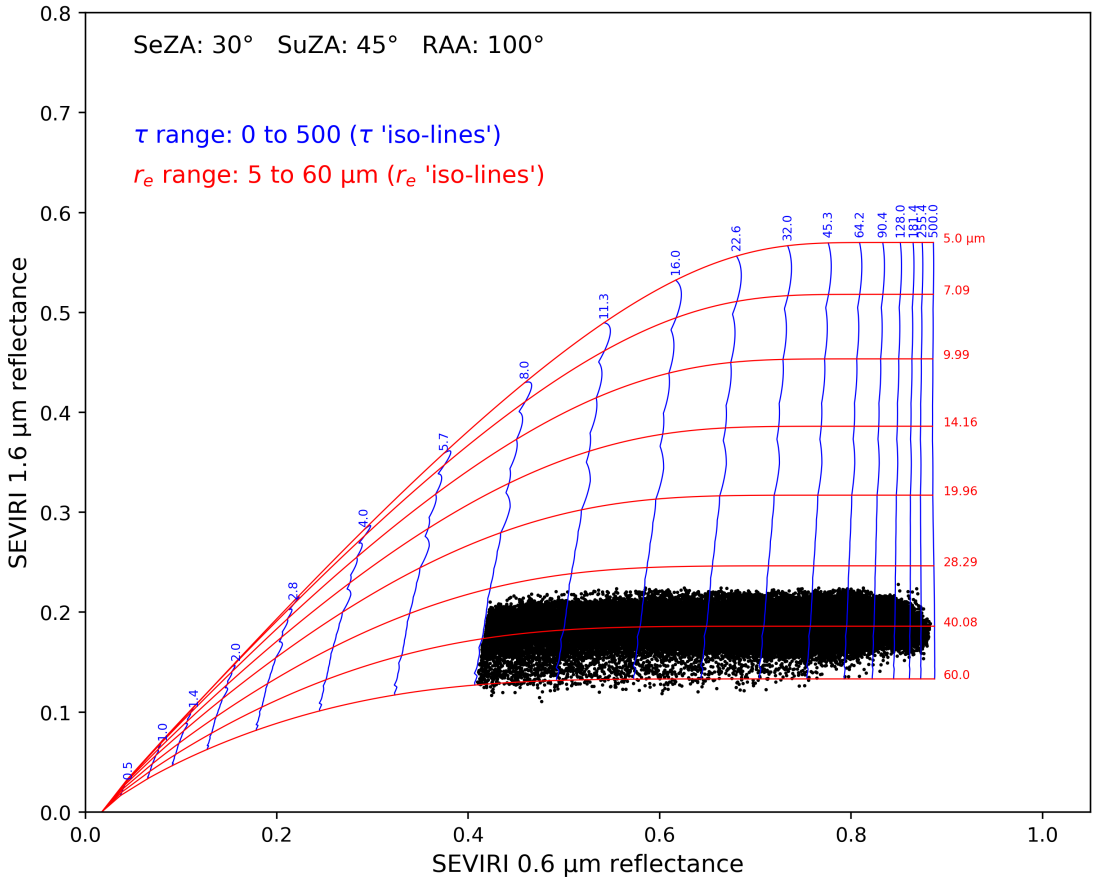

Figure A.5: Simulated reflectances scattered onto the IWP LUT. The configuration is only-CLI (C1) RTTOV input and Baran scheme used in the RTTOV calculations. Cf. Figure 13.

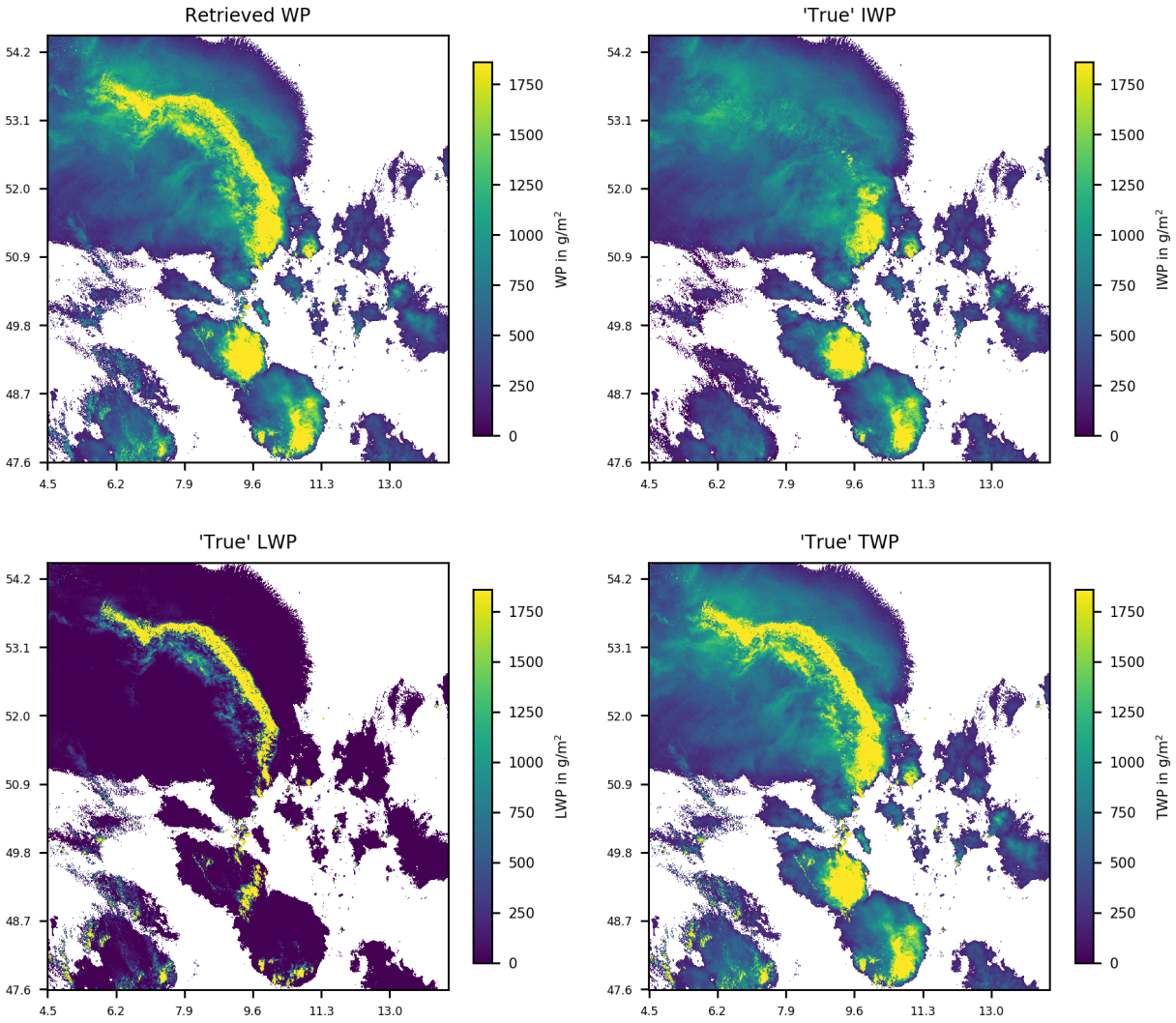

Figure A.6: Image plots of retrieved WP (upper left), "true" IWP (upper right), "true" LWP (lower left), "true" TWP (lower right) for 2013/06/20 16:00 UTC. The configuration corresponds to (C3) with CLW+CLI and $IceDe = 60$ μm. Cf. Figure 12.

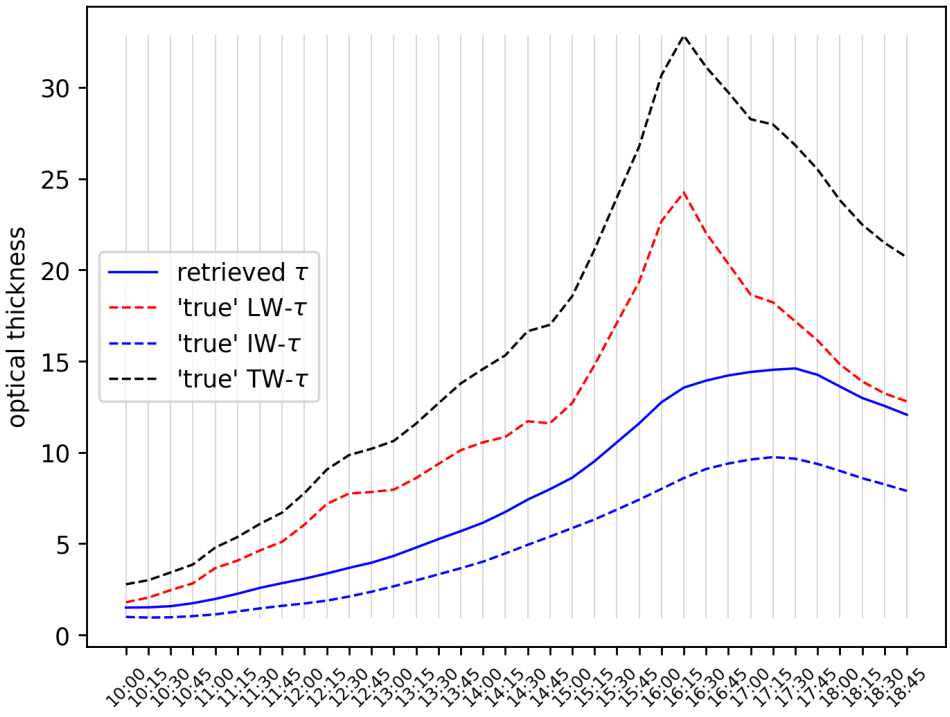

Figure A.7: All-Sky domain-means of τ under the assumption of $IceDe = 100$ μm and $Deff = 20$ μm. Shown are the retrieved τ (blue continuous line), "true" τ due to liquid clouds (red dashed line), "true" τ due to ice cloud (blue dasehd line), and "true" τ due to liquid and ice combined (black dashed line). Cf. Figure 21 (blue lines) for the corresponding WP retrieval.

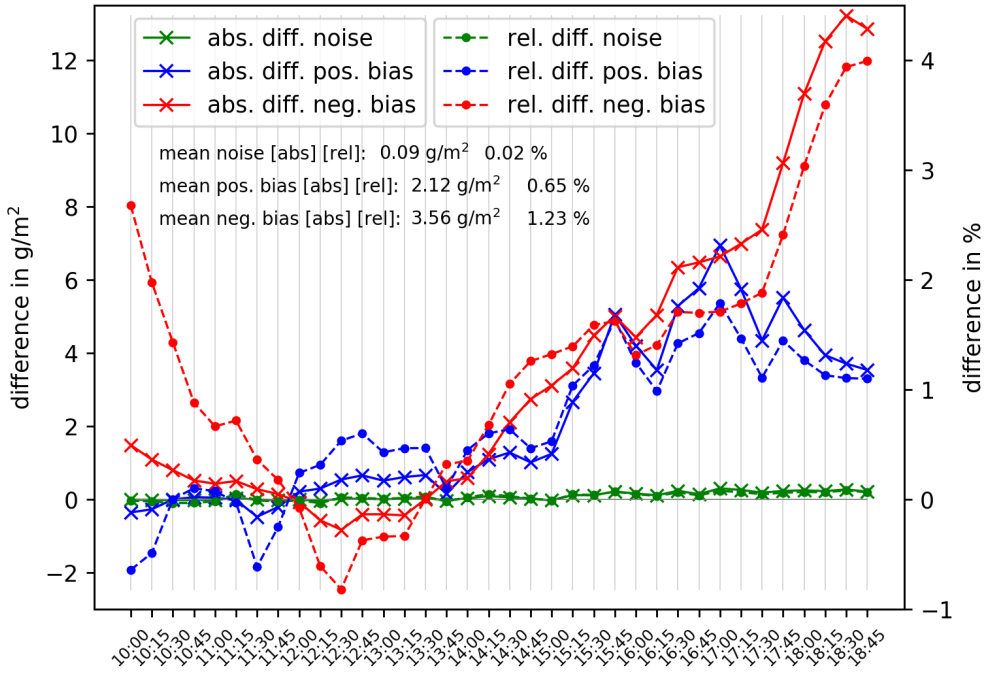

Figure A.8: Absolute (continuous lines with "×"-markers) and relative (dashed lines with filled circle markers) time-series differences of high sun (SuZA = 10°) retrievals with noise (green), positive (blue), and negative (red) bias to the retrievals without bias or noise. The differences correspond to Figure 23. See Table 4 for a summary of the statistics.

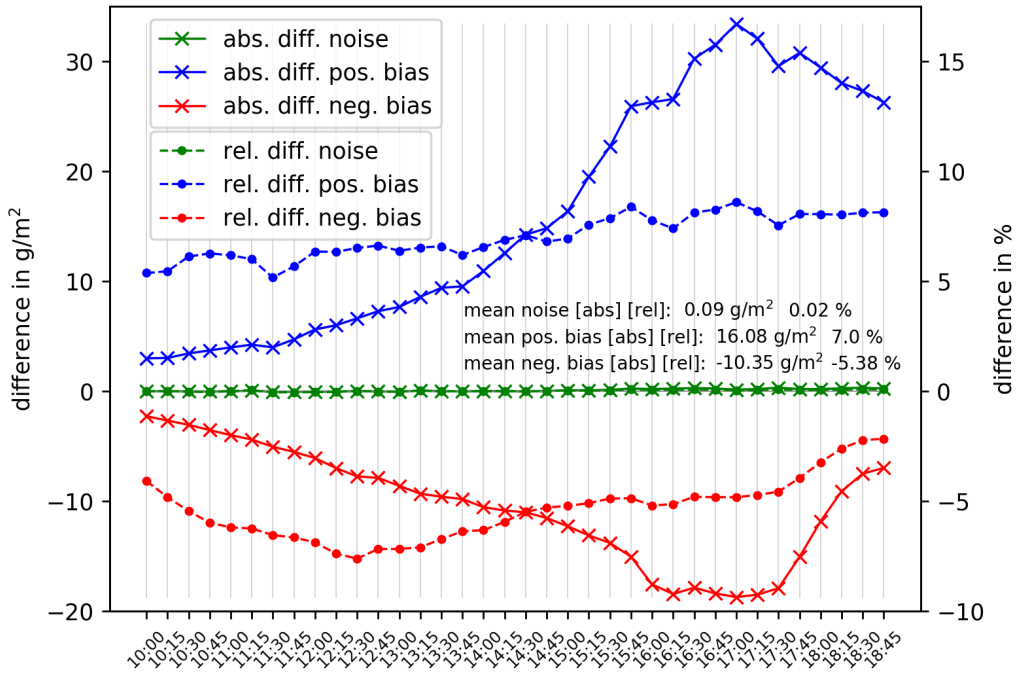

Figure A.9: Absolute (continuous lines with "×"-markers) and relative (dashed lines with filled circle markers) time-series differences of middle sun (SuZA = 45°) retrievals with noise (green), positive (blue), and negative (red) bias to the retrievals without bias or noise. The differences correspond to Figure 23. See Table 4 for a summary of the statistics.

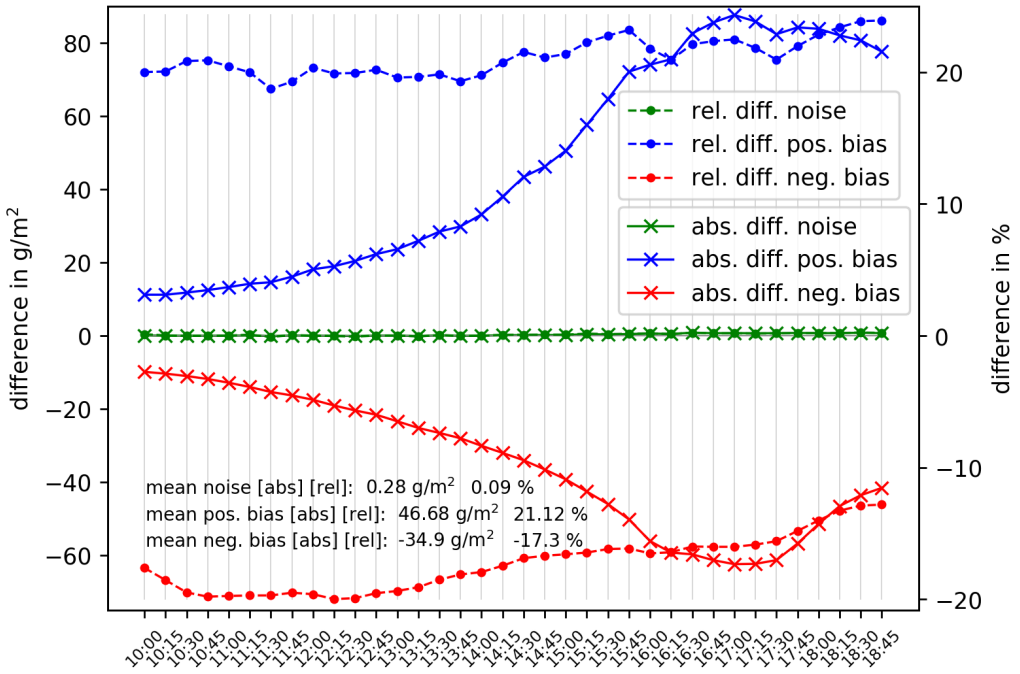

Figure A.10: Absolute (continuous lines with "×"-markers) and relative (dashed lines with filled circle markers) time-series differences of low sun (SuZA = 70°) retrievals with noise (green), positive (blue), and negative (red) bias to the retrievals without bias or noise. The differences correspond to Figure 23. See Table 4 for a summary of the statistics.

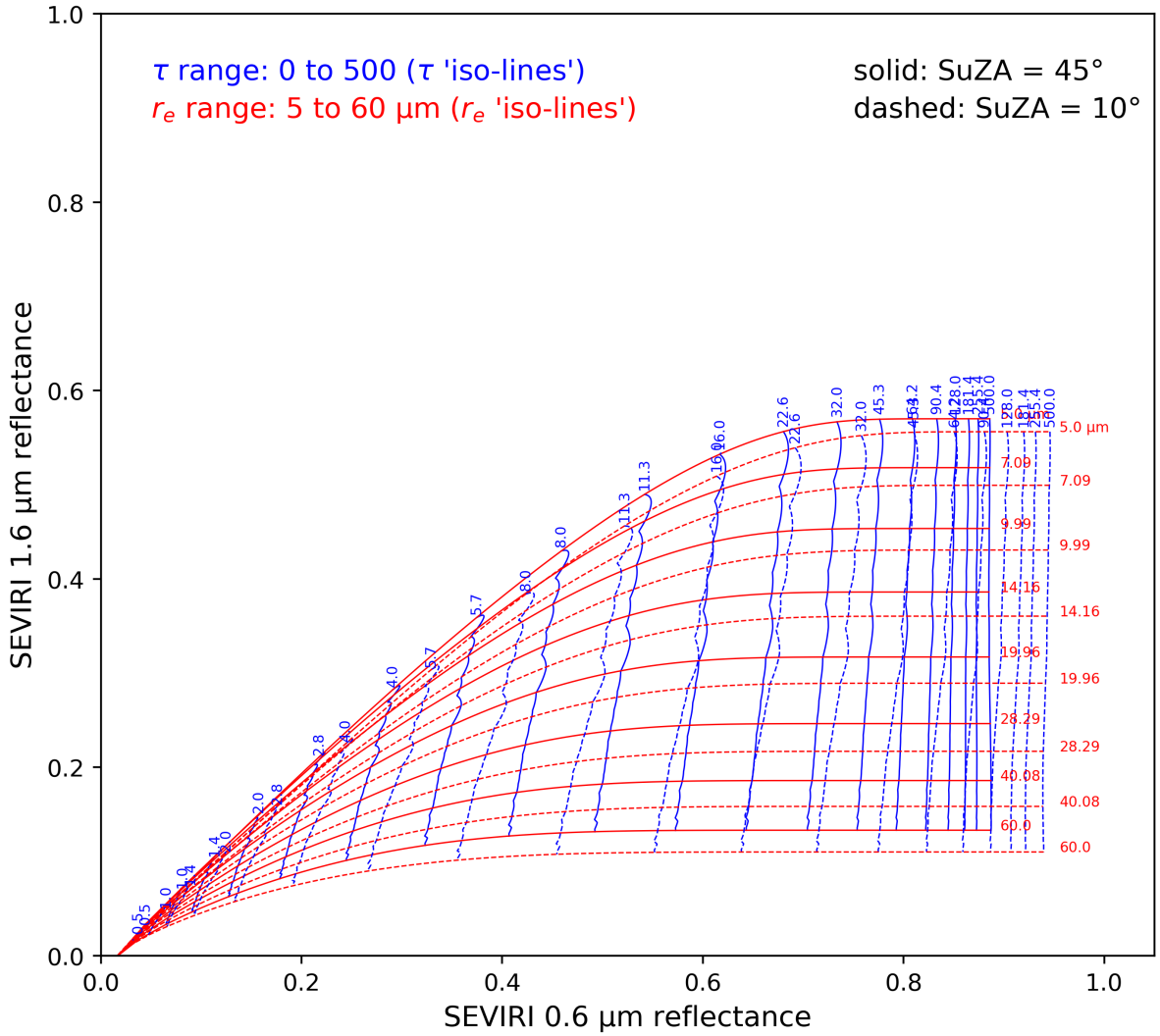

Figure A.11: IWP LUT for high sun (SuZA = 10°) compared to middle sun (SuZA = 45°). Refer to section 2.2 and Table 1 for details.

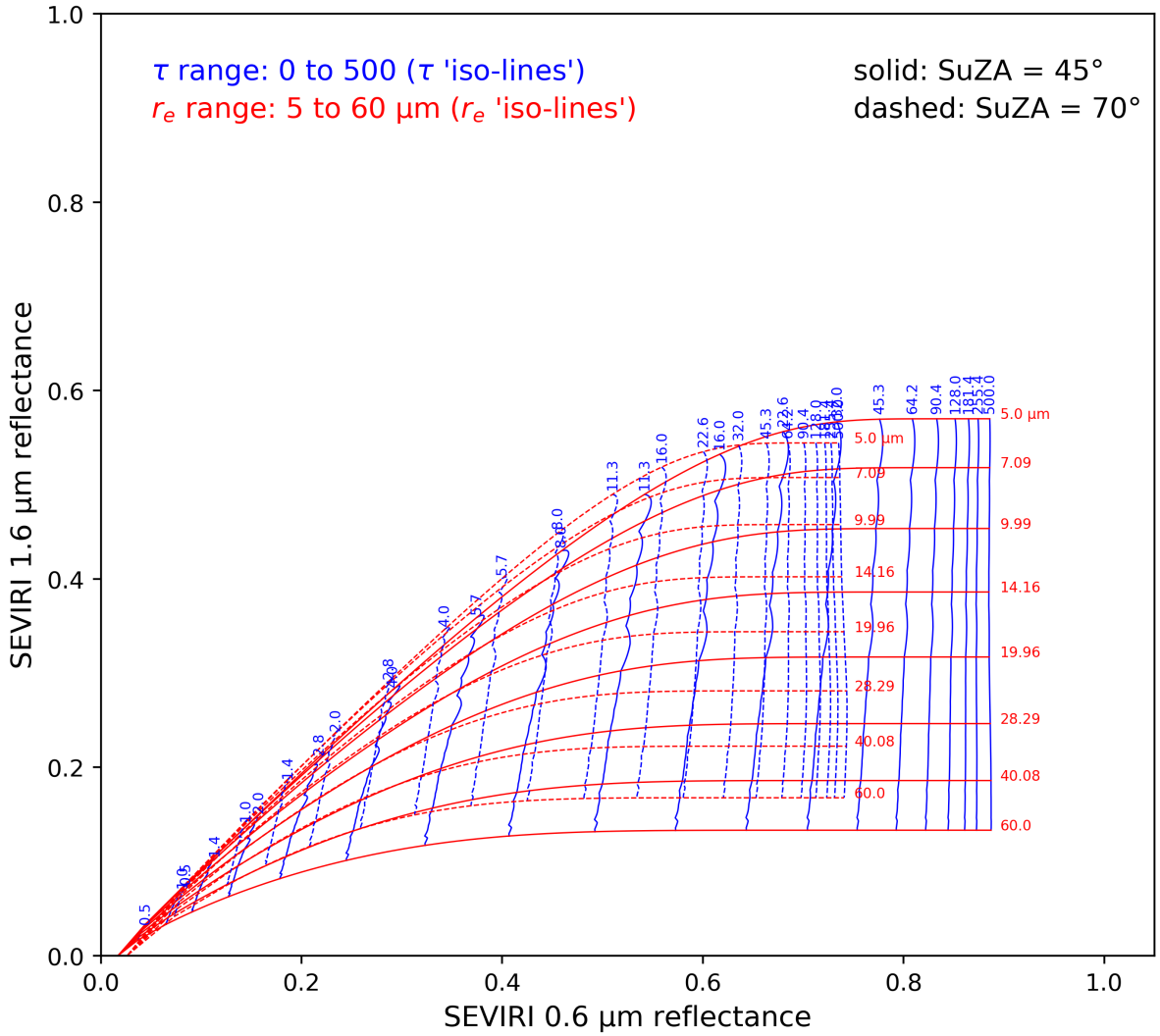

Figure A.12: IWP LUT for low sun (SuZA = 70°) compared to middle sun (SuZA = 45°). Refer to section 2.2 and Table 1 for details.

Versicherung an Eides statt

Hiermit versichere ich an Eides statt, dass ich die vorliegende Arbeit im Studiengang Master of Science Meteorologie selbstständig verfasst und keine anderen als die angegebenen Hilfsmittel − insbesondere keine im Quellenverzeichnis nicht benannten Internet-Quellen − benutzt habe. Alle Stellen, die wörtlich oder sinngemäß aus Veröffentlichungen entnommen wurden, sind als solche kenntlich gemacht. Ich versichere weiterhin, dass ich die Arbeit vorher nicht in einem anderen Prüfungsverfahren eingereicht habe und die eingereichte schriftliche Fassung der auf dem elektronischen Speichermedium entspricht.

Ich bin mit der Ausstellung der Arbeit in der Fachbibliothek einverstanden.

Ort, Datum:

Unterschrift: